Karlsruhe Institute of Technology

Outflow from the Asian Summer Monsoon and Transport in the UTLS based on GLORIA Measurements during the PHILEAS Campaign 2023

Master Thesis
by

Franziska Helena Trinkl

at the Department of Physics
Institute of Meteorology and Climate Research
Atmospheric Trace Gases and Remote Sensing (IMKASF)
Research Group for Remote Sensing using Aircraft and Balloons (FFB)

1st Reviewer	PD Dr. Michael Höpfner
2nd Reviewer	Prof. Dr. Björn-Martin Sinnhuber

May 2025

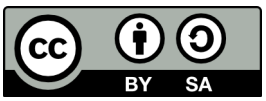

Abstract

This thesis investigates the origin, uplift mechanisms, and transport pathways of air masses enriched in Dichloromethane (CH_2Cl_2) and Peroxyacetyl Nitrate (PAN) observed over the Northeast Pacific during the PHILEAS aircraft campaign in late summer 2023. The main objective is to identify the dominant transport processes responsible for the observed enhancements in PAN and CH_2Cl_2, determine their source regions within the Asian Summer Monsoon (ASM), and assess the role of vertical and horizontal transport mechanisms such as uplift into the Asian Monsoon Anticyclone (AMA) with subsequent eddy shedding and Warm Conveyor Belts (WCBs). The analysis is based on high-resolution atmospheric composition data retrieved from the Gimballed Limb Observer for Radiance Imaging of the Atmosphere (GLORIA) aboard the HALO aircraft, complemented by model-based ICON-ART surface tracers and HYSPLIT backward trajectories driven by ERA5 reanalysis.

The results show that observed CH_2Cl_2 and, to a large fraction, PAN concentration maxima across four research flights originated predominantly from East China. The maxima in CH_2Cl_2 and PAN during Flight 8 on 26–27 August 2023 are observed in the upper troposphere as well as in the lower stratosphere. The uplift associated with the tropospheric maximum occurred mainly below the flanks of the AMA over the continent and Northwest Pacific. Its transport pathway into the upper troposphere is characterized by a horizontal export of monsoon outflow across the North Pacific. Although some uplift characteristics for the tropospheric maximum resemble WCB-related transport, the evidence remains incomplete. A consistent explanation for the transport of air belonging to the stratospheric maxima is the transport through deep convention into the AMA and subsequent eddy shedding related to the West Pacific Anticyclone (WPA). This raises the question of whether both WCBs and deep convective ascent within the AMA can simultaneously contribute to tropospheric as well as stratospheric filaments of monsoon air over the northeastern Pacific.

Further investigation, particularly involving shorter-lived tracers and PV-based diagnostics, is needed to refine the attribution of uplift mechanisms and mixing events influencing the extratropical UTLS.

Zusammenfassung

Diese Arbeit untersucht die Herkunft, Aufstiegsmechanismen und Transportpfade von Luftmassen mit erhöhten Konzentrationen von Dichlormethan (CH_2Cl_2) und Peroxyacetylnitrat (PAN), die im Spätsommer 2023 während der PHILEAS-Flugkampagne über dem Nordostpazifik beobachtet wurden. Ziel der Arbeit ist es, die dominanten Transportprozesse zu identifizieren, die für die beobachteten PAN- und CH_2Cl_2-Anreicherungen verantwortlich sind, deren Ursprungsregionen innerhalb des asiatischen Sommer-Monsuns (ASM) zu bestimmen und die Rolle vertikaler und horizontaler Transportmechanismen wie dem Aufstieg in den asiatisschen Monsun-Antizyklon (AMA) mit anschließendem Eddy Shedding sowie den Warm Conveyor Belts (WCBs) zu bewerten. Die Analyse basiert auf hochaufgelösten Messdaten der atmosphärischen Zusammensetzung, die mit dem GLORIA (Gimballed Limb Observer for Radiance Imaging of the Atmosphere) Instrument an Bord des Forschungsflugzeugs HALO gewonnen wurden, ergänzt durch modellbasierte ICON-ART-Emissionstracer sowie Trajektorienanalysen mit dem HYSPLIT-Modell auf Basis von ERA5-Reanalysedaten.

Die Ergebnisse zeigen, dass die beobachteten Konzentrations-Maxima von CH_2Cl_2 sowie zu einem großen Teil auch von PAN während vier Forschungsflügen überwiegend aus Ostchina stammten. Die Maxima von CH_2Cl_2 und PAN während Flug 8 am 26.–27. August 2023 wurden sowohl in der oberen Troposphäre als auch in der unteren Stratosphäre beobachtet. Der mit dem troposphärischen Maximum verbundene Aufstieg erfolgte hauptsächlich unterhalb der Flanken des AMA über dem Kontinent und dem Nordwestpazifik. Der Transportpfad in die obere Troposphäre ist durch einen horizontalen Export des von Mosnsunluft über den Nordpazifik gekennzeichnet. Obwohl einige Merkmale des Aufstiegs auf WCB-bezogenen Transport hindeuten, bleibt der Nachweis unvollständig. Eine konsistente Erklärung für den Transport der Luftmassen, die dem stratosphärischen Maximum zuzuordnen sind, ist der Aufstieg durch Konvektion in den AMA mit anschließendem Eddy Shedding, das mit dem westpazifischen Antizyklone (WPA) in Verbindung steht. Dies wirft die Frage auf, ob sowohl WCBs als auch tiefkonvektiver Aufstieg innerhalb des AMA gleichzeitig zur Bildung troposphärischer sowie stratosphärischer Filamente von Monsunluft über dem nordöstlichen Pazifik beitragen können

Zur genaueren Bestimmung der zugrunde liegenden Aufstiegsmechanismen und Mischungsprozesse, die die Zusammensetzung der extratropischen UTLS beeinflussen, sind weiterführende Untersuchungen mit kurzlebigeren Tracern und PV-Diagnosen erforderlich.

Contents

Abbreviations

AMA Asian Monsoon Anticyclone.

ASM Asian Summer Monsoon.

EASM East Asian Summer Monsoon.

ECMWF European Centre for Medium-Range Weather Forecasts.

GLORIA Gimballed Limb Observer for Radiance Imaging of the Atmosphere.

HALO High Altitude and Long Range Research Aircraft.

HYSPLIT Hybrid Single-Particle Lagrangian Integrated Trajectory model.

ICON ICOsahedral Nonhydrostatic weather- and climate model.

ICON-ART ICOsahedral Nonhydrostatic weather- and climate model with Aerosols and Reactive Trace gases.

LMS Lowermost Stratosphere.

MIPAS Michelson Interferometer for Passive Atmospheric Sounding.

PAN Peroxyacetyl nitrate.

PHILEAS Probing High Latitude Export of Air from the Asian Summer Monsoon.

ROI Region (Regions) of Interest.

UTLS Upper Troposphere Lower Stratosphere.

VMR Volume Mixing Ratio.

WCB Warm Conveyor Belt.

WPA West Pacific Anticyclone.

List of Figures

List of Tables

1 Introduction

The upper troposphere and lower stratosphere (UTLS) form a crucial and climate-sensitive interface in Earth's atmosphere. This region plays an important role in regulating the global energy balance, modulating weather systems, and governing the exchange of radiatively active trace gases. Due to its proximity to both, surface emissions and stratospheric circulation, the UTLS is especially sensitive to perturbations, natural or anthropogenic. Even small changes in its chemical composition or dynamical structure can have far-reaching consequences for climate, ecosystems, and public health.

One of the dominant meteorological phenomena influencing the structure and composition of the UTLS in the Northern Hemisphere is the Asian Summer Monsoon (ASM). The ASM not only induces deep convection, but also contributes significantly to the vertical and horizontal transport of pollution from the planetary boundary layer into the UTLS, primarily through the Asian monsoon anticyclone (AMA). One of the major gaps in the understanding of northern-hemispheric stratosphere-troposphere exchange lies in the limited observational coverage of the Northern Hemisphere transition region at middle and high latitudes. This region plays a key role in the decay of eddies shed from the Asian Monsoon Anticyclone (AMA) and their subsequent mixing into the lowermost stratosphere (LMS), which was found to significantly influence the composition and dynamics of the UTLS.

To better understand these processes, the PHILEAS (Probing High Latitude Export of Air from the Asian Summer Monsoon) campaign was conducted in August and September 2023. Using the German High Altitude and Long Range Research Aircraft (HALO), the campaign focused on characterizing the long-range transport and cross-tropopause exchange of monsoon-influenced air masses. The Gimballed Limb Observer for Radiance Imaging of the Atmosphere (GLORIA), developed jointly by the Karlsruhe Institute of Technology (KIT) and Forschungszentrum Jülich (FZJ), was one of the instruments deployed on HALO. It provides high-resolution measurements allowing for retrieval of thermal and chemical atmospheric profiles. Among the trace gases retrieved during PHILEAS, Peroxyacetyl Nitrate (PAN) and, for the first time, Dichloromethane (CH_2Cl_2) were analyzed to investigate outflow from the ASM and its impact on the UTLS over the North Pacific.

This thesis therefore addresses the following key questions:

- What are the characteristics with respect to the UTLS of the observed enhancements of PAN and CH_2Cl_2 above the northeastern Pacific?

- From which specific regions within the ASM does this polluted outflow originate?
- To what extent do different uplift mechanisms, such as Warm Conveyor Belts (WCBs) and ascend in the AMA with subsequent eddy shedding, contribute to the observed transport?

In order to explore these questions, the structure of this thesis is organized as follows:

A review of the current scientific understanding of the Asian Summer Monsoon is provided in Chapter 2, with emphasis on its dynamical structure, pollutant entrainment, and the role of the AMA transport gateway into the UTLS. It also introduces WCBs as an efficient uplift mechanism into the UTLS in extratropical regions. Finally, the chemical tracers PAN and CH_2Cl_2 are presented as trace gases for identifying monsoon outflow and assessing its influence on the chemical composition of the UTLS.

Chapter 3 describes the observational dataset and the methods applied in this thesis. This includes an overview of the GLORIA instrument, its measurement principles, and retrieval techniques. The chapter also outlines the four PHILEAS research flights selected for the following analysis. Transport diagnostics are introduced with the use of ICON-ART surface tracers and HYSPLIT trajectory simulations based on ERA5 reanalysis data from ECMWF.

The main results are presented in Chapter 4 and the findings are discussed in detail. Retrieved cross sections of PAN and CH_2Cl_2 are shown, followed by the characterization of the retrievals. The vertical and horizontal transport pathways are reconstructed using ICON-ART tracers and backward trajectories, highlighting key features of the Asian outflow. The influence of WCB activity and eddy shedding in shaping the observed tracer structures is discussed and compared to literature. Particular attention is paid to differences between tropospheric and stratospheric signatures, and the implications for stratosphere-troposphere exchange.

Chapter 5 concludes the thesis by summarizing the main findings, addressing the research questions, and offering an outlook on future directions for investigation, particularly regarding the role of rapid uplift mechanisms and their potential interaction in transporting short-lived species into the UTLS.

2 State of Research

2.1 System of the Asian Summer Monsoon

The Asian Summer Monsoon (ASM) is among the most influential atmospheric circulation systems in the Northern Hemisphere. It governs seasonal weather patterns across a vast region, bringing a distinct wet and dry season that affects the livelihoods of billions. During the boreal summer, moist southwesterly winds dominate, leading to intense rainfall, while in winter, dry northeasterly winds prevail. The ASM is more intense than other monsoon systems due to unique geographic and thermodynamic conditions such as the Himalayan and the Tibetan Plateau and diverse surface heat sources (Siu and Bowman, 2019).

2.1.1 Characteristics and Subsystems of the Asian Summer Monsoon

The thermal contrast between the solar heating Asian continent and the surrounding oceans during spring and early summer creates a low-pressure zone that draws in moist air from the Indian Ocean and western Pacific. The Himalayas and the Tibetan Plateau act as a barrier and elevated heat source, enhancing vertical motion and sustaining deep convection (Boos and Kuang, 2010, B. Wang and LinHo, 2002). The interplay of these elements results in characteristic features such as strong rainfall, deep convective towers, and upper-level anticyclonic flow near the tropopause (Gottschaldt et al., 2018).

Due to its geographic span and complex structure, the ASM is often subdivided into regional components. Two commonly used frameworks offer distinct but complementary perspectives. According to e.g. Pan et al., 2024 and Li et al., 2022, the ASM consists of two main components: the South Asian Summer Monsoon (SASM) and the East Asian Summer Monsoon (EASM) as seen in Figure 2.2. These regions are controlled by different dominant heat sources and display differing sensitivities to climatic variations, including responses to a warming climate. B. Wang and LinHo, 2002 use a division into the Indian Summer Monsoon (ISM), Western North Pacific Summer Monsoon (WNPSM), and East Asian Summer Monsoon (EASM). This classification is based on the onset timing, evolution, and regional dynamical behavior of the monsoon system, though the components remain dynamically interconnected across Asia (Ding and Chan, 2005). Both views emphasize the monsoon's coupled nature, despite internal regional variability and the different manifestations of convective and dynamic processes within the larger ASM circulation. The EASM is a subtropical system characterized by a seasonal reversal of low-level winds, shifting from northerly in winter to southerly in summer. This reversal is driven by a pronounced east–west

thermal contrast between the Asian landmass and the western Pacific, which establishes a zonal pressure gradient between the continental low and the Western Pacific Subtropical High (WPSH) (B. Wang and LinHo, 2002, Pan et al., 2024).

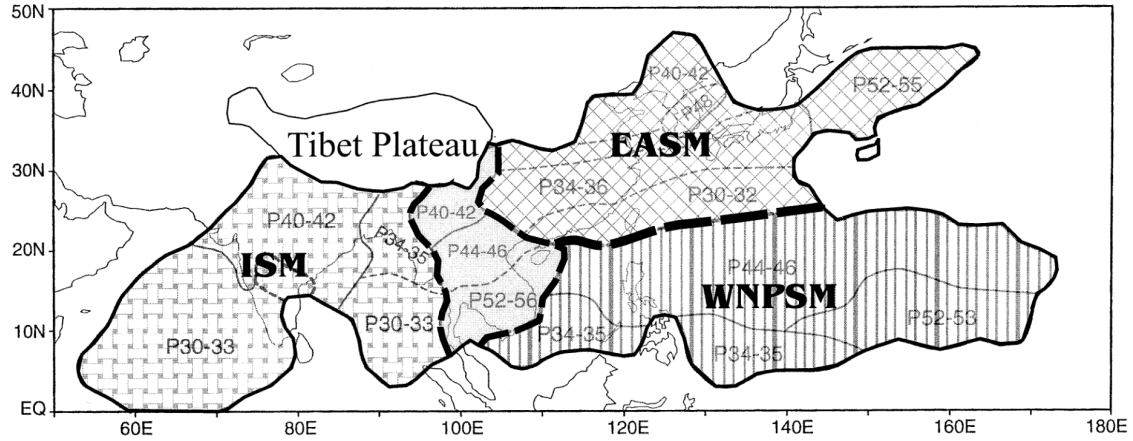

Figure 2.1: Subsystems of the ASM. This possible subdivision of the whole ASM system after B. Wang and LinHo, 2002 is primarily based on the onset of the ASM in the different regions and the seasonal development over time. The Indian Summer Monsoon (ISM) and the Western North Pacific Summer Monsoon (WNPSM) are classified as tropical monsoon systems. The East Asian Summer Monsoon (EASM), representing a subtropical monsoon regime, borders the WNPSM along a relatively narrow boundary. This Figure is from B. Wang and LinHo, 2002.

The onset of the ASM rainy season is a complex, phased phenomenon that typically begins over the southern Indochina Peninsula, catalyzed by increased sea surface temperatures in the Bay of Bengal, cyclonic activity, and intensifying southwesterly winds. This is followed by a stepwise northward advance, first reaching the Indian subcontinent and then progressing toward China, Korea, and Japan, where it manifests in the Meiyu–Baiu rainy season (B. Wang and LinHo, 2002, Ding and Chan, 2005, Pan et al., 2024). The peak monsoon activity typically occurs between mid-June and August, characterized by widespread deep convection and large-scale rainfall systems. The retreat phase and direction varies regionally and is generally less abrupt than the onset, the EASM diminishes to the north, whereas in the tropical monsoon systems the activity retreats to the south (B. Wang and LinHo, 2002).

The ASM displays variability on multiple timescales, including intra-seasonal oscillations, interannual variability, and decadal trends. For example, the East Asian Summer Monsoon is especially sensitive to ocean-atmosphere coupling and exhibits significant variability influenced by phenomena such as the El Niño–Southern Oscillation (ENSO) and Pacific Decadal Oscillation (Ding, 2007). Climate model projections suggest divergent trends for different monsoon subsystems. While the EASM is expected to strengthen under global warming due to increased moisture availability, the SASM may weaken due to declining land-sea thermal contrast (Li et al., 2022). Recent years have shown evidence of altered ASM behavior under climate change (Pan et al., 2024).

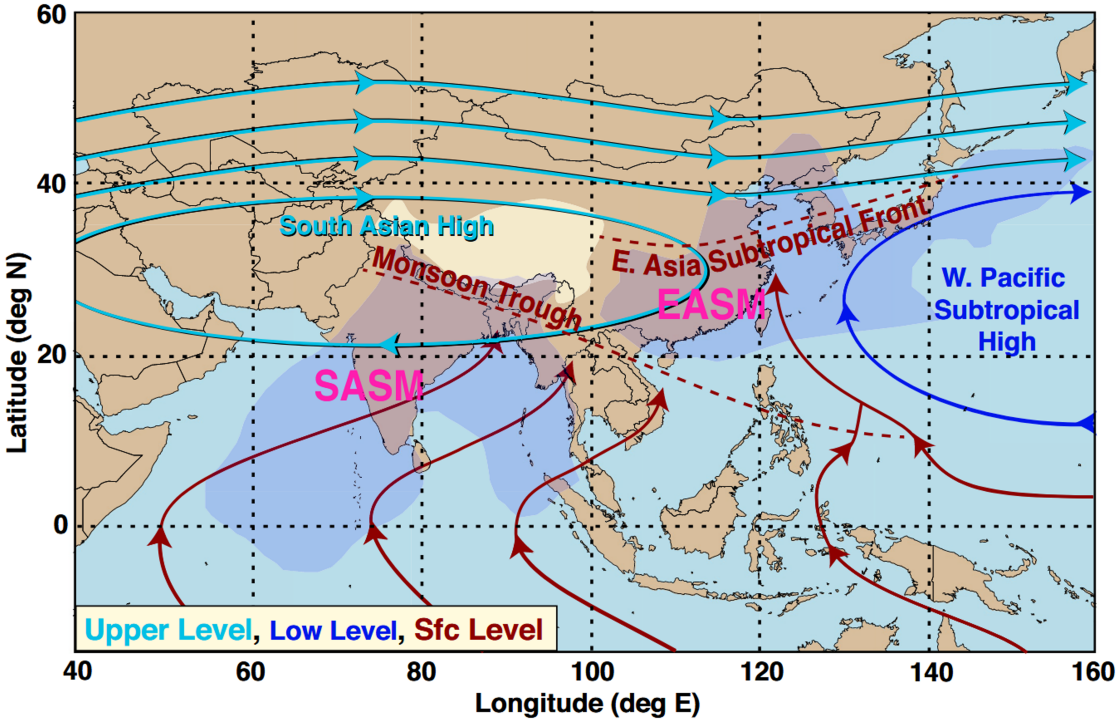

Figure 2.2: Schema of the defining dynamical components of the ASM at three representative pressure levels: near-surface (1,000 hPa) in brown, low-level (850 hPa) in blue, and upper-level (200 hPa) in turquoise. A key precipitation system in this region is the East Asia Subtropical Front, positioned on the northwestern edge of the Western Pacific Subtropical High, which undergoes a seasonal northward shift. This figure is from Pan et al., 2024.

2.1.2 Uplift into the Asian Monsoon Anticyclone and Eddy Shedding

One of the defining features of the ASM is its deep convective updrafts, which are capable of rapidly transporting trace gases, aerosols, and pollutants from the boundary layer into the UTLS region. This vertical uplift is not uniform across the ASM. Historically, the South Asian monsoon region was thought to dominate this vertical transport. However, recent findings reveal that the East Asian Summer Monsoon also plays a critical role in lifting air masses to altitudes above the level of zero radiative heating (LZRH). At this level, air becomes neutrally or positively buoyant and can be further transported into the stratosphere (Pan et al., 2024). The uplift of air masses in the ASM system leads to the formation of the Asian Monsoon Anticyclone (AMA), a recurring feature in the UTLS that acts as a reservoir for air masses enriched with pollutants and humidity. The AMA thus represents a major atmospheric gateway, with implications for both regional air quality and global stratospheric chemistry (Vogel et al., 2015, Ungermann et al., 2016, Ploeger et al., 2017,Lauther et al., 2022, Pan et al., 2024). The AMA is a consequence of intense diabatic heating associated with deep convection over South Asia and the Tibetan Plateau (Garny and Randel, 2013, see Figure 2.3). Its development and structure have been the focus of extensive theoretical and observational research, revealing a complex dynamical system.

The foundational understanding of the AMA originates from theoretical work using shallow water equations, particularly the study by Gill, 1980, which demonstrated, how tropical heat sources generate a stationary Rossby wave response to the west and an eastward-propagating Kelvin wave.

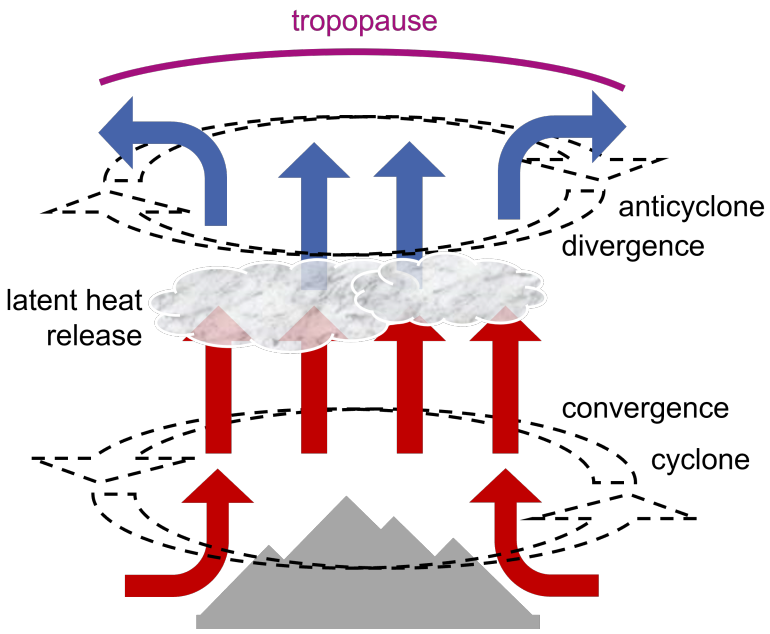

Figure 2.3: Uplift in the ASM region and formation of the AMA. Rising moist and warm air from the monsoon region (e.g. Tibetan Plateau) is convectively uplifted. The lated heat release through precipitation creates a wave response (Gill, 1980). As a result the cooled diverging air below the tropopause is confined in the spiraling of the emerging anticyclone from 300 to 50 hPa (Siu and Bowman, 2019, Garny and Randel, 2013).

This framework effectively describes the large-scale upper-tropospheric circulation anomalies observed during the monsoon season. Subsequent modeling by Hsu and Plumb, 2000 extended this understanding, showing that a localized monsoon-like heating can give rise to an anticyclone that periodically sheds eddies. These shed eddies propagate westward and eastward, as then observed by Popovic and Plumb, 2001, contributing to the overall transport characteristics of the AMA.

Dynamically, the AMA is bounded latitudinally between the subtropical westerly jet to the north and the tropical easterly jet to the south, which act as waveguides for its maintenance and variability. Vertically, the anticyclone extends from the upper troposphere into the lower stratosphere, with its core typically found near the 200 to 100 hPa level (Randel and Park, 2006). The heating-induced upward motion contributes to a bulging of the tropopause over the monsoon region, creating a region of elevated tropopause that enables horizontal transport quasi-isentropic into the stratosphere (Pan et al., 2016, 2024, Siu and Bowman, 2019, 2020). A key dynamical signature of the AMA is its association with low potential vorticity (PV) in the UTLS. This anomaly arises due to the influence of diabatic heating from persistent convection, which lowers the static stability and PV in the upper-level anticyclone. These PV anomalies serve as markers for identifying and tracking the AMA in both observational and modeling studies (e.g. Garny and Randel, 2013, Pan et al., 2016 and references therein).

The AMA exhibits both intra-seasonal and inter-annual variability. This variability is closely linked to shifts in convective intensity, the location of maximum heating, and the phase of large-scale climate modes such as the Madden–Julian Oscillation. Furthermore, the AMA often exhibits multiple centers or subvortices, including the Iranian and Tibetan anticyclones (Basha et al., 2020).

These components evolve over the course of the monsoon season, reflecting the shifting centers of deep convection and associated diabatic forcing (Siu and Bowman, 2020, X. Wang et al., 2022).

Air is lifted into the AMA predominantly through deep convection and cyclonic activity such as typhoons. Observations indicate that convective outflow follows spiraling upward trajectories, eventually reaching the upper troposphere and becoming confined within the anticyclone. This transport mechanism has been described as quasi-isentropic, highlighting the role of isentropic uplift in transporting surface air to the UTLS (Vogel et al., 2014, 2015, 2016, 2019, 2024, Pan et al., 2016). In this UTLS region the AMA acts as an effective transport barrier, resulting in the confinement and accumulation of trace gases and pollutants. Due to limited horizontal mixing with the surrounding environment, air masses within the AMA become chemically distinct from midlatitude and tropical background air. Studies have shown that the AMA effectively traps anthropogenic pollutants and water vapor, contributing to observed anomalies in the UTLS composition and the Asian tropopause aerosol layer (ATAL) during the monsoon period (Vernier et al., 2011,Pan et al., 2016, Ploeger et al., 2017).

This transport barrier however, is not as impermeable, as initially assumed. The AMA enables horizontal transport via eddy shedding. Eddies are shed both westward and eastward from the anticyclonic center, carrying air masses along isentropic surfaces into the lower stratosphere. This process is closely tied to the AMA's bulging tropopause, which allows for enhanced cross-tropopause exchange. The circulation of the West Pacific anticyclone (WPA), which Honomichl and Pan, 2020 described as a third possible mode of the AMA, is a direct result of westward shed eddies from the AMA vortex over the Asian continent. Eddy shedding events are not continuous but occur episodically, with several events typically observed during each monsoon season (Vogel et al., 2016). These events represent a key mechanism by which the AMA interacts with surrounding air masses and contributes to the redistribution of trace constituents in the UTLS (Honomichl and Pan, 2020, Pan et al., 2016).

Understanding these processes has been the objective of several major observational campaigns. Aircraft campaigns such as StratoClim and ACCLIP, have provided detailed in situ and remote sensing observations of the AMA's structure and chemical properties. These campaigns have played a critical role in validating transport theories and improving the representation of the AMA in global models (e.g. Pan et al., 2016, Vogel et al., 2016, 2019, von Hobe et al., 2021, Pan et al., 2024)

2.2 Warm Conveyor Belts as Intercontinental Transport Pathways into the UTLS

Warm Conveyor Belts (WCBs) represent one of the most efficient large-scale coherent airstreams for the rapid vertical transport of air masses from the boundary layer into the UTLS. Their characteristic dynamics, coupling to synoptic-scale weather systems and injection of pollutants into the jet stream make them critical pathways for the intercontinental movement of moisture, energy, and chemical tracers, including anthropogenic and natural pollutants (Huntrieser et al., 2005). WCBs typically form within midlatitude baroclinic systems and are closely associated with the warm sector of extratropical cyclones. They are defined as coherent, narrow airstreams ascending from the lower troposphere, often starting in the marine boundary layer, and reaching altitudes of up to 10-12 km within 2 to 3 days. This rapid ascent is driven by frontal dynamics and is sustained by diabatic processes, primarily latent heat release during cloud formation (Joos et al., 2023).

The ascent in WCBs occurs in distinct stages: a shallow initial rise near the surface, followed by a rapid mid-level ascent associated with the warm front, and concluding in the upper troposphere where the air is detrained as outflow (Madonna et al., 2014). This evolution is accompanied by widespread cloud formation and heavy precipitation, particularly during the frontal lifting phase, as large quantities of moisture are condensed and precipitated (Eckhardt et al., 2004, Joos et al., 2023). WCBs are dynamically coupled to the lifecycle of extratropical cyclones. The latent heat released during ascent reinforces the cyclone's development, influencing upper-level jet dynamics and midlatitude wave breaking. The positioning of WCB ascent ahead of the cyclone's cold front and the generation of extensive cloud shields mark this interaction (Madonna et al., 2014).

Climatologically, the frequency and characteristics of WCBs vary seasonally and regionally. In the Northern Hemisphere, WCBs occur more frequently during winter and spring, particularly over the storm tracks in the North Atlantic and North Pacific (see Figure 2.4). During summer, their occurrence diminishes, and the ascent tends to be weaker and more localized (Joos et al., 2023). Regional studies show that WCBs over the North Pacific are especially relevant for intercontinental transport due to their frequent formation, robust ascent, and proximity to major Asian emission regions (Eckhardt et al., 2004, Miyazaki et al., 2003, Cooper et al., 2004).

Due to their rapid vertical motion and connection to surface air masses, WCBs can efficiently transport boundary layer pollutants into the upper troposphere. This capability becomes especially relevant in the context of emissions from East Asia, particularly China and India. During the Asian summer monsoon, strong convection over the Indian subcontinent and Southeast Asia lifts trace gases and aerosols from near the surface into the upper troposphere, from where they can be entrained into WCBs and transported further eastward (Miyazaki et al., 2003). Pollutants such as carbon monoxide (CO), nitrogen oxides (NO_x), ozone (O_3), PAN, and various volatile organic compounds can be carried over intercontinental distances. The vertical transport within WCBs may even lead to the crossing of the tropopause, enabling injection into the lower stratosphere. This stratosphere-troposphere exchange can have significant impacts on regional and global chemical

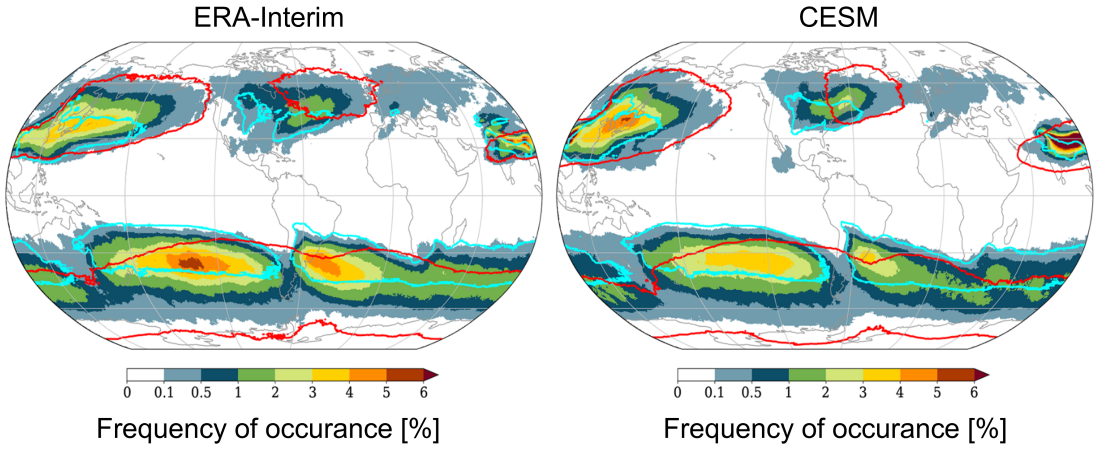

Figure 2.4: Climatological occurance of WCBs in the northern hemispheric winter from ERAInterim data and the CESM Community Earth System Model for 10 years (1990–1999). The color shading represents the percentage of 6-hour intervals during which at least one WCB trajectory is found within a 100 km radius of a given grid point, evaluated 24 hours after the onset of ascent. A turquoise contour marks regions where WCB occurrence reaches 1% at the initial time ($t = 0\,\mathrm{h}$), while a red contour indicates the same frequency at the end of the ascent phase ($t = 48\,\mathrm{h}$) This figure was taken from Joos et al., 2023 with minor modifications regarding labels.

composition, including radiative forcing and stratospheric ozone chemistry (Madonna et al., 2014, Joos et al., 2023).

Observational campaigns and modeling studies in the 2000s have confirmed the role of WCBs in long-range pollution transport. For instance, Cooper et al., 2004 analyzed ozone and CO measurements over North America and showed that elevated levels frequently coincided with air masses traced back to East Asia, transported via WCBs. Similarly, Miyazaki et al., 2003 showed that WCBs act as major conduits for the uplift and redistribution of (South)east Asian emissions like NO_x, also in form of it's reservoir gas PAN, emphasizing their role in linking regional sources to global atmospheric composition.

WCBs are not only meteorologically significant features of extratropical cyclones but also crucial atmospheric structures for the intercontinental redistribution of pollutants. Their efficiency in transporting boundary layer air into the UTLS underscores their importance in studies of air quality, effects on the radiative forcing and the global tropospheric chemistry budget.

2.3 Tracers for Monsoon Air

2.3.1 PAN as Trace Gas for Anthropogenic and Biogenic Processes

The study of atmospheric oxidants began with investigations into the phenomenon of photochemical "smog" in the mid-20th century. This smog arises from the solar-driven reactions between volatile organic compounds and nitrogen oxides (NO_x), primarily emitted from anthropogenic sources such as traffic and industrial processes. These reactions, driven by free radicals under sunlight, lead to a wide range of secondary pollutants, including ozone (O_3), hydrogen peroxide, and a class of compounds known as peroxyacyl nitrates. Among these, peroxyacetyl nitrate (PAN, $CH_3C(O)OONO_2$) emerged as the most abundant and widely studied member. PAN was initially noted in the 1950s for its phytotoxic effects, particularly its ability to cause “leaf bronzing” in plants, where it proved even more damaging than ozone. For humans, PAN exposure has been linked to adverse effects on respiratory and cardiovascular health and may also influence the prevalence of skin cancer. These early findings highlighted the importance of PAN not only as an atmospheric constituent but also as a public health concern (Gaffney et al., 1989).

Subsequent research established PAN as a chemically reactive trace gas that serves as the most significant reservoir species for NO_x in the troposphere. Its formation is closely linked to the oxidation of non-methane volatile organic compounds (NMVOCs) in the presence of NO_x, with both anthropogenic and natural processes contributing to this chemistry. Fossil fuel combustion, biomass burning, lightning activity, and soil emissions act as the principal sources of the required precursors. The production pathway involves a sequence of reactions, beginning with hydrocarbon oxidation to form peroxyacetyl radicals, which subsequently react with NO_x to form PAN, as seen below, in a temperature-dependent equilibrium (Fischer et al., 2014, Glatthor et al., 2007, Gaffney et al., 1989):

$$CH_3C(O)OO + NO_2 \rightleftharpoons CH_3C(O)OONO_2 \tag{2.1}$$

Due to its relatively large molecular mass and structural complexity (see Figure 2.5), PAN exhibits densely packed spectral lines, causing significant overlap from individual rotational-vibrational transitions. This results in broad emission bands, with little details, where single rotational-vibrational lines cannot be resolved by conventional FTIR spectroscopy (Glatthor et al., 2007).

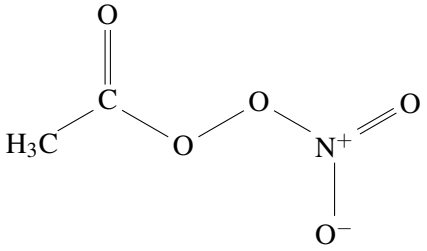

Figure 2.5: Structural formula of a PAN molecule

PAN plays a dual role in atmospheric chemistry: it functions both as a reservoir for NO_x and as a precursor for ozone. When PAN undergoes thermal decomposition, especially upon warming of polluted air masses, it releases NO_x, which can photolyze to NO and atomic oxygen, as seen in equation 2.2 (Gaffney et al., 1989, Singh, 1987). The latter reacts with molecular oxygen, leading to ozone formation under the presence of a third chemical substance M, see equation 2.3. This mechanism enhances tropospheric ozone concentrations (Mahieu et al., 2021, Glatthor et al., 2007).

$$NO_2 + h\nu(\lambda < 420\,nm) \longrightarrow NO + O \tag{2.2}$$

$$O + O_2 + M \longrightarrow O_3 + M \tag{2.3}$$

A defining feature of PAN is its high sensitivity to ambient temperature. Its atmospheric lifetime varies substantially, from around one hour in warm lower tropospheric conditions to several months in the cold upper troposphere. Because of this, PAN is especially effective at transporting reactive nitrogen over large distances when temperatures are low, enabling long-range pollution transport (Singh, 1987). Seasonal variations in PAN abundance reflect this dependency, with concentrations generally peaking during the Northern Hemisphere spring and summer, when both precursor emissions and atmospheric lifetimes favor its accumulation (Fischer et al., 2014, Mahieu et al., 2021).

Significant regional sources of PAN have been identified in Eastern and Southern Asia, particularly over China and India. These regions exhibit high levels of anthropogenic activity, including industrial emissions, traffic, and biomass burning, which supply both NO_x and NMVOCs in large quantities (Hallquist et al., 2016). Observational and modeling studies have consistently shown elevated PAN mixing ratios over these areas (Fischer et al., 2014, Fadnavis et al., 2014).

Due to its stability under cold conditions and photochemical production pathways, PAN is widely recognized as a valuable tracer of polluted air masses. It has been used extensively to track the long-range transport of emissions, particularly from East Asia to North America. Satellite measurements from instruments such as the Infrared Atmospheric Sounding Interferometer (IASI) have confirmed that PAN is transported across the North Pacific. These findings highlight the role of PAN in contributing to ozone levels over the western United States, having impact in the air quality (Zhai et al., 2024).

Within the context of the ASM, PAN is especially relevant. During the monsoon season, strong convective activity enables the vertical transport of boundary layer air from South and Southeast Asia into the UTLS. Fadnavis et al., 2014 have documented enhanced PAN levels within the ASM anticyclone, with distinct uplift pathways associated with convective zones over the South China Sea and the southern slopes of the Himalayas. These PAN-rich air masses, originating from both Indian and Chinese emissions, are subsequently redistributed over large distances within the monsoon circulation system (Fadnavis et al., 2014, Wetzel et al., 2021, Ungermann et al., 2016).

PAN has also become a key trace gas for remote sensing due to its importance in atmospheric chemistry and transport. It was first globally retrieved from limb emission spectra using the MIPAS (Michelson Interferometer for Passive Atmospheric Sounding) instrument on the Envisat satellite, which revealed significant PAN plumes at altitudes between 8 km and 16 km extending across continents. These early observations established its broad spatial distribution (Glatthor et al., 2007). This retrieval and observation of PAN in the UTLS with MIPAS was continued with its airborne successor GLORIA, particularly within the context of long-range transport. These measurements have further confirmed PAN's value as a diagnostic tracer for analyzing atmospheric composition and transport dynamics (Wetzel et al., 2021, Johansson et al., 2022, Johansson et al., 2024, Ungermann et al., 2016).

2.3.2 Dichloromethane as Ozone Depleting Compound

Dichloromethane (CH_2Cl_2, see Figure 2.6), a chlorine-containing very short-lived substance (Cl-VSLS), has gained attention as a growing contributor to stratospheric ozone depletion in the last two decades. While the compound has a relatively short tropospheric lifetime of approximately 168 days and a stratospheric lifetime of 1–2 years outside the polar regions, it has been shown to reach the stratosphere under suitable transport conditions, particularly through deep convection in the tropics and monsoon systems (Hossaini et al., 2017, Hossaini et al., 2019, Pan et al., 2024). Its atmospheric sink is dominated by reactions with hydroxyl radicals (OH). In the tropical tropopause layer (TTL), its lifetime may extend to 6–10 months, providing ample time for upward transport (Lauther et al., 2022, Park et al., 2010).

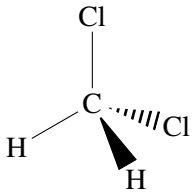

Figure 2.6: Structural formula of a CH_2Cl_2 molecule

Despite its short atmospheric lifetime, CH_2Cl_2 is especially concerning, because it is not regulated under the Montreal Protocol, which has otherwise effectively limited emissions of long-lived ozone-depleting substances (Hossaini et al., 2015). Consequently, increasing emissions of CH_2Cl_2 have been predicted to offset the expected ozone recovery, particularly in the Southern Hemisphere. If global emissions remain at 2019 levels, CH_2Cl_2 could delay Antarctic ozone recovery by up to five years (An et al., 2021). Moreover, its increasing role in tropical lower stratospheric ozone loss has been identified in recent chemistry–climate model simulations, which estimate that very short-lived substance emissions may account for up to a quarter of the observed tropical ozone decline between 1998 and 2018 (Villamayor et al., 2023).

The primary sources of CH_2Cl_2 are anthropogenic, with industrial applications including its use as a solvent for cleaning and adhesives and as a feedstock for hydrofluorocarbon (HFC) production (Hossaini et al., 2015; An et al., 2021). While small amounts may be of natural origin, it is estimated that more than 90% of global emissions are human-derived (Lauther et al., 2022). A notable rise

in CH_2Cl_2 emissions has occurred over the last two decades. Global emissions increased from 231 Gg/year in 2011 to 628 Gg/year in 2019, with over 85% of this increase attributed to solvent use. CH_2Cl_2 emissions from China make the greatest part of the global total, with the eastern provinces, including the North China Plain and the Yangtze River Delta, being identified as major hotspots (An et al., 2021).

The ASM system plays a key role in transporting CH_2Cl_2 from its South and East Asian source regions into the stratosphere. Strong convective uplift within the AMA allows for efficient vertical transport of boundary layer air to the UTLS, particularly above regions such as Northern India, the Tibetan Plateau, and eastern China (Lauther et al., 2022). Air parcels carrying CH_2Cl_2 are lifted and subsequently spiral upward within the AMA to 370 K-400 K, from where they exit eastward along the subtropical jet stream, eventually reaching the extratropics over the Pacific and Atlantic Oceans (Lauther et al., 2022).

This process was illustrated during the ACCLIP campaign in 2022, which observed record-high CH_2Cl_2 concentrations, up to 600 pptv near the tropopause in convective outflow layers above East Asia. These extreme values were attributed to the alignment of deep convection with intense surface emissions from industrial hubs (Pan et al., 2024). Similarly, prior campaigns such as StratoClim have confirmed the presence of CH_2Cl_2 in the ASM region and its role in transporting pollutants from rapidly industrializing Asian nations into the UTLS (Adcock et al., 2021).

Beyond Asia, rising CH_2Cl_2 concentrations have also been measured across North America. Long-term aircraft observations between 2000 and 2022 show increasing mixing ratios of CH_2Cl_2 at all tropospheric altitudes, with evidence of some transport into the lower stratosphere, though its abundance declines sharply above 15 km due to its short-lived nature (Smith et al., 2024). Compared to the efficient and rapid transport within the ASM system, North American emissions appear to have a weaker impact on stratospheric chlorine levels due to both lower emission rates and slower transport pathways (Lauther et al., 2022).

Climate projections suggest that warming-induced intensification of monsoon convection, particularly in East and South Asia, will enhance the vertical transport of CH_2Cl_2, further increasing its stratospheric influence. Among global monsoon systems, the East Asian summer monsoon (EASM) is projected to be the most sensitive to global warming, potentially amplifying CH_2Cl_2 contributions to stratospheric chlorine loading and ozone depletion (Pan et al., 2024).

Taken together, CH_2Cl_2, though short-lived, is a growing and significant factor in stratospheric ozone chemistry, especially in the context of unregulated emissions and enhanced vertical transport from Asian monsoon systems. As emissions of long-lived chlorinated substances continue to decline under the Montreal Protocol, the relative contribution of Cl-VSLSs like CH_2Cl_2 is expected to rise, making it more important to observe its emission, distribution and impact on the composition of troposphere and stratosphere. (Lauther et al., 2022, Villamayor et al., 2023).

3 Instrument, Data and Methods

3.1 GLORIA Instrument

The Gimballed Limb Observer for Radiance Imaging of the Atmosphere (GLORIA) is an advanced airborne infrared limb imager developed jointly by the Karlsruhe Institute of Technology (KIT) and the Forschungszentrum Jülich (FZJ) to investigate the chemical and dynamical processes in the UTLS. This region plays a crucial role in the Earth's climate system, and even minor changes in its composition can have significant impacts on the radiation budget, weather, stratospheric ozone and chemical equilibrium. GLORIA enables high-resolution measurements of trace gases, temperature fields, and cloud structures in this critical atmospheric layer (Riese et al., 2014, Friedl-Vallon et al., 2014).

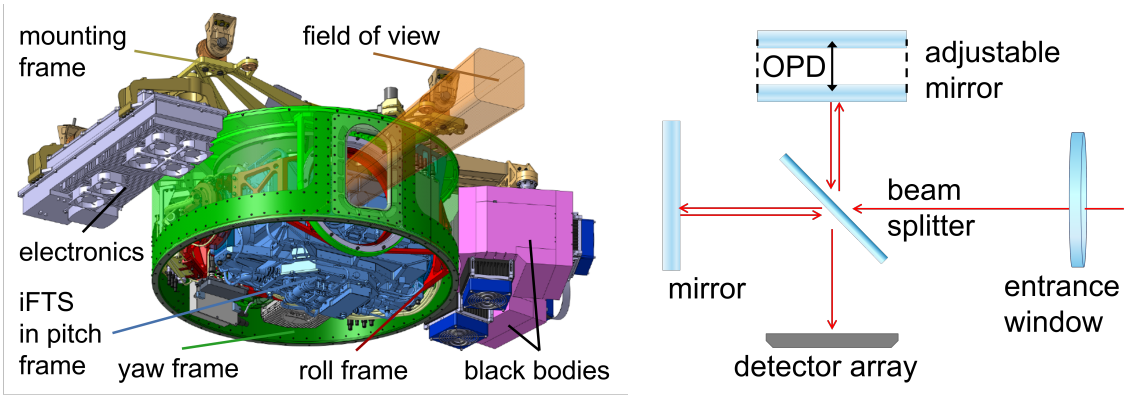

(a) (b)

Figure 3.1: Instrumental setup of GLORIA in (a), Figure from Friedl-Vallon et al., 2014 with added labels, and principle of a Michelson Interferometer in (b). Setup of the GLORIA instrument, The instrument observes spectral information in form of interferograms, which are generated by directing incoming infrared radiation (i.e. the thermal emission of the atmosphere) through a beam splitter onto two mirrors. The reflected beams interfere with each other and are detected. The interferogram is obtained through the variable optical path difference (OPD), which is controlled by the position of one of the mirrors. The spectrometer is embedded in a gimbal frame to stabilize and direct the instrument's line-of-sight. Furthermore, GLORIA inlcudes two black bodies for calibration.

Designed for deployment aboard high-altitude research aircrafts and stratospheric balloons, GLORIA (Figure 3.1a) combines the principle of a Michelson interferometer (Figure 3.1b) with a two-dimensional detector array to record atmospheric emission with both high spatial and spectral resolution. The system incorporates an actively cooled imaging Fourier transform spectrometer (IFTS), which is mounted in a gimbal frame. This configuration allows for flexible adjustments of the instrument's line-of-sight in azimuth and elevation, enabling optimized limb- and nadir-viewing

geometries (Friedl-Vallon et al., 2014). The optical setup includes a dielectric beam splitter, a fixed and a moving mirror and an imaging detector array, consisting of 128 x 128 pixels of which 48 x 128 are used. The optical components of the spectrometer are cooled with dry ice to about 215 K to improve the sensitivity of the instrument (Piesch et al., 2015, Friedl-Vallon et al., 2014). With the help of an inertial navigation system, the gimballed frame is used to stabilize and direct the line-of-sight of the instrument in the required viewing limb-viewing geometry. Azimuth panning is possible to adjust the viewing direction along atmospheric features of interest or to enable tomographic observations, and also nadir observations are possible (Friedl-Vallon et al., 2014).

GLORIA is typically operated in two main modes: chemistry mode, which prioritizes high spectral resolution to support retrievals of a wide range of trace gases, and dynamics mode, which favors dense horizontal sampling for tomographic observations to study atmospheric motion and structure. In this work, only chemistry mode data is used. In this mode, the instrument achieves a spectral sampling of approximately 0.0625 cm^{-1}, a 12.8 s temporal sampling and high vertical resolutions of a few hundred meters, allowing for detailed curtain observations of trace gas distributions along the flight path (Riese et al., 2014, Friedl-Vallon et al., 2014).

The instrument's measurement principle is based on the recording of interferograms which are transformed into infrared limb emission spectra. Thereby, the line-of-sight is oriented tangentially to Earth's surface. This limb geometry (Figure 3.2) maximizes sensitivity to weakly abundant species due to the extended path length through the atmosphere and allows to detect the weak thermal emission of these trace gases in front of the cold background of deep space (Riese et al., 2014). The vertical structure of the atmosphere is inferred by resolving emissions originating from different tangent altitudes across the detector array (Friedl-Vallon et al., 2014).

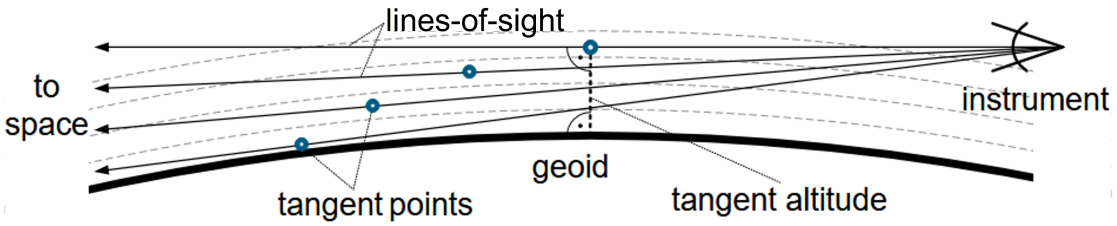

Figure 3.2: Limb Geometry for remote sensing with GLORIA. The tangent points are the location of the points on the line-of-sight, which are closest to the Earth's surface. From the region around the tangent points, usually most information is collected at the respective altitude levels. This schematic is from Riese et al., 2014

Radiometric and spectral calibration is critical to the data processing chain. GLORIA enables in-flight measurements for calibration using two on-board black bodies at different stabilized temperatures, along with "deep-space" observations at an upward viewing angle of approximately 10°. Calibration measurements are performed every 15 minutes during flight (Friedl-Vallon et al., 2014).

The data processing begins with level 0 processing, where raw interferograms, one for each of the 48×128 detector pixels, are corrected for spikes, detector non-linearities, and phase drifts. Then, the interferograms are resampled from a time- to a space-equidistant grid using laser-based path

difference information and spectral calibration parameters. This is followed by level 1 processing, which includes Fourier transformation and complex radiometric calibration, resulting in calibrated spectral radiances (Kleinert et al., 2014, Ungermann et al., 2022). In order to limit the size of the microwindows for the retrieval, the spectra are apodized using Norton-Beer-strong apodization (Norton and Beer, 1976, 1977).

For the retrieval of atmospheric state parameters, the radiative transfer model KOPRA (Karlsruhe Optimized and Precise Radiative transfer Algorithm, Stiller, 2000, 2002) in combination with the KOPRAFIT inversion algorithm (Höpfner et al., 2001) is used. These tools enable the estimation of temperature and trace gas profiles by iteratively fitting modelled spectra to the observations, based on an initial guess derived from climatological data or numerical weather prediction output (Stiller, 2000, Johansson et al., 2018). As clouds are optically thick in the infrared, GLORIA cannot provide reliable data below the edge of the cloud layer. Cloud influenced data are filtered using either spectral indices or derivative-based methods, ensuring robust retrievals (Woiwode et al., 2015, Johansson et al., 2018). This retrieval strategy has proven effective in resolving vertical distributions of temperature and key trace species such as ozone, nitric acid, organic compounds, PAN, chlorinated compounds, ammonium nitrate and water vapor with high accuracy (e.g. Höpfner et al., 2019, Wetzel et al., 2021, Johansson et al., 2018, Johansson et al., 2022).

3.2 PHILEAS Campaign

Figure 3.3: GLORIA deployed in the belly pod of HALO in Oberpfaffenhofen during the first phase of PHILEAS

The PHILEAS campaign (Probing HIgh Latitude Export of Air from the Asian Summer Monsoon) was conducted with the research aircraft HALO (High Altitude and LOng-Range Aircraft) operated by German Aerospace Center (DLR). PHILEAS took place in summer and early autumn 2023 and was specifically designed to address the observational deficit as described in the introduction in Chapter 1, by providing in-situ and remote sensing data over this critical region (Riese, 2025 (in prep.)).

The campaigns twenty research flights were carried out in two phases from bases in Oberpfaffenhofen, Germany and later in Anchorage, Alaska. The first mission phase from Oberpfaffenhofen focused on the investigation of the displaced lower boundary of the AMA and the Asian Tropopause Aerosol Layer over the Eastern Mediterranean region. The second phase took place from Anchorage, Alaska. It aimed to explore the long-range eastward transport of moist and polluted air masses from the AMA into the UTLS. The focus was on determining the main transport pathways, associated timescales, and the impact of this transport on the extratropical LMS. In Figure 3.4 all flight tracks of this Alaska campaign phase can be seen.

One observation of this phase was the occurrence of a strong Rossby wave breaking event between 24–27 August 2023. This dynamic event triggered large-scale stirring, resulting in significant filamentation and the eventual mixing of AMA-influenced air masses into the lower stratosphere (Riese, 2025(in prep.)). First results from the campaign revealed long-range transport processes of AMA-influenced air masses reaching high latitudes. These air masses contained aerosols, as well as very short-lived substances containing chlorine and bromine. Of particular note were the observed concentrations of CH_2Cl_2 in the upper troposphere, which exceeded 300 pptv in some regions (Jesswein et al., 2025, Riese, 2025 (in prep.), Woiwode et al., 2025). The observations also underscore the importance of eddy shedding and filaments originating at higher altitudes from the AMA and also at lower altitudes by tropospheric transport from the ASM region. These features facilitate the exchange of trace gases and aerosols across the tropopause and contribute to the chemical composition of the LMS.

The GLORIA instrument is deployed in the belly pod of the HALO research aircraft. It views to the right-hand-side of the flight direction and provides profiles of temperature and trace gases from the flight altitude down to the top of the cloud layer (see Section 3.1). The limb-viewing geometry of GLORIA makes it particularly well-suited for studying fine-scale dynamical processes and trace gas structures, especially during high-altitude flight segments where the instrument can cover as much vertical range as possible. The higher altitudes can only be reached with HALO towards the end of the flights, as less fuel makes the aircraft lighter.

The analysis presented in this thesis is based on data collected during four research flights of the PHILEAS campaign. These flights were selected because of their tracks crossing air with large fractions of air from the ASM region. In these GLORIA detected filaments enriched with the trace gases PAN and CH_2Cl_2 (see Chapter 4). The flight tracks and corresponding flight levels are illustrated in Figure 3.5. The execution of the flights deviated only slightly from the planned routes. Only the actual altitudes did not fully match the specified flight levels, and in Flight 17, the point at the end of the FL470 leg was shifted slightly further to the east.

Flight 8 on 26–27 August 2023 targeted a filament of ASM-influenced air masses extending across the North Pacific into Alaska. According to the flight report by Christian Rolf, the mission was designed to intersect both ASM and non-ASM air along multiple legs, allowing for a detailed investigation of air mass composition and structure.

Table 3.1: Summary of flights relevant for this thesis from the second PHILEAS campaign phase from Anchorage, Alaska, after Riese, 2025 (in prep.) and the Flight Reports.

Flight	Alias	Aim	Start	End
F08	Gilching	Sample ASMair over Alaska and Pacific, mixing into the lower stratosphere	2023-08-26 17:58 UTC	2023-08-27 02:13 UTC
F09	Hambach	Revisit air masses from Flight 8	2023-08-28 18:19 UTC	2023-08-29 02:55 UTC
F16	Offenburg	Probe filament of Asian monsoon air over the Pacific at different altitudes	2023-09-15 22:06 UTC	2023-09-16 07:09 UTC
F17	Paderborn	Revisit air masses from Flight 16	2023-09-16 22:00 UTC	2023-09-17 06:30 UTC

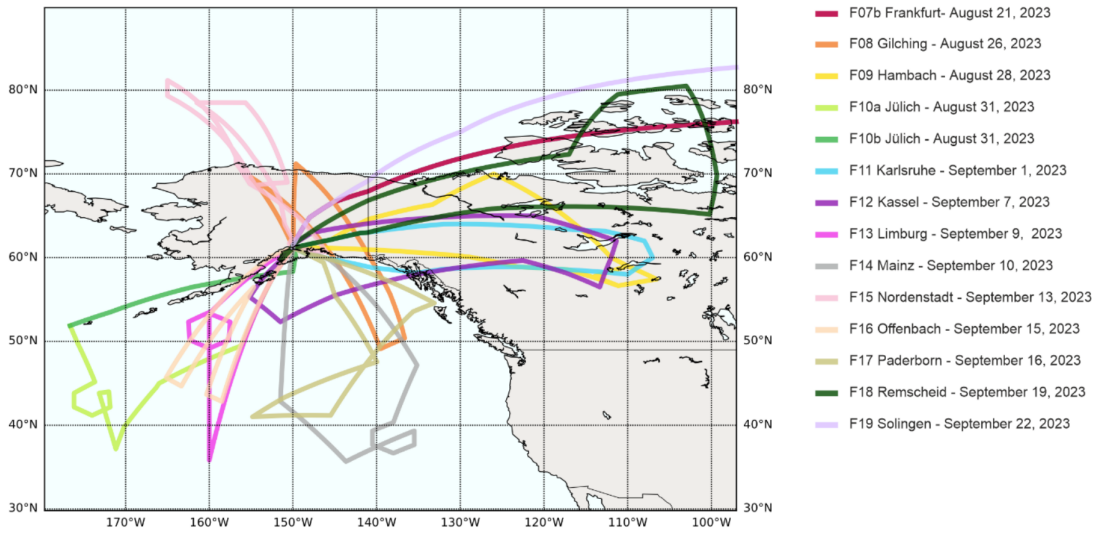

Figure 3.4: Map of the PHILEAS flight tracks from Anchorage (Alaska). For this thesis the data from Flight 8 on 26–27 August 2023 , Flight 9 on 28–29 August 2023 , Flight 16 on 15–16 September 2023 and Flight 17 on 16–17 September 2023 are used. This figure is from Riese, 2025 (in prep.).

During the initial northeast-bound segment, the aircraft sampled air masses near the northern edge of the filament at relatively low altitudes, transitioning into regions without apparent monsoon influence. The southeast-bound leg was dedicated to probing ASM air at multiple vertical levels. However, only the northwest segments from the fourth flight leg onward were measured in chemistry mode, where both PAN and CH_2Cl_2 data are available, and thus are are suitable for further analysis in this thesis. This portion of the flight provided optimal conditions for remote sensing with the GLORIA instrument due to reduced cloud cover and sufficient observational altitude.

During this segment, both in-situ and remote sensing measurements revealed significant evidence of mixing processes in the LMS. Notably, elevated concentrations of ammonium nitrate and ozone were observed just below the flight level around 01:15 UTC, indicating active mixing of tropospheric

air into the LMS (Riese, 2025 (in prep.)). This interpretation is further supported by increased levels of CH_2Cl_2, a tracer of anthropogenic origin (see Section 2.3), as presented in Woiwode et al., 2025 and Riese, 2025 (in prep.).

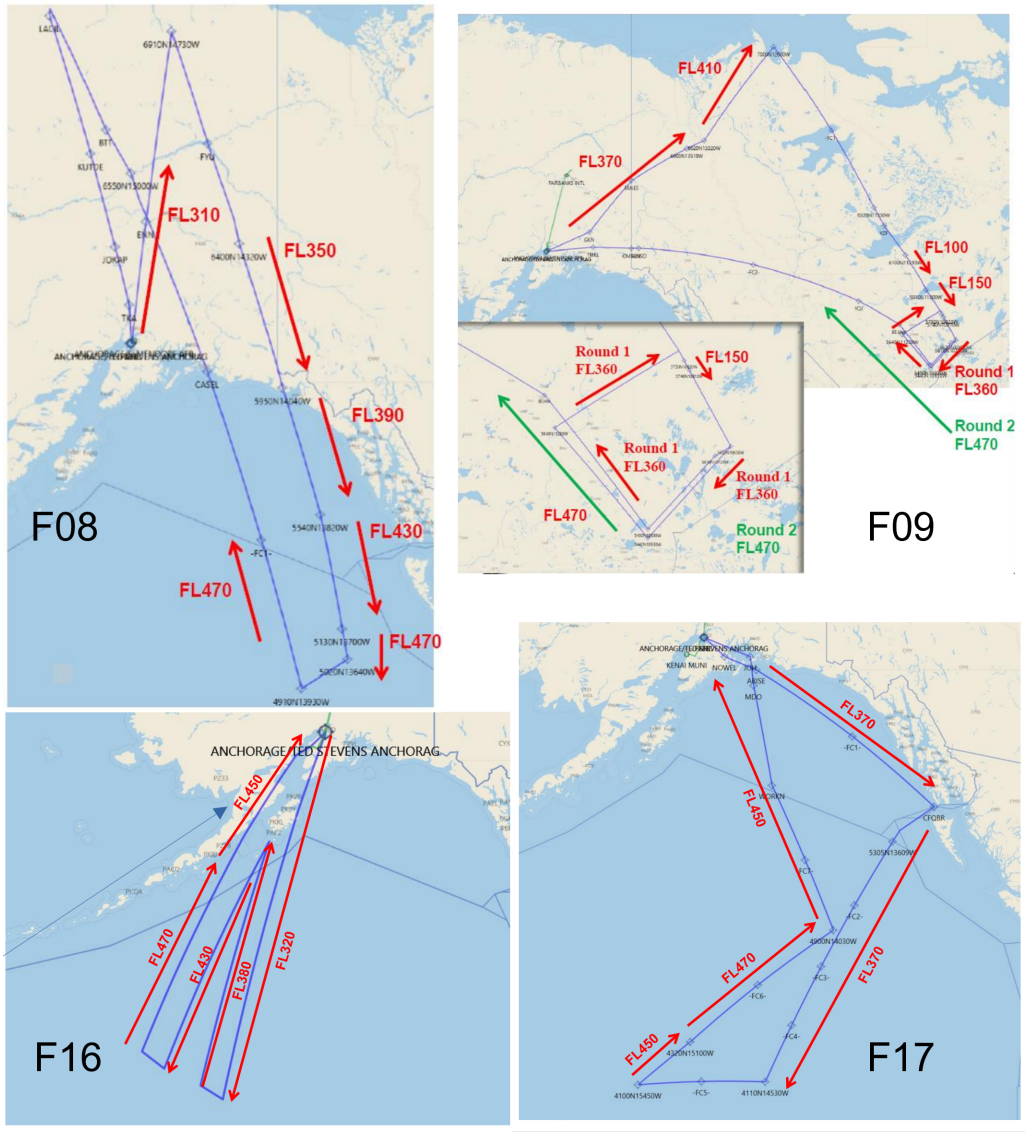

Figure 3.5: Flight plans of Flight 8 on 26–27 August 2023 , Flight 9 on 28–29 August 2023 , Flight 16 on 15–16 September 2023 and Flight 17 on 16–17 September 2023 with the targeted flight levels (FL). All flights started in Anchorage, Alaska and sampled air masses over the North Pacific, Alaska and Canada. For Flight 9 a loop at the southeastern edge was planned to probe the same air masses on different heights. These flight plans are from the respective flight protocols of PHILEAS.

Flight 9 on 28–29 August 2023 included a south-easternmost excursion with a loop structure designed to sample air masses affected by intense Canadian wildfires. These air masses were targeted at various altitudes to investigate their vertical distribution and potential influence on UTLS composition. Although this looping section was not captured in the vertical cross-sections derived from GLORIA observations, it provided important in-situ data for assessing the chemical properties of wildfire-affected air.

Flight 16 on 15–16 September 2023 yielded, due to the presence of clouds, usable data from GLORIA starting from the second leg heading south. It was during this segment that the aircraft reached higher altitudes for GLORIA observations, allowing for effective and largely cloud-free remote sensing of the filamentary monsoon outflow structures.

Flight 17 on 16–17 September 2023 featured a southbound segment performed at two distinct flight levels in its easterly portion, traversing a region with elevated concentrations of Asian tracers on isentropic surfaces. The return leg to the northwest was executed at higher altitudes to intercept air masses formerly influenced by the AMA, which again was most usable for the GLORIA observations. The final segment of the flight was strategically designed to investigate a shear zone located south of Anchorage, offering insights into dynamical mixing processes near the tropopause.

Together, these four flights provide complementary perspectives on ASM-related transport and mixing, capturing outflow at various stages across the Pacific. These case studies form the basis for the detailed analyses in Chapter 4.

3.3 ICON-ART Surface Tracer

The surface tracer analysis employed in this study was adapted by Sören Johansson, drawing upon the established methodology of emission tracers developed for the Chemical Lagrangian Model of the Stratosphere, CLaMS (Vogel et al., 2019 and references therein), and implementing a similar approach within the ICON-ART framework. This adaptation allows for the investigation of air mass origins and boundary layer contributions. Figure 3.6 illustrates the specific boundary layer source regions applied in the tracer configuration.

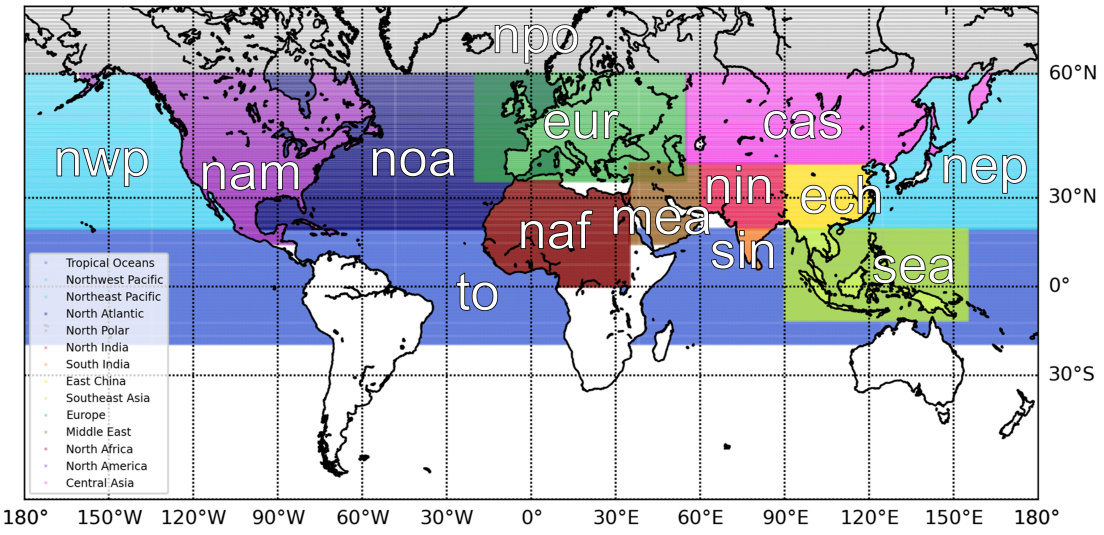

Figure 3.6: Map of the boundary layer regions for the surface tracers used with ICON-ART. The definition of the regions was largely taken from Vogel et al., 2024 with more precision on coastlines and a focus to the northern hemisphere. The abbreviations for the regions can also be seen in 3.2. Figure from Sören Johansson with added abbreviations.

Table 3.2: Abbreviations and corresponding regions for the map of ICON-ART surface tracers (Figure 3.6). The additional combined tracer India/China = nin + sin + ech is not in the map

Abbreviation	**Region**	**Abbreviation**	**Region**
nin	North India	nam	North America
sin	South India	nep	Northeast Pacific
ech	East China	nao	North Atlantic
cas	Central Asia	eur	Europe
to	Tropical Oceans	mea	Middle East
nwp	Northwest Pacific	naf	North Africa
sea	Southeast Asia	npo	North Polar region

The foundational concept of surface emission tracers was originally introduced in studies using the CLaMS model to investigate the influence of various regional emissions on the composition of the Asian monsoon anticyclone (Vogel et al., 2015, 2016 and 2019). In the CLaMS framework, tracer simulations are driven by wind fields from the ERA-Interim reanalysis, with artificial, inert tracers injected into the model's boundary layer. These emission tracers are region-specific and used to tag air masses based on their geographical origin. In Table 3.2 a list of the region abbreviations explains the labels of Figure 3.6.

A key aspect of the CLaMS emission tracer approach is the division of the ASM influenced boundary layer into distinct regions of interest, notably northern India (NIN), southern India (SIN), eastern China (ECH), and Southeast Asia (SEA). These regions were selected based on their potential to contribute to monsoon-related outflow, with NIN, SIN, and ECH sometimes combined under a broader category referred to as "India/China." Each tracer is initialized with a value of one within its designated region and zero elsewhere. As the simulation progresses, these tracers are passively transported by the modeled wind field and subject to mixing, allowing for the quantification of air mass origin and dilution. The resulting tracer concentrations represent the fraction of an air mass that originated from a specific region. It is important to note that this methodology is only sensitive to young air masses and does not account for aged contributions from the free troposphere or stratosphere (Vogel et al., 2016).

The ICON model (ICOsahedral Nonhydrostatic weather- and climate model) operates on a global-to-regional modeling scale with capabilities for local grid refinement acts as core meteorological driver, designed for high-resolution and accurate atmospheric simulations. Developed to simulate interactions between aerosols, trace gases and the atmospheric state across weather and climate timescales, the ART (Aerosols and Reactive Trace gases) extension module (Rieger et al., 2015) provides the framework to implement the surface emission tracer concept.

ICON-ART includes a flexible tracer infrastructure that supports the definition and implementation of artificial, passive tracers tailored to specific scientific objectives (Schröter et al., 2018). These tracers are initialized at a designated time step and subsequently evolve purely under the influence of atmospheric transport processes—without any sources, sinks, or chemical interactions. This

makes them particularly useful for studying the advection and dispersion of air masses, as in the case of boundary layer origin tracers.

Tracer metadata and configurations in ICON-ART are managed via XML inputs, providing researchers with a highly customizable setup for defining tracer properties and initialization conditions. In the context of this thesis, surface tracers were defined analogously to those in the CLaMS approach, with the aim of tagging specific boundary layer regions and tracking their contribution to upper tropospheric and lower stratospheric air composition. The ICON-ART simulations used in this thesis employed ICON standard configuration of 90 terrain-following vertical levels extending from the surface up to approximately 75 km. Surface tracers were initialized on 1 May 2023 with a value of 1 at the lowest model level in the respective tracer regions. The model was run in a sequence of short, freely evolving 24-hour forecast cycles. At the end of each 24-hour period at 6 UTC, only the meteorological fields were reinitialized using the operational analysis, while the tracer fields continued without reset. Through the ICON-ART system's ability to simulate passive tracer transport with high spatial resolution and forecast quality, this adaptation provides a tool for analyzing air mass pathways and regional influences on atmospheric composition.

3.4 Backward Trajectories with HYSPLIT Model and ERA5 Reanalysis Data

Backward trajectory modeling using the Hybrid Single-Particle Lagrangian Integrated Trajectory model (HYSPLIT) by NOAA (National Oceanic and Atmospheric Administration) is a widely used method for tracing the origins of trace gases and understanding atmospheric transport processes (Stein et al., 2015,). Its calculation method is a hybrid between the Lagrangian approach, observing the transport in the reference system of one particle or air parcel for advection and diffusion processes, and the Eulerian approach, which calculates pollutant air concentrations in reference of the flow field. It is used for computing simple air parcel trajectories as well as complex transport and dispersion processes Stein et al., 2015). The ERA5 reanalysis dataset from the European Centre for Medium-Range Weather (ECMWF) is globally complete and consistent and the successor of ERAInterim, released in 2018. It assimilates model simulation output together with observation data and is available for from 1940 to the present and for pressure levels from 1000 hPa to 1 hPa (Hersbach et al., 2020, Copernicus Climate Change Service, 2018).

Using backward trajectories from HYSPLIT with the meteorological input from ERA5 reanalysis data is a widely used method for tracing the origins of trace gases and understanding atmospheric transport processes (e.g. Vogel et al., 2024). However, this approach is not without limitations, which arise from both the ERA5 reanalysis data and the HYSPLIT model itself. The accuracy of HYSPLIT trajectories is heavily dependent on the quality of the input meteorological data. Errors in ERA5, such as biases in moisture, temperature or uplift speeds (Bourguet and Linz, 2022, Vogel et al., 2024), can propagate into the trajectory calculations.

The mean effective ascent rates derived from ERA5 back trajectories are in good agreement with the observation-based mean ascent rates. With better spatial and temporal resolution, the ERA5 reanalysis data yield a better representation of convection than its predecessor ERAInterim. This dependency on the resolution, especially temporal, leads still to a poorer performance of a ERA5 dataset with e.g. 6 h or 12 h resolution than 1 h (Vogel et al., 2024, Bourguet and Linz, 2022, Hoffmann et al., 2019).

ERA5 reanalysis data, while highly advanced, has limitations in its spatial and temporal resolution that can impact backward trajectory modeling. ERA5 operates at a horizontal resolution of approximately 31 km on a grid of $0.25^\circ \times 0.25^\circ$ (Copernicus Climate Change Service, 2018), which may not capture small-scale meteorological features such as localized convection or terrain-induced flow (Hoffmann et al., 2019, Bourguet and Linz, 2022).

Although ERA5 provides hourly data (Copernicus Climate Change Service, 2018), the temporal resolution of certain meteorological parameters may still be insufficient to resolve rapid changes in atmospheric conditions, such as those occurring during intense convective events. This can result in trajectory errors, particularly in regions with high diurnal variability (Hoffmann et al., 2019).

ERA5's vertical resolution, while improved compared to its predecessor ERA-Interim, may still fail to accurately represent sharp gradients in the atmosphere, such as those near the tropopause or within the boundary layer. Vogel et al., 2024 indicate that ERA5 still struggles with accurately representing the intensity and vertical extent of deep convection, particularly in regions with complex terrain such as the Tibetan Plateau. For instance, the mean age of air derived from ERA5 is too old above 430 K, suggesting that the model may underestimate the efficiency of rapid uplift in the upper troposphere. A slower ascend rate and higher mean age of air in the tropical lower stratosphere and in the upper tropical tropopause layer are reported by Ploeger et al., 2021. This can affect the accuracy of trajectory calculations in these critical regions, e.g. the uplift in the ASM system and further transport into tropical regions and the stratosphere. ERA5 exhibits biases for the wind speed at lower altitudes, influenced by local terrain (Potisomporn et al., 2023), which can lead to errors in trajectory calculations near to the ground and the distribution of trace gases.

4 Results and Discussion

4.1 Cross Sections from GLORIA Measurements

This section presents and discusses in 4.1.1 the retrieved vertical cross sections from four flights of the PHILEAS campaign, as they are described in Section 3.2, and characterizes the GLORIA retrievals in 4.1.2. As introduced in Section 2.3 the analysis for this thesis focuses on the retrievals of PAN as a tracer for burning processes and CH_2Cl_2 as a tracer for anthropogenic emissions. Both trace gases are here used as indicators for air masses from the ASM System. For detailed analysis of the origin of the discussed air masses see Section 4.3.

4.1.1 Retrieved Cross Sections for PAN and Dichloromethane

The retrieved cross sections from GLORIA observations show as atmospheric parameters the Volume Mixing Ratios (VMRs) for specific chemical species, here CH_2Cl_2 and PAN, on the retrieval grid with the time stamp, equivalent to the distance the aircraft has moved, in UTC on the horizontal. Data gaps are due to the calibration procedure every 15 min (Friedl-Vallon et al., 2014) or measurements conducted in dynamic mode. The dynamic mode is usually visible through the larger gaps in the cross sections of the chemistry mode. Moreover, retrievals are filtered based on vertical resolution thresholds and the assessed quality of the results. Turns in the flight pattern are also the cause of filtering out vertical profiles in the retrieval curtain. As described in Section 3.1 the cloud influenced interferograms have to be filtered out. This can be seen as the lower edge of the cross sections. The highest retieval values at the edge of the cloud layer should be interpreted with caution, as clouds are optically thick and therefore have a strong signal in the IR. Single detector pixels can exhibit nonlinear effects due to the readout electronics, which is why neighboring pixels may, but do not necessarily, be affected by the clouds. Therefore uncertainties in these regions are expected to be higher than it can be seen in the error plots as these nonlinear effects cannot be included in the error estimation. A detailed discussion of the error sources is provided later in this section.

Figure 4.1 shows the vertical profiles of CH_2Cl_2 and PAN from Flight 8 on 26–27 August 2023. Both trace gases exhibit an extended maximum in their VMR in the upper troposphere, observed between 22 : 30 UTC and 23 : 30 UTC, with a vertical extent from below 9 km up to 13 km. Additionally, PAN shows localized maxima around the dynamical tropopause between 00 : 15 UTC and 01 : 45 UTC. Overall, the enhanced concentration of both species exhibit similar structural distributions. In the extended tropospheric maximum PAN reaches approximately peak values

up to 600 pptv and for CH_2Cl_2 a maximum of up to 300 pptv with very similar shape is observed. Furthermore, both species show localized stratospheric maxima (for explanation regarding the use of this term, refer to Section 4.4.2) between 13 km and 14.5 km. In the cross section of CH_2Cl_2, these features are evident between 23 : 40 UTC and 00 : 10 UTC, as well as from 01 : 15 UTC to 01 : 30 UTC. In PAN they show structures from 23 : 40 UTC to 00 : 40 UTC and from 01 : 15 UTC to 01 : 45 UTC.

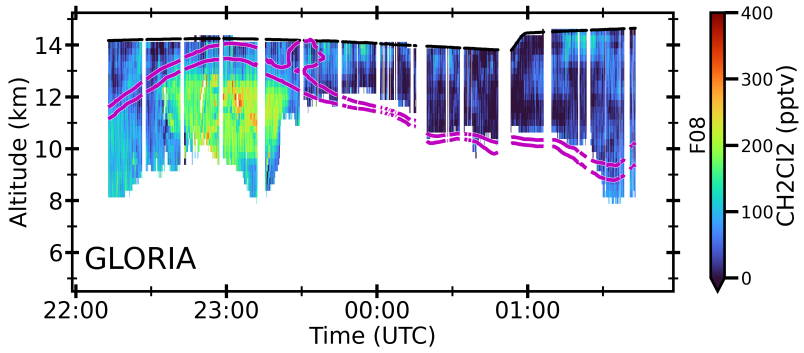

(a) CH_2Cl_2 profile for Flight 8 on 26–27 August 2023

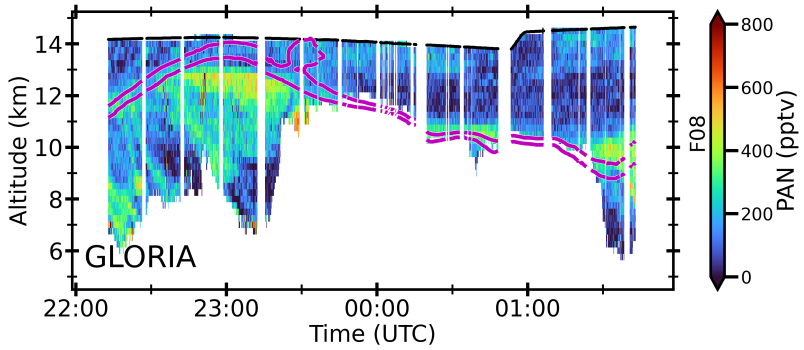

(b) PAN profile for Flight 8 on 26–27 August 2023

Figure 4.1: CH_2Cl_2 and PAN vertical cross sections in pptv from GLORIA for Flight 8 on 26–27 August 2023. On the x-axis is the time stamp in UTC of the retrieved profile. This corresponds to the flight track. On the y-axis is the altitude in km, beginning above the boundary layer at about 5 km up to 15 km. The color bar represents the VMR in pptv with the maximum value depending on the species. The dynamical tropopause is marked in violet with the PV = 2 PVU and PV = 4 PVU lines from ECMWF interpolated on the tangent points.

During Flight 9, conducted two days later on 28–29 August 2023, tropospheric air masses were sampled, showing CH_2Cl_2 maxima of up to 275 pptv. Figure 4.2(a) displays two prominent maxima between 9 km and 13 km: the first occurring between 20 : 30 UTC and 21 : 20 UTC, and the second between 00 : 00 UTC and 01 : 00 UTC. The PAN distribution in Figure 4.2 (b) exhibits a similar structure, with the notable exception that it reaches its highest values, exceeding 700 pptv, within a third maximum, located between 00 : 45 UTC and 01 : 45 UTC at altitudes of 8 km to 11 km. This observation will be further examined in the discussion, Section 4.4.1.

For Flight 16 on 15-16 September 2023, shown in Figure 4.3, the maxima of CH_2Cl_2 and PAN largely coincide. CH_2Cl_2 exhibits higher values of up to 200 pptv between 8 km and 9 km from 04 : 15 UTC and 04 : 45 UTC, while PAN presents a local minimum in this region and has its peak

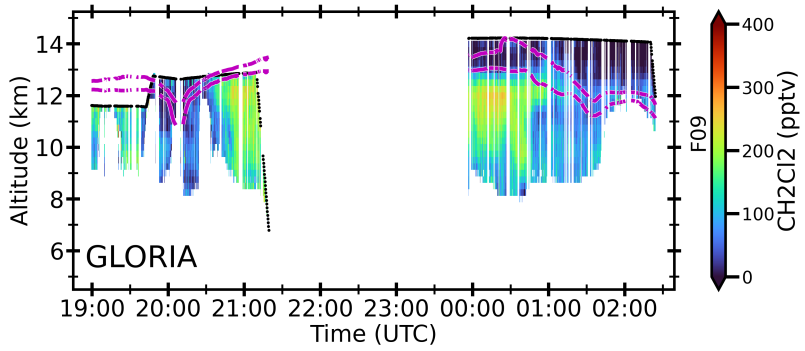

(a) CH_2Cl_2 profile from Flight 9 on 28–29 August 2023

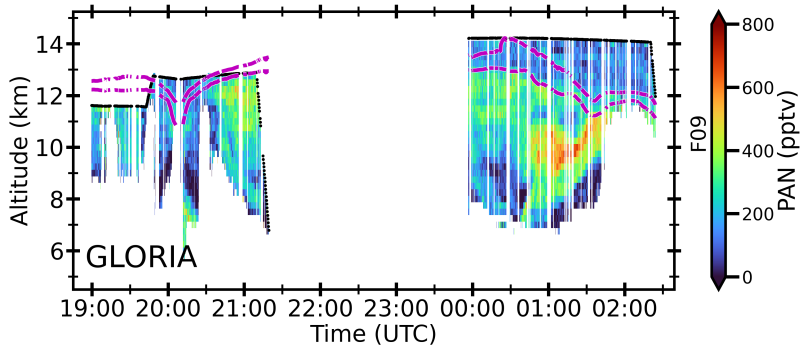

(b) PAN profile from Flight 9 on 28–29 August 2023

Figure 4.2: CH_2Cl_2 and PAN vertical cross sections in the same format as in Figure 4.1, but for Flight 9 on 28–29 August 2023

values of around 500 pptv at 12 km. The absolute highest values of 800 pptv between 23 : 30 UTC and 00 : 00 UTC are here ignored, as the larger gaps in the profiles make it difficult to interpret structure and reliability of the feature. The dynamical tropopause, defined for simplicity at the PV = 2 PVU isoline, exhibits a fold-like structure for the course of this flight, with the lower stratosphere reaching just up to 9 km in the north and the tropopause rising to altitudes of up to 15 km in the south. This flight was specifically designed to investigate turbulent air mixing at the jet stream boundary.

Flight 17 on 16-17 September 2023, shown in Figure 4.4 was conducted to resample air masses observed during Flight 16 on the day before. This Flight 17 again reveals a CH_2Cl_2 maximum in monsoon-influenced tropospheric air, reaching nearly 400 pptv between 8 km and 11 km, and between 02 : 00 UTC and 03 : 20 UTC. A second maximum above the previous reaches up to the flight altitude from 12 km to 14 km during an ascend of the aircraft. It shall be noted that, because of this, the maximum could also be sampled with the in-situ instruments on board of HALO. However a comparison of these measurements with the retrievals from GLORIA is not included in the analysis for this thesis. A similar structure as for the CH_2Cl_2 maxima for Flight 17 is observed for PAN, which reaches peak values of approximately 500 pptv. Additionally, PAN shows a distinct maximum near the lower tropopause, between 6 km and 9 km, occurring from 04 : 30 UTC to 06 : 00 UTC, which is not observed in CH_2Cl_2.

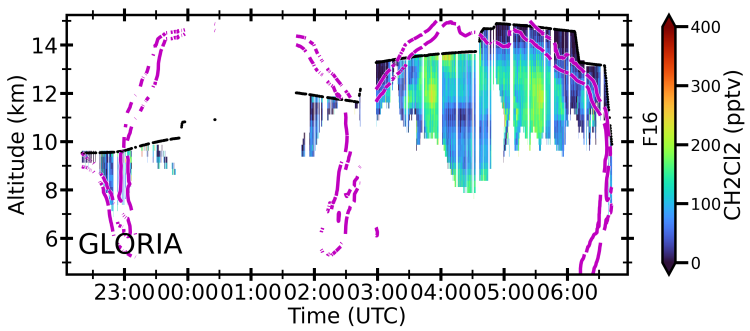

(a) CH_2Cl_2 profile from Flight 16 on 15-16 September 2023

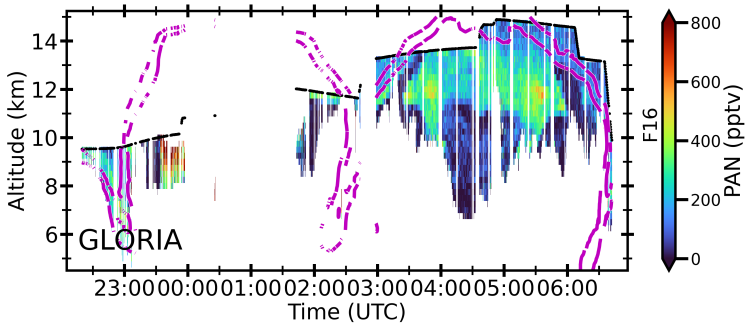

(b) PAN profile from Flight 16 on 15-16 September 2023

Figure 4.3: CH_2Cl_2 and PAN vertical cross sections in the same format as in Figure 4.1, but for Flight 16 on 15–16 September 2023

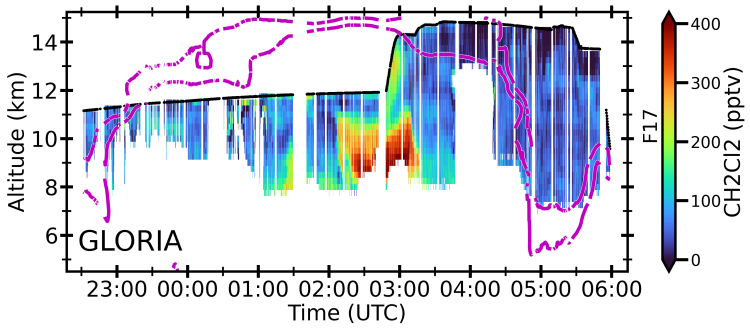

(a) CH_2Cl_2 profile for Flight 17 on 16-17 September 2023

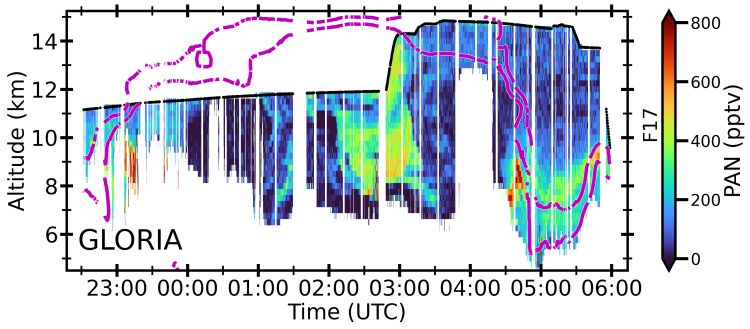

(b) PAN profile for Flight 17 on 16-17 September 2023

Figure 4.4: CH_2Cl_2 and PAN vertical cross sections in the same format as in Figure 4.1, but for Flight 17 on 16–17 September 2023

Air masses with elevated pollution concentrations PAN align for the most filaments with the maxima in CH_2Cl_2. However, three maxima in PAN VMR during Flight 8 on 26–27 August 2023 , Flight 9 on 28–29 August 2023 and Flight 17 on 16–17 September 2023 were observed to have no corresponding structure in CH_2Cl_2. In the cross sections for Flight 8 and Flight 17 these filaments are in the proximity of the PV = 2 PVU and PV = 4 PVU isolines.

4.1.2 Retrieval Characterization for Flight 8 on 26–27 August 2023

The uncertainties in the retrieved trace gas distributions are now analyzed, using Flight 8 on 26–27 August 2023 as an example, since similar error characteristics are expected for the other three flights. Thereby, the following sources of uncertainty were considered:

- A **1% gain error** and a **30** $\mathrm{nW\,cm^{-2}\,sr^{-1}\,cm}$ **offset error**, both of which have minimal impact since offset and gain were fitted (Ungermann et al., 2022)
- An **elevation pointing error** of 0.03° (Ungermann et al., 2022)
- A **temperature error** of 1 K for PAN (Johansson et al., 2018). For CH_2Cl_2 the temperature has been jointly fitted.
- A **spectroscopic error** due to unknown spectroscopic data for CH_2Cl_2 is 3.2% (Sharpe et al., 2004), as well as for PAN, which is adopted from the predecessor instrument MIPAS (Glatthor et al., 2007) and now applied to GLORIA retrievals

Ungermann et al., 2022 describes the pointing error and, to a lesser extent, the gain error as the main sources of uncertainties for measurements with GLORIA.

Figure 4.5 (a) presents a vertical profile of the CH_2Cl_2 VMR along with the estimated total error. The total error reaches its peak between 9 km and 10 km. Among the different error contributions, the pointing error, shown in green in Figure 4.6 (b), has the largest influence on the total error. The vertical resolution in Figure 4.5c maintains a relatively constant value of approximately 0.8 km between 9 km and 14 km.

In comparison, the vertical resolution for PAN in Figure 4.8 (c) shows a similar pattern on the retrieval grid and amounts to about 0.3 km for most of the cross-section. Higher values are primarily found at the boundaries of the retrieved section and can reach up to 1 km in the core of the tropospheric PAN maximum (see Figure 4.8 (a)) at around 23 : 00 UTC. The total error is lowest in the altitude of the tropospheric PAN maximum around 12 km, which also corresponds to the region with the best vertical resolution, as shown in Figure 4.6 (c). Both CH_2Cl_2 and PAN have an overall relative error of about 30% (see also Table 4.1). As altitude decreases toward the cloud layer, the uncertainties increase significantly. Again, the contribution of the pointing error is the dominant factor influencing the total error. However, for CH_2Cl_2, additional factors such as noise and spectroscopy errors have a proportionally greater impact.

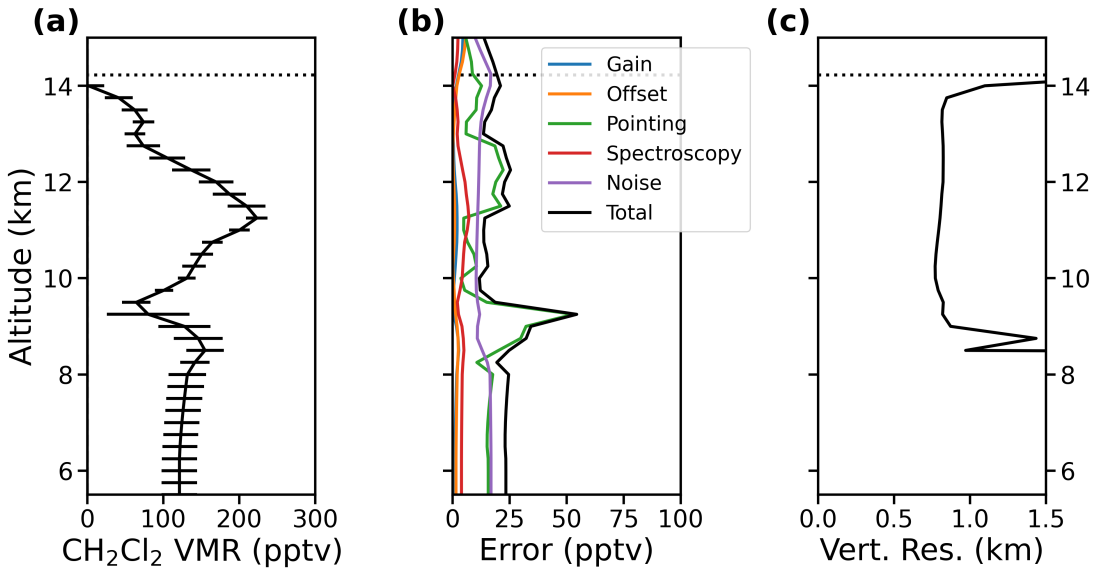

Figure 4.5: Retrieval characterization for one profile of CH_2Cl_2 from Flight 8 on 26–27 August 2023, 23:15:35 UTC. Part (a) shows the unfiltered vertical profile of the CH_2Cl_2 VMR with the total estimated error in black. In (b) contributions from different error sources and in (c) the vertical resolution are shown. As the vertical resolution below 8 km exceeds a reasonable value, VMR and the error contributions show no realistic values. Dotted lines denote flight altitude. The plots were created by Sören Johansson.

Figure 4.7 presents the corresponding errors and vertical resolution for the full cross section. At the center of the tropospheric CH_2Cl_2 maximum and along the edges of the cloud layer, the total error in Figure 4.7 (b) reaches values of approximately 60–70 pptv. At the maximum smaller data gaps due to the stricter cloud filtering applied in the CH_2Cl_2 retrieval are visible. The cloud filter likely flagged these areas because of increased aerosol levels, which is not uncommon in polluted air. As a result, the errors increase and the vertical resolution decreases, just as it does at the edges of the displayed altitude range. However, these uncertainties have a reduced impact on the relative error within the tropospheric maximum, as the VMR of CH_2Cl_2 is up to four times higher than in the surrounding regions. A similar pattern is observed in the vertical resolution in Figure 4.7 (c), with values up to two times higher in the tropospheric maximum and near the cloud edges. Additionally, the poorest resolution is observed at the upper boundary of the retrieval domain, corresponding to the flight altitude.

The vertical resolution of approximately 0.3 km for most of the retrieved PAN cross-section is evident in Figure 4.8 (c). Higher values are primarily found at the boundaries of the retrieval domain and reach up to 1 km in the core region of the tropospheric PAN maximum (Figure 4.8 (a)). The total error generally decreases with altitude (Figure 4.8 (b)), following a similar trend to CH_2Cl_2.

In Table 4.1 a summary of the statistical error values and the vertical resolution for PAN and CH_2Cl_2 can be seen. The vertical resolution for PAN is higher by a factor of two than the resolution for CH_2Cl_2. As stated before the total errors of CH_2Cl_2 and PAN result in relative errors for both species little above 30 % These uncertainties contribute to the overall measurement error but are within acceptable limits for the analysis of the structure of trace gas maxima in the context of the

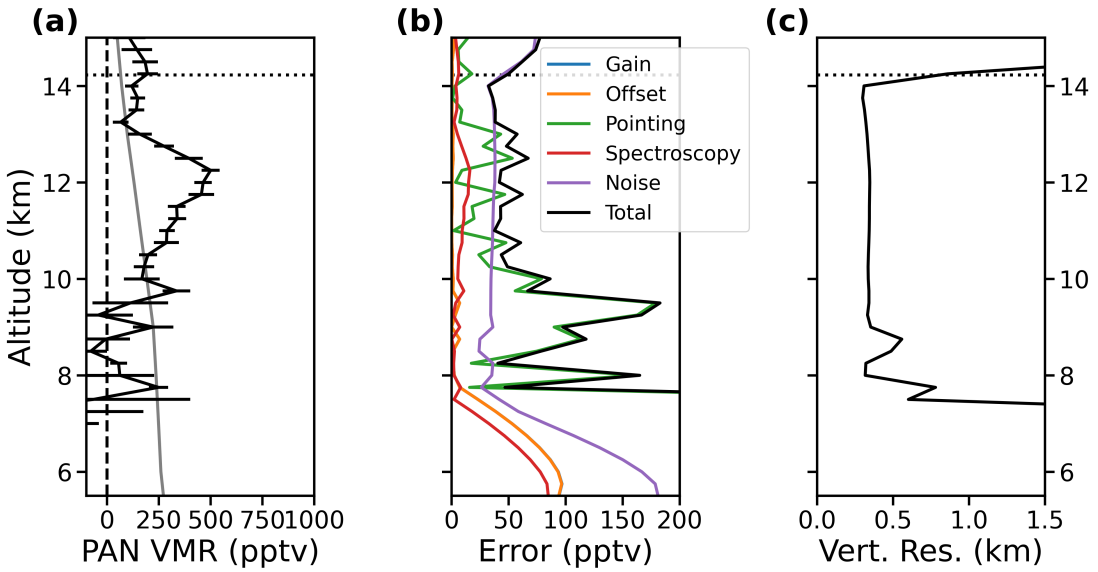

Figure 4.6: Retrieval characterization for one profile of PAN from Flight 8 on 26–27 August 2023, 23:15:35 UTC. Part (a) shows the unfiltered vertical profile of the PAN VMR with the total estimated error in black and the initial profile in gray. In (b) the different contributions from the errors depending on the altitude and in (c) the vertical resolution are shown. As the vertical resolution below 8 km exceeds a reasonable value, VMR and the error contributions show no realistic values. Dotted lines denote flight altitude. The plots were created by Sören Johansson.

EASM outflow. This is because for the later analyses, there are not absolute accuracies needed for there is no comparison with the chemical models. More important are the random errors, which influence the detection limit, and therefore, if filaments and structures are discernible from the background.

Table 4.1: Statistical summary of vertical resolution and errors for PAN and CH_2Cl_2. These correspond to the statistical values for the cross sections of the errors and the vertical resolution, as shown in Figure 4.7 (b), (c) and Figure 4.8 (b), (c), which display the total error and vertical resolution for the retrieval after the resolution filtering and averaging kernel diagnosis.

Parameter	**10th–90th Percentile**	**Median**	**Unit**
	PAN		
Vertical resolution	0.3037 – 0.4150	0.3400	km
Total absolute error	36.02 – 78.71	44.59	pptv
	CH_2Cl_2		
Vertical resolution	0.7672 – 0.9867	0.8187	km
Total absolute error	12.05 – 28.63	16.15	pptv

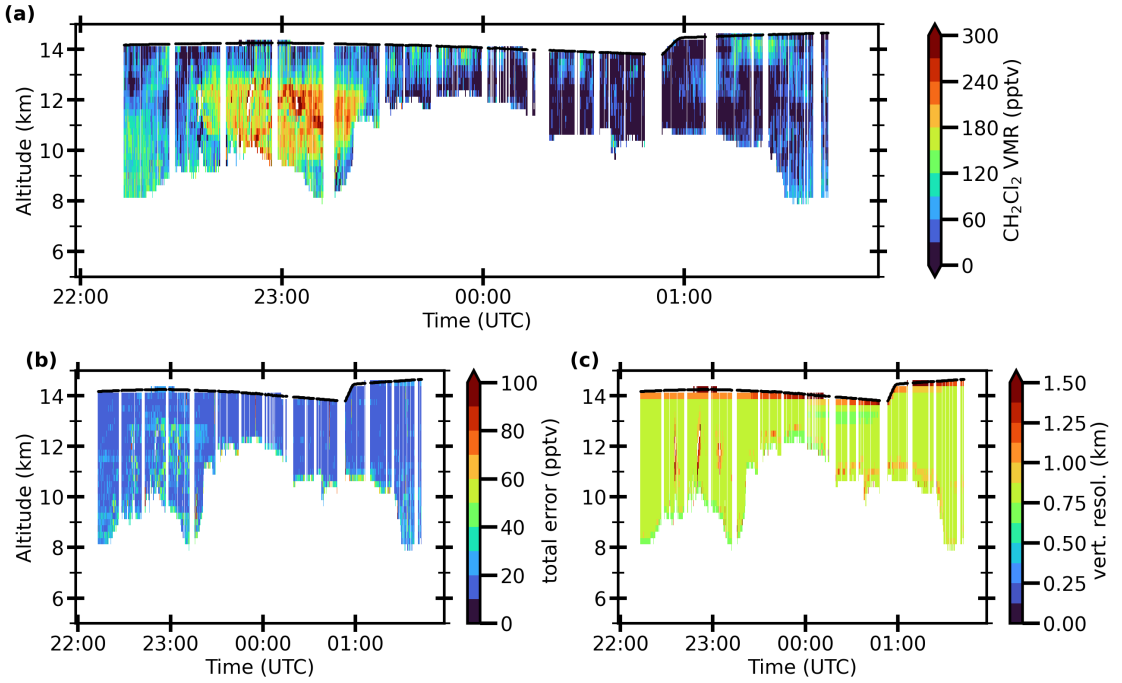

Figure 4.7: CH_2Cl_2 VMR cross section for Flight 8 on 26–27 August 2023 in panel (a) compared to the total error (b) and the vertical resolution in (c). The plots were created by Sören Johansson.

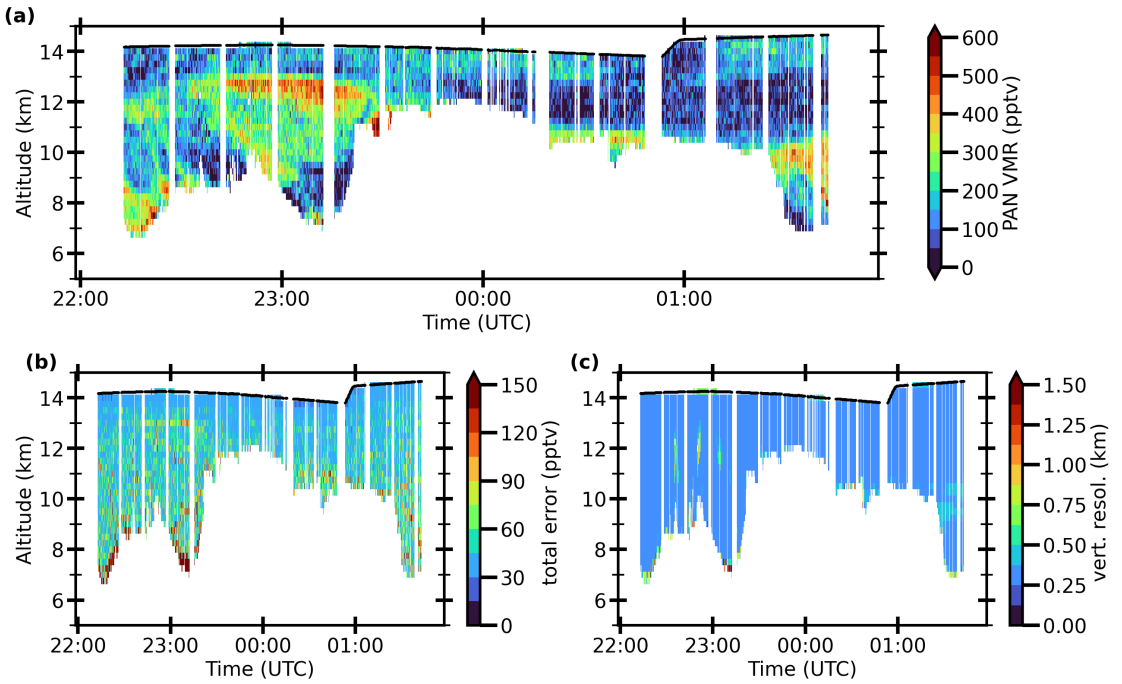

Figure 4.8: PAN VMR cross section for Flight 8 on 26–27 August 2023 in panel (a) compared to the total error (b) and the vertical resolution in (c). The plots were created by Sören Johansson.

4.2 Air Mass Transport in ICON-ART Tracer

In Section 3.3 the concept of the surface tracer of ICON-ART was explained. Now it is the aim to apply this for the investigation of the origins of the air masses measured with GLORIA. To assert the origins of trace gases and pollutants observed with GLORIA, Wetzel et al., 2021 already used artificial surface tracers from CLaMS (Chemical Lagrangian Model of the Stratosphere). In the following, the same approach is used, but with surface emission tracers calculated with the ICON-ART model, as described in Section 3.3.

4.2.1 Comparison of Cross Sections from ICON-ART Tracer and GLORIA

Figure 4.9 presents the cross-sections for Flight 8 on 26–27 August 2023 for PAN and CH_2Cl_2 in the upper two panels, analogous to Figure 4.1. Below these, six surface tracers derived from ICON-ART are displayed for the same altitude and time window. They are mapped using the same filtering criteria as the retrieved cross-sections from PHILEAS. These tracers indicate the origin of the air masses, as simulated by the ICON-ART model. In Figure 4.9 only one half of the calculated surface tracers is shown. They were selected depending on their relevance to the transport from the EASM, and the amount of their contribution to the observed air masses with GLORIA. The left out tracers can be found in the Appendix (see Section A.1)

The most prominent source region for the tropospheric maximum is identified in the combined India/China surface tracer. The structure observed in this tracer closely resembles the distribution of CH_2Cl_2 and PAN in the region of the tropospheric maximum. In the first stratospheric maximum, present between 23 : 40 UTC and 00 : 10 UTC for CH_2Cl_2 and between 23 : 40 UTC and 00 : 40 UTC for PAN, the India/China tracer exhibits fractions of up to 0.2. Among the components of this tracer, the East China surface tracer contributes most significantly to the retrieved air masses. Additionally, weaker signatures in the North India tracer align with the overall structures observed in CH_2Cl_2 and PAN, in particular at the stratospheric maxima and less for the tropospheric maximum. The South India tracer (Figure A.1) shows nearly none signal in the total cross section.

Another source contributing to the retrieved air masses, according to the ICON-ART tracers, is the Northwest Pacific. Larger structures are evident in the stratosphere, originating from tropical oceanic regions. Furthermore, the North Africa tracer exhibits a distinct structure at the location of the first stratospheric maximum in CH_2Cl_2between 23 : 20 UTC and 23 : 40 UTC, potentially indicating long-range transport in the stratosphere. A more detailed analysis of this transport will be provided in Section 4.3 on trajectory calculations.

In summary, the ICON-ART surface tracers suggest that the tropospheric maximum observed during Flight 8 on 26–27 August 2023 primarily originates from the India/China region, with East China being the dominant source. These air masses are possibly mixed along their transport path with air from the Northwest Pacific. The stratospheric signatures are also associated with the India/China tracer, though their precise source region is less distinct compared to the tropospheric

maximum. Additionally, there is evidence of long-range transport from North Africa and mixing with air masses originating from tropical oceanic regions.

Nearly all observed air masses from Flight 9 (28–29 August 2023), as shown in Figure 4.10, exhibit their strongest source region in the ICON-ART India/China surface tracer. The tracer fractions for these air masses predominantly range between 0.25 and 0.35. The most pronounced signal within this tracer originates from East China, where the structural patterns of the local maxima in CH_2Cl_2 and PAN are discernible in their broad outlines. In contrast, the North India tracer does not exhibit any distinguishable features in these trace gases, and the South India tracer shows no significant signal (Figure A.2).

Another influential surface tracer for CH_2Cl_2 and PAN during Flight 9 is the Northwest Pacific tracer. At the location of the strongest maximum in PAN, which does not have a corresponding enhancement in the cross section of CH_2Cl_2, primarily the Northwest Pacific tracer and the East China tracer show a boundary layer origin. This suggests a degree of mixing between air masses from the ASM region and those from the Northwest Pacific along the transport path across the Pacific. The influence of tropical oceanic air increases with altitude, reaching fractions of up to 0.3 at 14 km.

The signatures in the India/China surface tracer for CH_2Cl_2 maxima in Flight 16 (15–16 September 2023) are approximately twice as strong as those observed in the previous flights. The tracer fractions in the core regions of these maxima reach values up to 0.5, with the East China tracer again providing the dominant contribution, reaching fractions of up to 0.3. The air masses surrounding these maxima originate primarily from the tropical oceans, Southeast Asia and the Northwest Pacific.

For Flight 17 (16–17 September 2023), the signatures in the India/China surface tracer at the CH_2Cl_2 and PAN maxima are comparable in magnitude to those observed in Flight 16. While the spatial structures are not fully congruent, they align well with the maxima, with origin fractions reaching up to 0.55 in the upper part of the maximum. This contribution again primarily originates from East China within the combined tracer. The tropical ocean and Northwest Pacific tracers exhibit strong structural patterns around this maximum.

Additionally, the lower PAN maximum, occurring between 04 : 30 UTC and 05 : 50 UTC at altitudes between 6 km and 9 km, has weaker counterparts in the North America and Europe tracers (Figure A.4). A stronger signal is also observed in the Central Asia tracer, indicating potential contributions from this region. But for these surface tracers, a distinctive assignment to an origin region is difficult, as this implies a long-range transport around half of the globe.

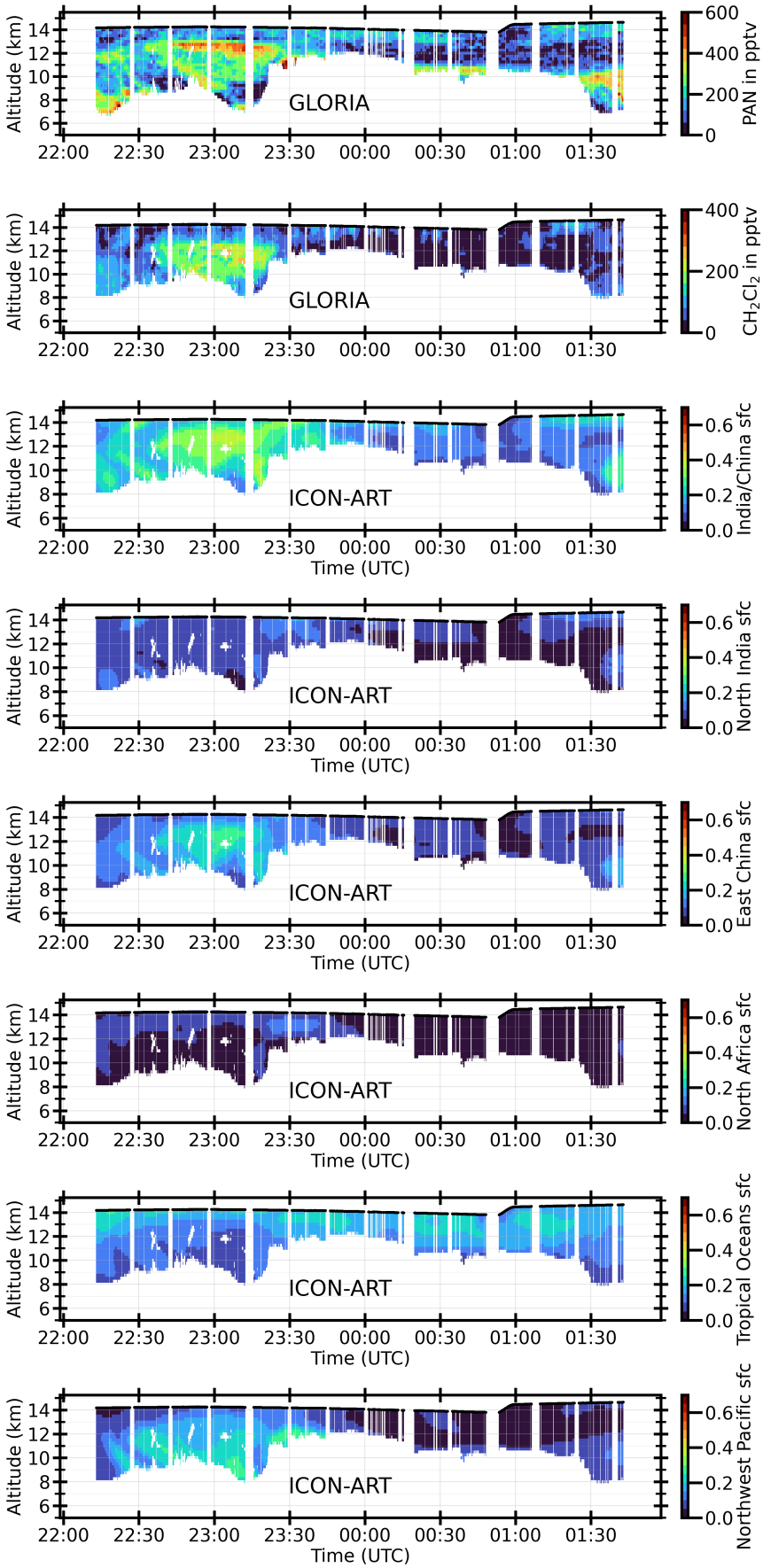

Figure 4.9: Cross Section from the GLORIA retrieval for PAN and CH_2Cl_2 from Flight 8 on 26–27 August 2023 in comparison to ICON-ART surface tracer.

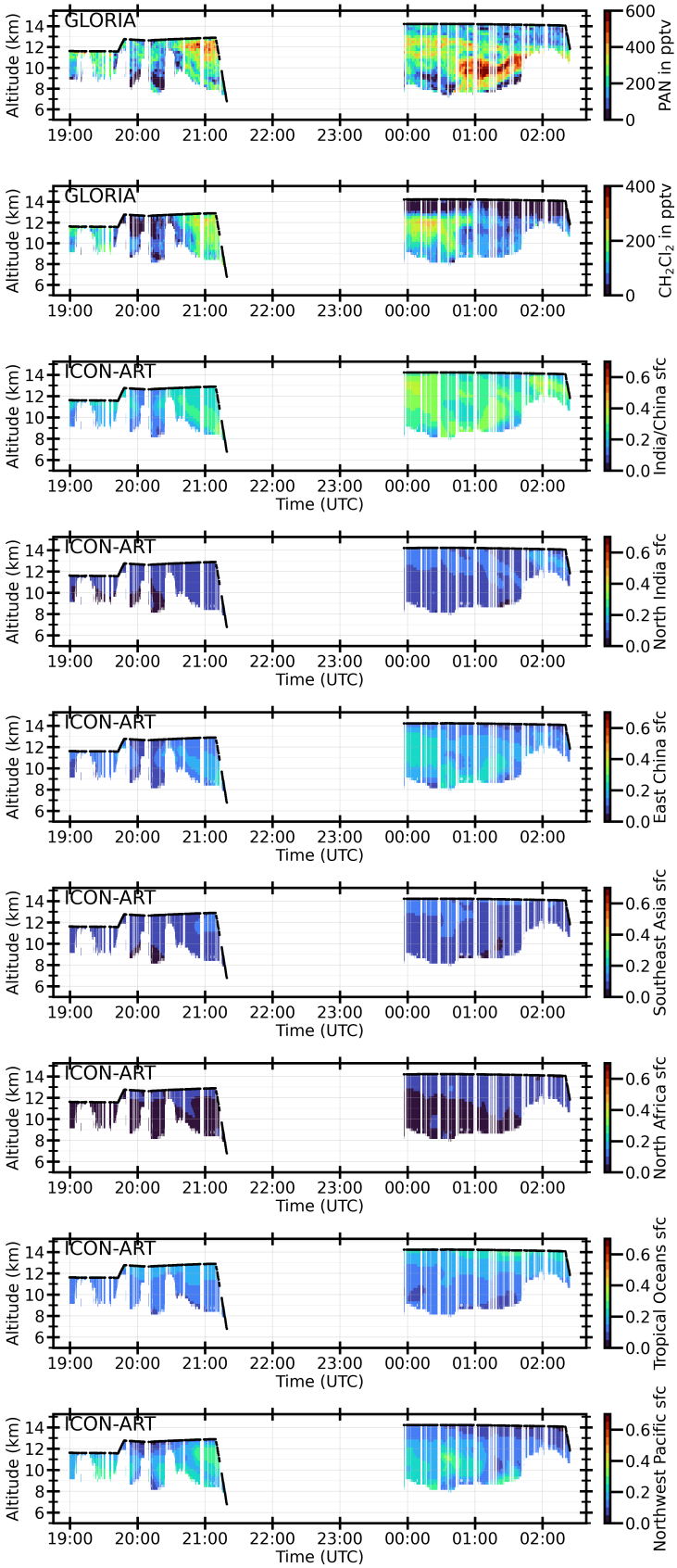

Figure 4.10: Cross Section from the GLORIA retrieval for PAN and CH_2Cl_2 from Flight 9 on 28–29 August 2023 in comparison to ICON-ART surface tracer.

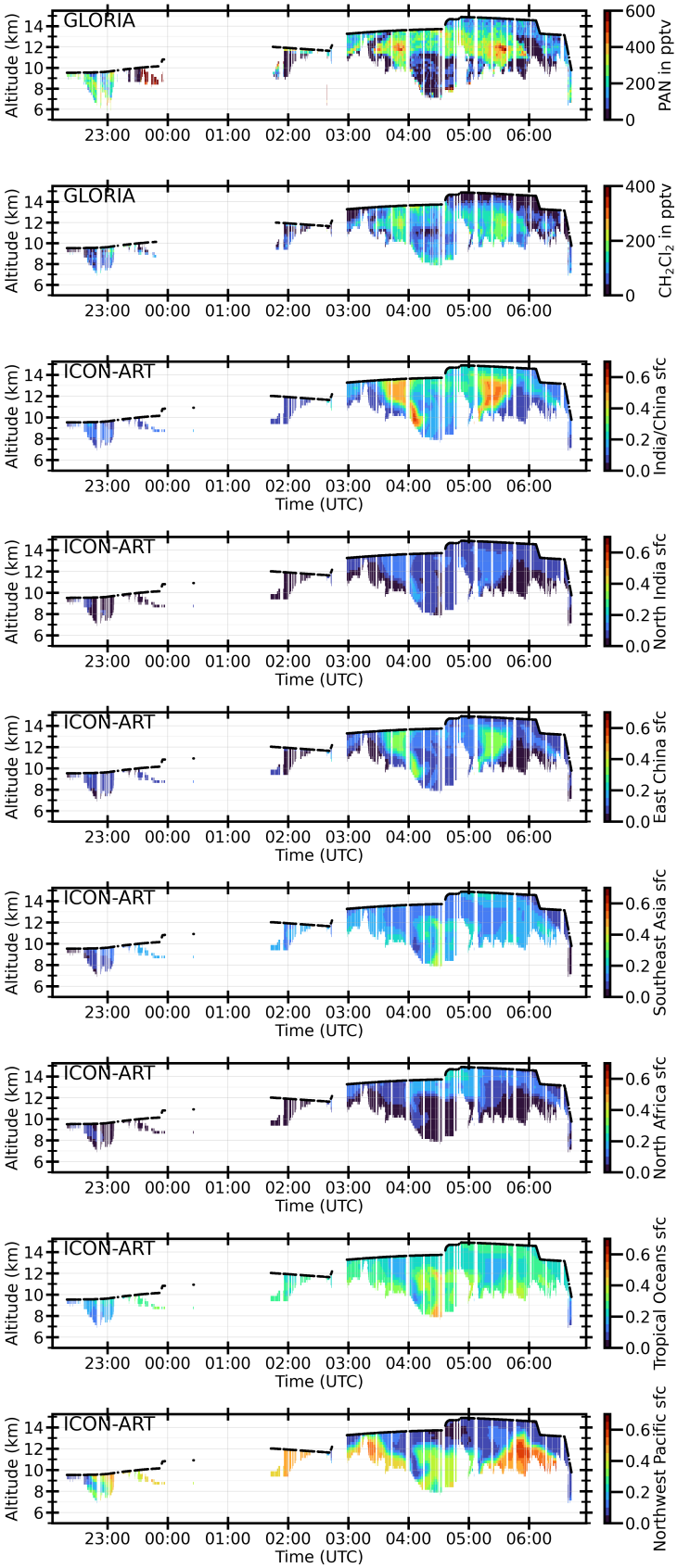

Figure 4.11: Cross Section from the GLORIA retrieval for PAN and CH_2Cl_2 from Flight 16 on 15–16 September 2023 in comparison to ICON-ART surface tracer.

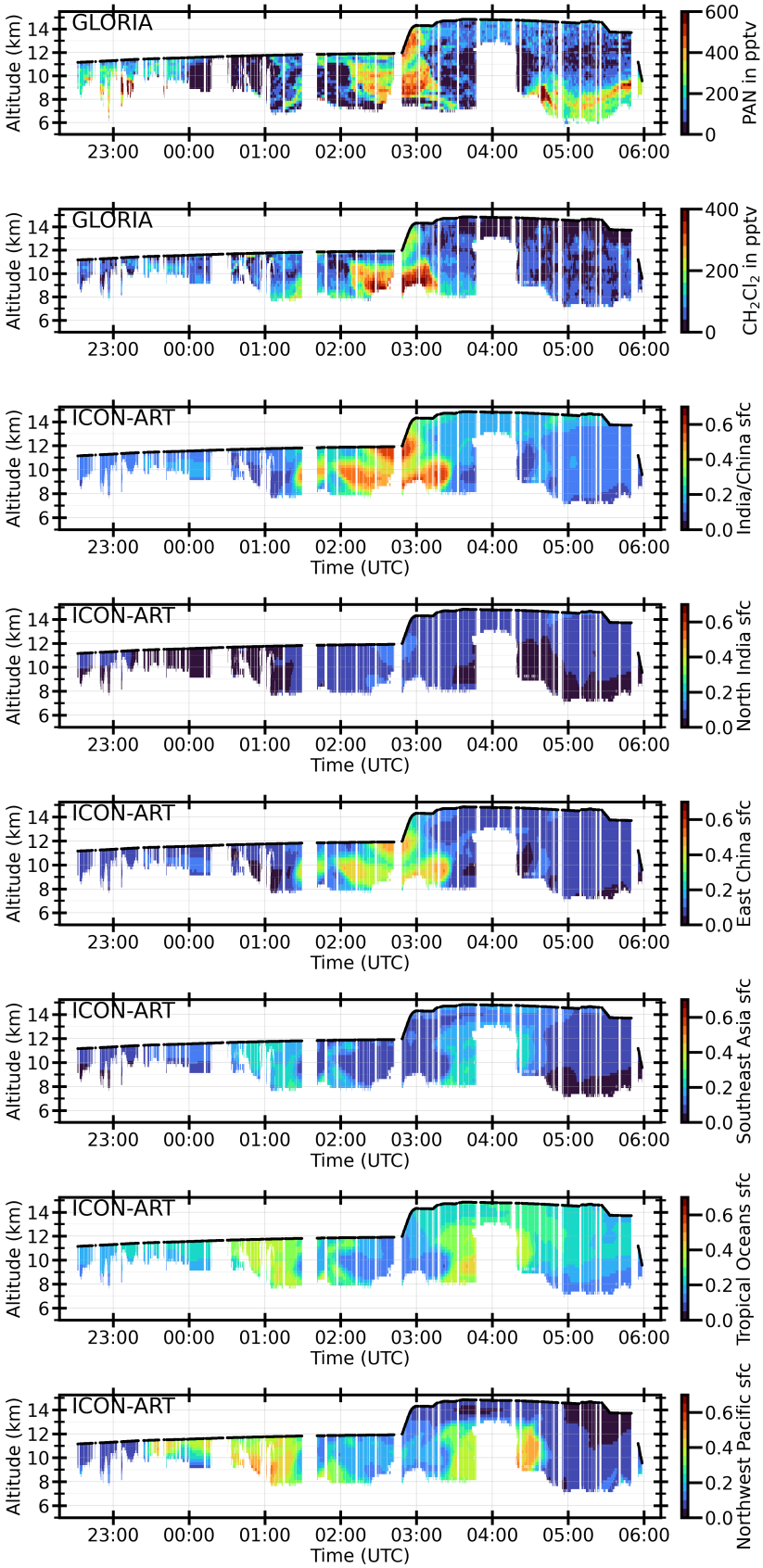

Figure 4.12: Cross Section from the GLORIA retrieval for PAN and CH_2Cl_2 from Flight 17 on 16–17 September 2023 in comparison to ICON-ART surface tracer.

4.2.2 Time- and Altitude-Resolved Transport Pathways over the Pacific in ICON-ART Surface Tracers

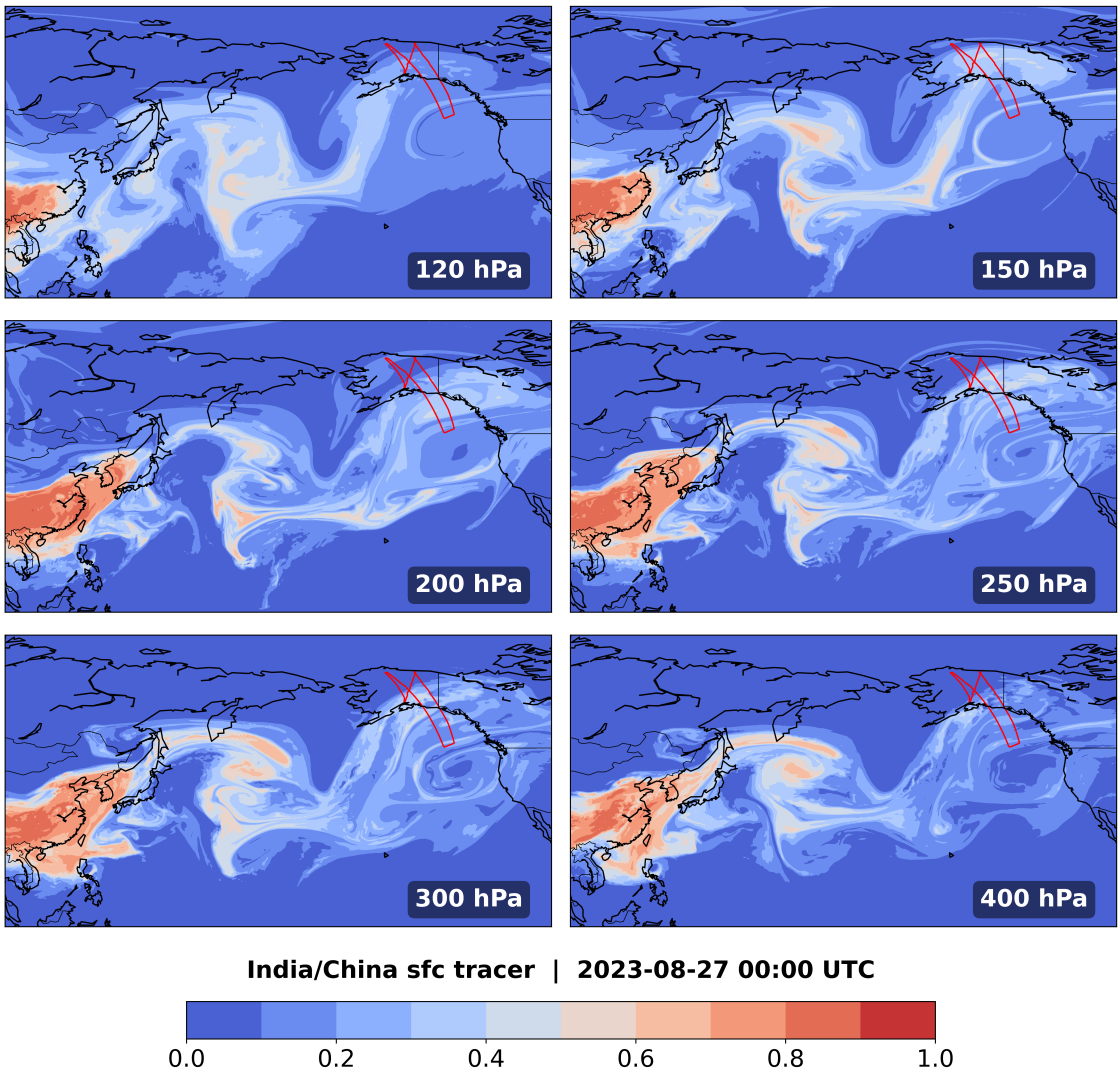

Figure 4.13: Maps of the India/China ICON-ART surface tracer distribution across the Pacific on six pressure levels from 400 hPa to 120 hPa at the half time of the flight 8 on 27th August at 00:00 UTC. The color bar represents the fraction of remaining air initiated on 1 May 2023 at the origin region. The flight path of GLORIA on HALO is shown as red line.

To better understand the vertical and temporal evolution of pollution transport from the Asian monsoon region to the UTLS, ICON-ART surface tracer fields are analyzed. These fields help identify the origin and pathway of air masses detected during Flight 8, which exhibited pronounced maxima in CH_2Cl_2 and PAN. Particular attention is paid to tracers originating from the India/China region, with a separate focus on the East China subregion due to its dominant contribution in previous cross-section analyses (see Section 4.2.1).

Figures 4.13 and 4.14 present horizontal maps of the India/China and East China surface tracers, respectively, at six pressure levels from 400 hPa to 120 hPa. These maps correspond to the temporal midpoint of Flight 8 (27 August 2023, 00:00 UTC). The tracer fields indicate the fraction of air that originated from the defined surface regions, initiated on 1 May 2023.

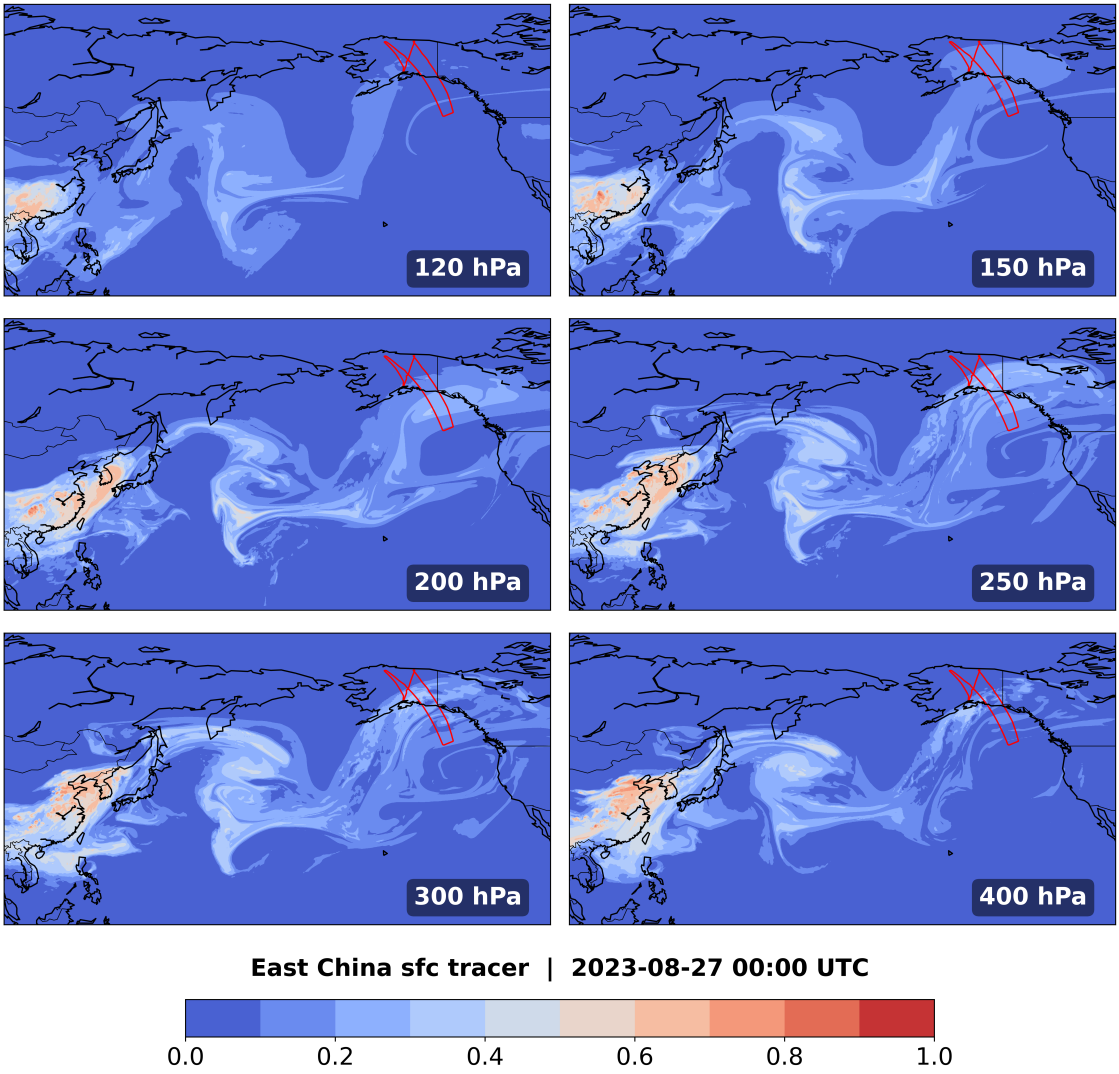

Figure 4.14: Maps of the East China ICON-ART surface tracer distribution across the Pacific using the same format as in Figure 4.13

The overall transport structure remains consistent across pressure levels, albeit with variations in tracer intensity and spatial extent. At lower altitudes (400 hPa), tracer distributions appear more filamented and localized. In contrast, mid to upper tropospheric layers (300 hPa to 200 hPa) show broader, more cohesive air masses with enhanced tracer concentrations. Notably, the 200 hPa level exhibits the highest concentrations above the Asian Summer Monsoon (ASM) region, with fractions reaching up to 0.9. This could be attributed either to vertical uplift in the ASM or horizontal convergence and accumulation of tracer-laden air masses over time.

At the Flight 8 location, predominantly over the Gulf of Alaska, tracer values of up to 0.5 are observed at 200 hPa and 250 hPa, suggesting long-range transport from Asia into the northeastern Pacific. Higher-altitude layers (150 hPa and 120 hPa) show a northward displacement of the tracer plume, now positioned over Alaska and western Canada, indicating vertical ascent followed by poleward advection.

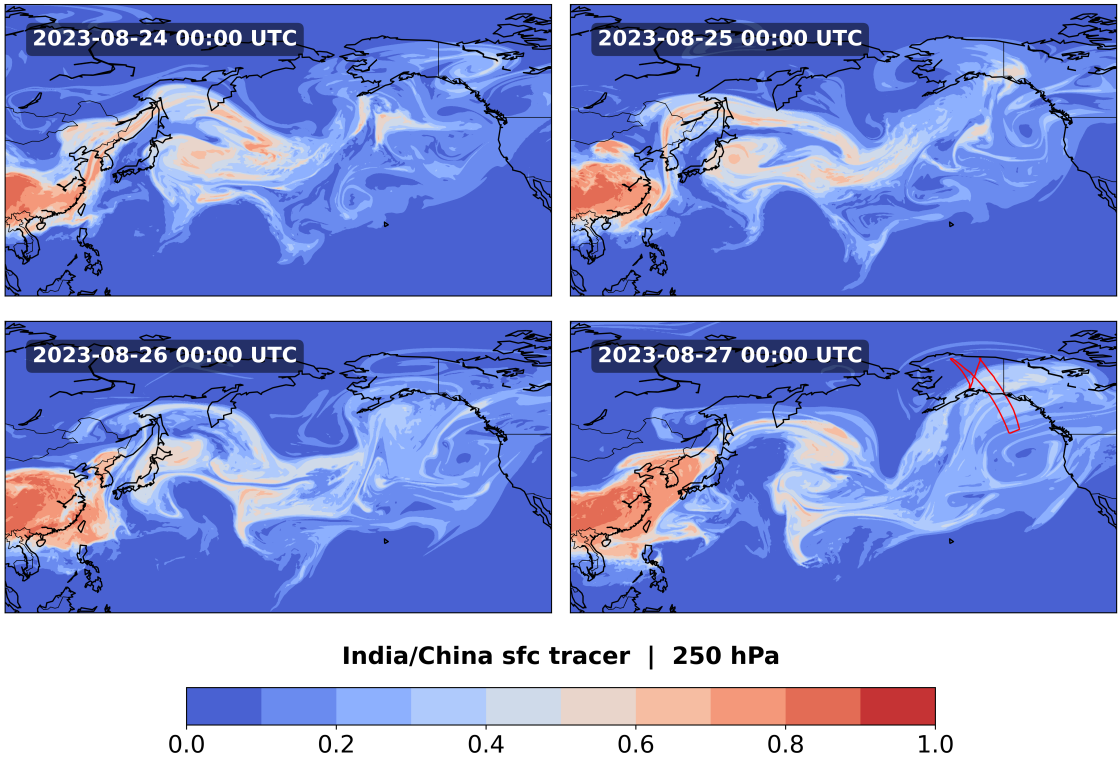

Figure 4.15: Time series of the India/China ICON-ART surface tracer distribution across the Pacific at pressure level 250 hPa for four days before measurement during Flight 8 on 27 August 2023 00:00 UTC. The color bar again represents the fraction of remaining air as in Figures 4.13 and 4.14.

The East China tracer (Figure 4.14) reflects the overall structure of the India/China tracer but with lower intensities, as expected from the smaller source region. The highest fractions up to 0.3 of East China origin near the flight track also appear at 200 hPa and 250 hPa, while minimal contributions are evident at higher altitudes (150 hPa and 120 hPa).

The 250 hPa level is chosen for further analysis for two main reasons. First, it corresponds closely the altitude of the highest concentrations of CH_2Cl_2 and PAN, making it a key layer for investigating direct transport signatures. Second, this level displays the most coherent and elevated surface tracer concentrations in both the India/China and East China tracers along the flight path. This pressure level therefore represents a critical altitude in this context for tracing long-range pollution transport from the Asian boundary layer into the UTLS.

To capture the temporal evolution of the transport processes, Figures 4.15 and 4.16 show time series of the surface tracers at the 250 hPa pressure level for the four days leading up to the Flight 8 observations.

The India/China tracer shows a well-defined transport pathway extending from the ASM region over western China and the adjacent seas, northeastward across the Sea of Japan toward the Kamchatka Peninsula. At this point the flow goes southeast and the air mass splits in the middle of the North Pacific: one branch continues east across the Pacific, while the other loops back westward, forming a large anticyclonic eddy. This eddy is most distinct on 24 and 25 August, after which its

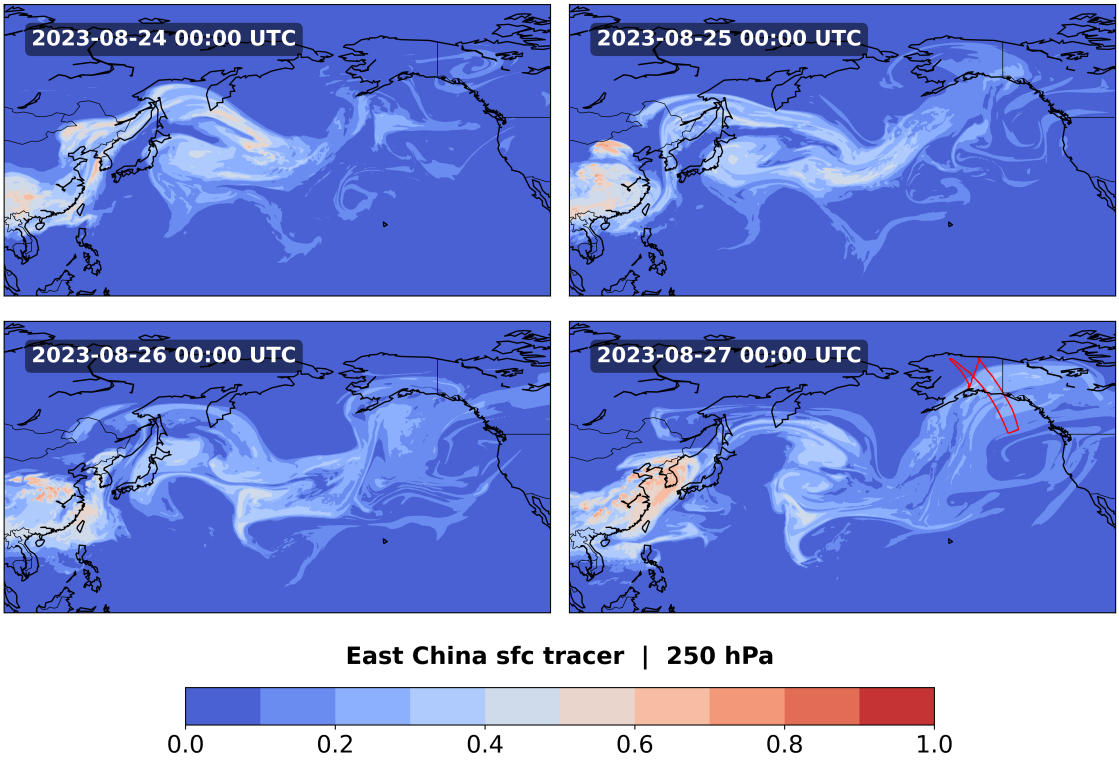

Figure 4.16: Time series of the East China ICON-ART surface tracer distribution across the Pacific at pressure level 250 hPa using the same format as in Figure 4.15.

structure becomes more diffuse. The eastward-moving air masses follow a meandering pathway that ultimately leads to the observation point over the Gulf of Alaska by 27 August.

The East China tracer displays a similar but more defined structure. Over the course of the four days, the volume of air transported from the East China source region steadily increases, peaking on 27 August. The split of the flow in the central Pacific is also visible, reinforcing the complex nature of the long-range transport from East Asia. The preceding pathway from East China past Japan to Kamchatka is consistent with the described behavior of the India/China surface tracer.

The combination of vertical and temporal analyses of ICON-ART surface tracers reveals a consistent picture of long-range transport from the Asian monsoon region into the northeastern Pacific. The India/China tracer, particularly its East China component, indicates structured pathways from the source region into the UTLS, with 250 hPa emerging as a key transport altitude. These results confirm the known origin of CH_2Cl_2 emissions in East China and characterize the transport process across the North Pacific. Nevertheless, this consideration remains incomplete without including the vertical component. In the following section, these tracer-derived insights will be extended with trajectory analyses to better quantify the source contributions and refine the understanding of the vertical transport processes into the UTLS.

4.3 Analysis of Transport over the Pacific

4.3.1 Definition of Regions of Interest (ROI) for Backward Trajectory Analysis

To investigate the origin of air masses associated with observed enhancements in CH_2Cl_2 and PAN and better understand the 3D pathways, backward trajectory calculations using HYSPLIT are applied. This is a frequently used approach for trace gases observed with GLORIA. It was usually applied for filaments of enhanced PAN or ammonia concentrations (e.g. Höpfner et al., 2019, Wetzel et al., 2021 and Johansson et al., 2020). There, other models were used, as in this case the HYSPLIT run was driven with ECMWF ERA5 meteorological data. These computations rely on the prior definition of so-called Region (or Regions) Of Interest (ROI), which serve as the starting volumes for the trajectory ensemble (analog approach to Johansson et al., 2020)

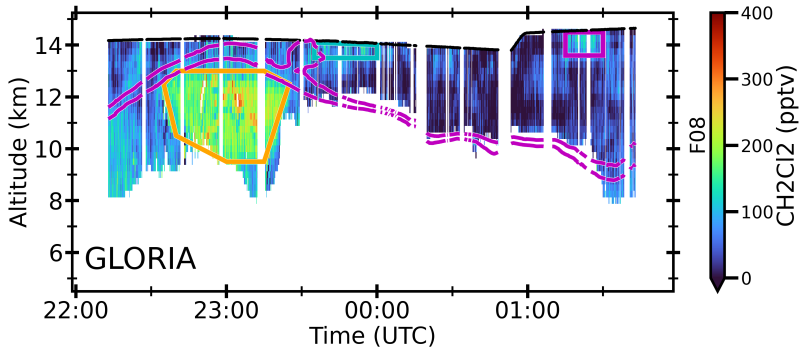

(a) CH_2Cl_2 profile with Regions Of Interest

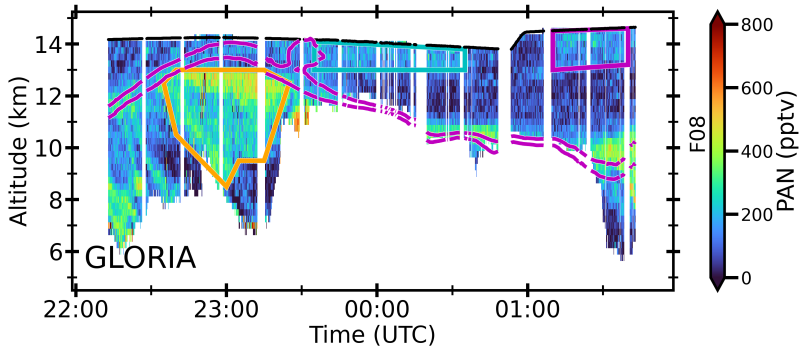

(b) PAN profile with Regions Of Interest

Figure 4.17: CH_2Cl_2 and PAN vertical cross sections from GLORIA with Regions Of Interest (ROI) marked in orange, turquoise and violet for HYSPLIT from Flight 8 on 26–27 August 2023. The dynamical tropopause is again marked with the PV = 2 PVU and PV = 4 PVU lines as in Figure 4.1

The definition of ROI is based on vertical cross sections retrieved from GLORIA measurements. Specific air mass features, such as filaments or plumes with elevated trace gas concentrations, are enclosed using polygonal paths defined in the two-dimensional domain of the cross section, namely, flight time and altitude. These time–altitude coordinates are then translated into spatial

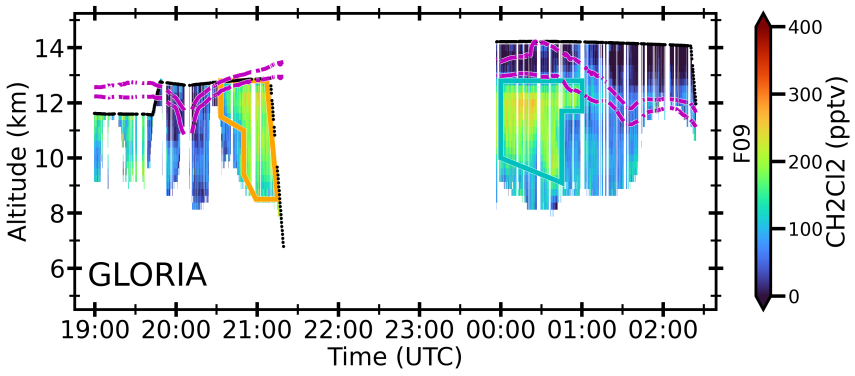

Figure 4.18: CH_2Cl_2 vertical cross sections from GLORIA with Regions Of Interest marked in orange and turquoise for HYSPLIT from Flight 9 on 28–29 August 2023 .

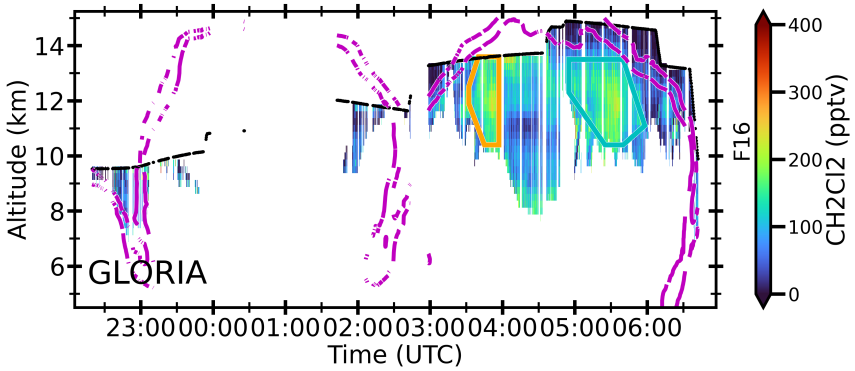

Figure 4.19: CH_2Cl_2 vertical cross sections from GLORIA with Regions Of Interest marked in orange and turquoise for HYSPLIT from Flight 16 on 15–16 September 2023 .

positions using the aircraft position data, providing the necessary inputs for initializing the backward trajectory ensembles in HYSPLIT.

This approach ensures that only coherent features with a clear spatial and temporal extent are selected for further analysis. Isolated or marginal features at the edges of the cross section, such as

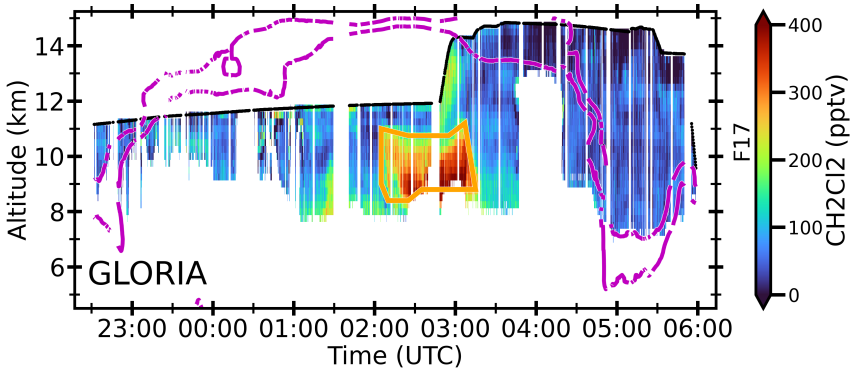

Figure 4.20: CH_2Cl_2 vertical cross sections from GLORIA with Region Of Interest marked in orange for HYSPLIT from Flight 17 on 16–17 September 2023 .

those potentially impacted by cloud filters or instrument mode changes, are excluded. This helps to ensure that the backward trajectories are initiated from representative air mass features.

Figure 4.17 displays the ROI defined for Flight 8 (26–27 August 2023), selected based on pronounced maxima in CH_2Cl_2 and PAN concentrations (see Section 4.1.1). Three distinct regions are identified, each corresponding to peaks in the trace gas profiles:

- **Tropospheric maximum (orange):** Extending from approximately 9 km to 14 km in altitude and between 22:30 UTC and 23:30 UTC. This structure aligns well for both CH_2Cl_2 and PAN, though with slight differences in intensity and extent.
- **First stratospheric maximum (turquoise):** Located between 13.5 km and 14 km, and between 23:30 UTC and 00:00 UTC for CH_2Cl_2. For PAN this maximum has a broader distribution and extends up to 00:40 UTC and down to 13 km.
- **Second stratospheric maximum (violet):** Observed from 13.5 km to 14.5 km and from 01:15 UTC to 01:35 UTC. While the maximum is more distinct in the CH_2Cl_2 cross section, corresponding enhancements in PAN are also present with again a broader spatial distribution.

PAN generally exhibits a broader distribution compared to CH_2Cl_2, often displaying additional, less coherent enhancements, for example at the edge of the dynamical tropopause. Therefore, for consistency and clearer attribution in subsequent trajectory analysis, the ROI selection focuses on CH_2Cl_2 maxima.

For the additional Flights 9, 16 and 17, ROI are also defined based on CH_2Cl_2 cross sections, shown in Figures 4.18, 4.19 and 4.20, respectively:

- **Flight 9 on 28–29 August 2023** (Figure 4.18)
  - Orange ROI: 20:30 UTC to 21:15 UTC, 8.5 km to 12.8 km
  - Turquoise ROI: 00:00 UTC to 01:00 UTC, 9 km to 12.8 km
- **Flight 16 on 15–16 September 2023** (Figure 4.19)
  - Orange ROI: 03:30 UTC to 04:00 UTC, 10.5 km to 13.5 km
  - Turquoise ROI: 04:50 UTC to 06:00 UTC, 10.5 km to 13.5 km
  - Both ROI refer to the same air parcel as the aircraft flew a loop with a 180-degree turn and sampled the same air mass on both the outbound and return flight.
- **Flight 17 on 16–17 September 2023** (Figure 4.20)
  - Orange ROI: 02:00 UTC to 03:15 UTC, 8.5 km to 11 km

This definition of ROI from GLORIA vertical cross sections of CH_2Cl_2 observations provides a basis for subsequent backward trajectory calculations. The next section will present the corresponding HYSPLIT results and their interpretation in the context of long-range trace gas transport.

4.3.2 Analysis of Long-Range Transport over the Pacific Using Backward Trajectories

Based on the initialization points from the (ROI) identified from GLORIA cross sections for CH_2Cl_2, as described before in Section 4.3.1, backward trajectories were calculated using HYSPLIT. Each ROI, defined in the coordinate system of flight time (UTC) and altitude, is transformed into three-dimensional spatial coordinates (longitude, latitude, and altitude) using the aircraft's flight path. These spatial positions, along with the corresponding time information, served as the starting points for the trajectory ensembles. The trajectories were computed using meteorological data from the ECMWF ERA5 reanalysis, with wind fields as the primary driver of the transport.

Figure 4.21 presents three ensembles of backward trajectories, corresponding to the ROI for the observed CH_2Cl_2 enhancements during Flight 8 (26–27 August 2023). The orange trajectories originate from the tropospheric maximum, while the violet and turquoise sets correspond to the two stratospheric maxima. Panel (a) shows the horizontal projection of the trajectories on a global map, while panel (b) displays their evolution in altitude over time.

The air parcels associated with the tropospheric ROI (orange) exhibit long-range transport across the North Pacific, following a meandering path. One branch originates over eastern China and the South/East China Seas, while another originates further west and north. These flows converge over the Korean Peninsula and form a coherent stream moving northeastward, turning southeast above Kamchatka, and finally bending northward over the North Pacific toward the observation region above the Gulf of Alaska. This transport route is consistent with the surface tracer pathways simulated by ICON-ART, as shown in Section 4.2.2.

In the vertical, the orange trajectories show two origins: one from varying altitudes between 6 km and 13.5 km, and another group that ascends sharply between 22 and 24 August, rising from around 5 km to 13 km within approximately two days. These air parcels reach their final observed altitude between 10 km and 13 km one to two days before the observation with GLORIA. This vertical transport is examined in more detail in Section 4.4.1.

The violet and turquoise trajectory ensembles, corresponding to the stratospheric ROI, indicate air masses that follow similar long-range transport from the Asian continent. They remain within the UTLS region, between 13 km and 15 km and do not overlap in altitude with the tropospheric ROI ensemble after 18 August. From this, it is not clear, if the observed CH_2Cl_2 maxima in the stratosphere originate from different sources or are the result of vertical uplift along the trajectory path, potentially unresolved by the ERA5 meteorological data. This aspect is further discussed in Section 4.4.

For the corresponding PAN trajectories (Appendix, Figure A.5), the overall transport pattern is similar. Due to the broader definition of the PAN ROI, these trajectory ensembles include more members and cover a slightly larger volume.

The trajectories for Flight 9, shown in Figure 4.22, indicate a transport pathway across the Pacific that closely resembles that of Flight 8. The timing of Flight 9, two days after Flight 8, was designed to capture the same air masses with a temporal offset, and the trajectory analysis confirms this intent. The vertical evolution again shows ascent between 22 and 25 August, aligning well with the vertical transport observed in Flight 8.

For Flight 16 (15-16 September 2023), the trajectory ensembles (Figure 4.23) from both orange and turquoise ROI trace the same air parcel with enhanced CH_2Cl_2 concentrations. The horizontal transport pathway shows less meandering compared to Flights 8 and 9. A part of the air parcels originates over Central Asia and follows an eastward route skirting the Tibetan Plateau. These trajectories merge with flow from Southeast Asia, then pass over the Korean Peninsula and Japan Sea, cross the Pacific south of Kamchatka, and finally reach the observation region over the Gulf of Alaska.

Vertically, the air masses remain in the UTLS between 11 km and 15 km for most of the path. Around four days prior to observation, the ensemble shows descent of roughly 2 km, merging with ascending air masses that rose between 12 and 13 September. As in Flights 8 and 9, individual trajectories exhibit rapid vertical motion, especially those from the Philippine Sea on 15 September, with ascents of up to 6 km within a few hours.

Figure 4.24 shows the trajectory ensembles for Flight 17 (16-17 September 2023), which was conducted to probe the same air mass as Flight 16. The transport pathway is nearly identical, with one notable difference: a looping structure forms between 160°E and 180°E, possibly reflecting mesoscale meteorological features in the jet stream. The vertical structure again shows rapid ascent around 12–13 September, followed by descent of approximately 2 km prior to observation, matching the vertical profile of the trajectories for Flight 16.

Flights 8 and 9, as well as Flights 16 and 17, reveal consistent and nearly congruent long-range transport pathways across the North Pacific. In all cases, trajectory origins are partly traced back to eastern China, with mixing from air masses originating further west or south. A notable feature across all flights is the rapid vertical transport occurring roughly four to five days prior to the observations. In several cases, air parcels ascend up to 7 km within two days, highlighting the potential for fast uplift mechanisms. This rapid vertical transport is investigated in more detail in Section 4.4.1.

These findings support the hypothesis of Asian pollution being transported across the Pacific into the UTLS above the Gulf of Alaska. While the general structure of this pathway is captured by ERA5-driven HYSPLIT trajectories, unresolved uplift processes and transit from the upper troposphere into the LMS likely play a key role in vertical redistribution. This will be further discussed in reference to eddy shedding processes in Section 4.4

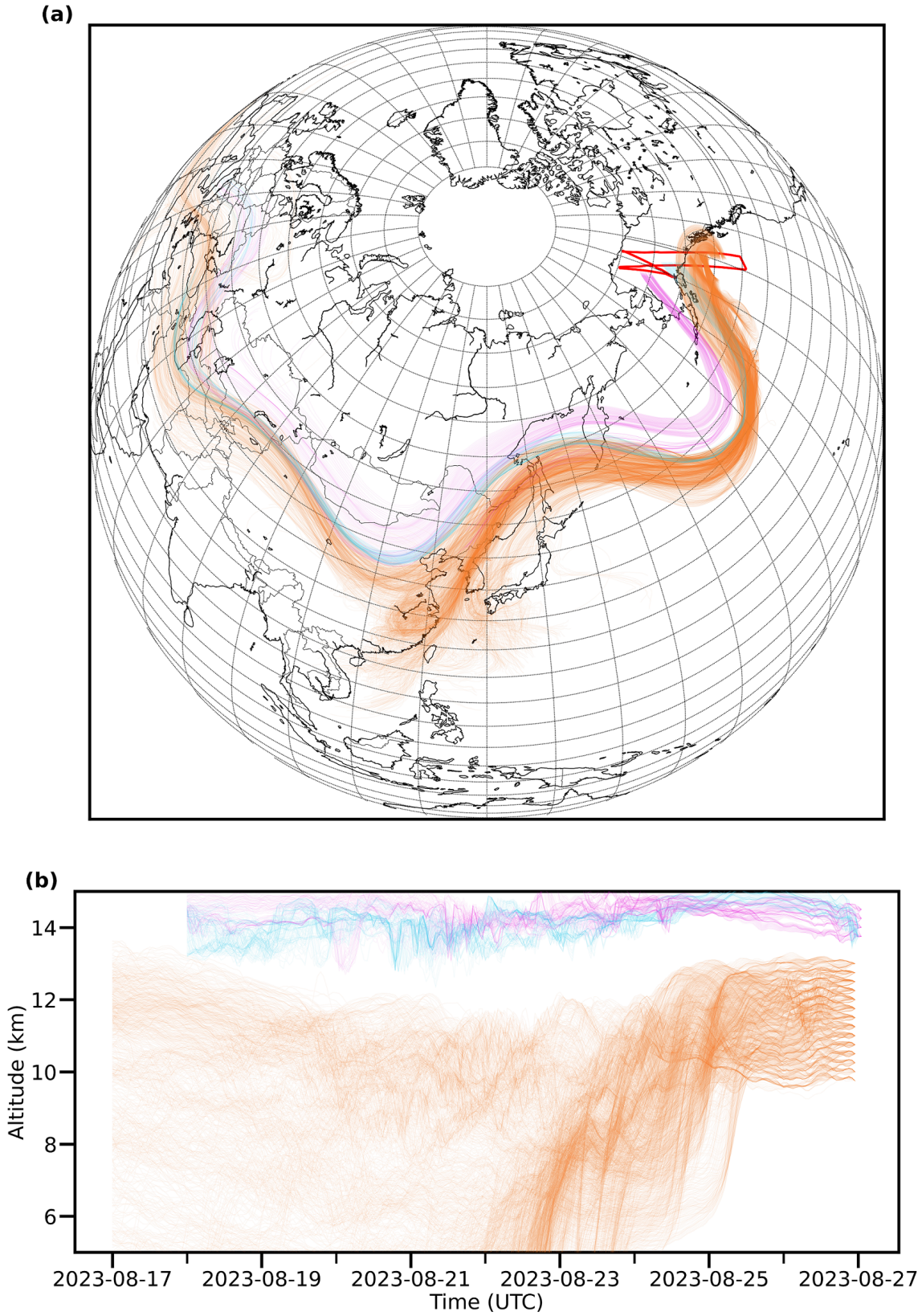

Figure 4.21: Ensembles of backward trajectories from HYSPLIT belonging to the defined ROI with respect to the CH_2Cl_2 maxima from Flight 8 on 26–27 August 2023 . The ROI can also be seen in Figure 4.17. The orange trajectories belong to the large tropospheric maximum and the ones in violet and blue belong to the stratospheric maxima. In plot a) the trajectories are mapped to the globe with the flight track in red and plot b) shows the vertical profile of the trajectories with respect to time.

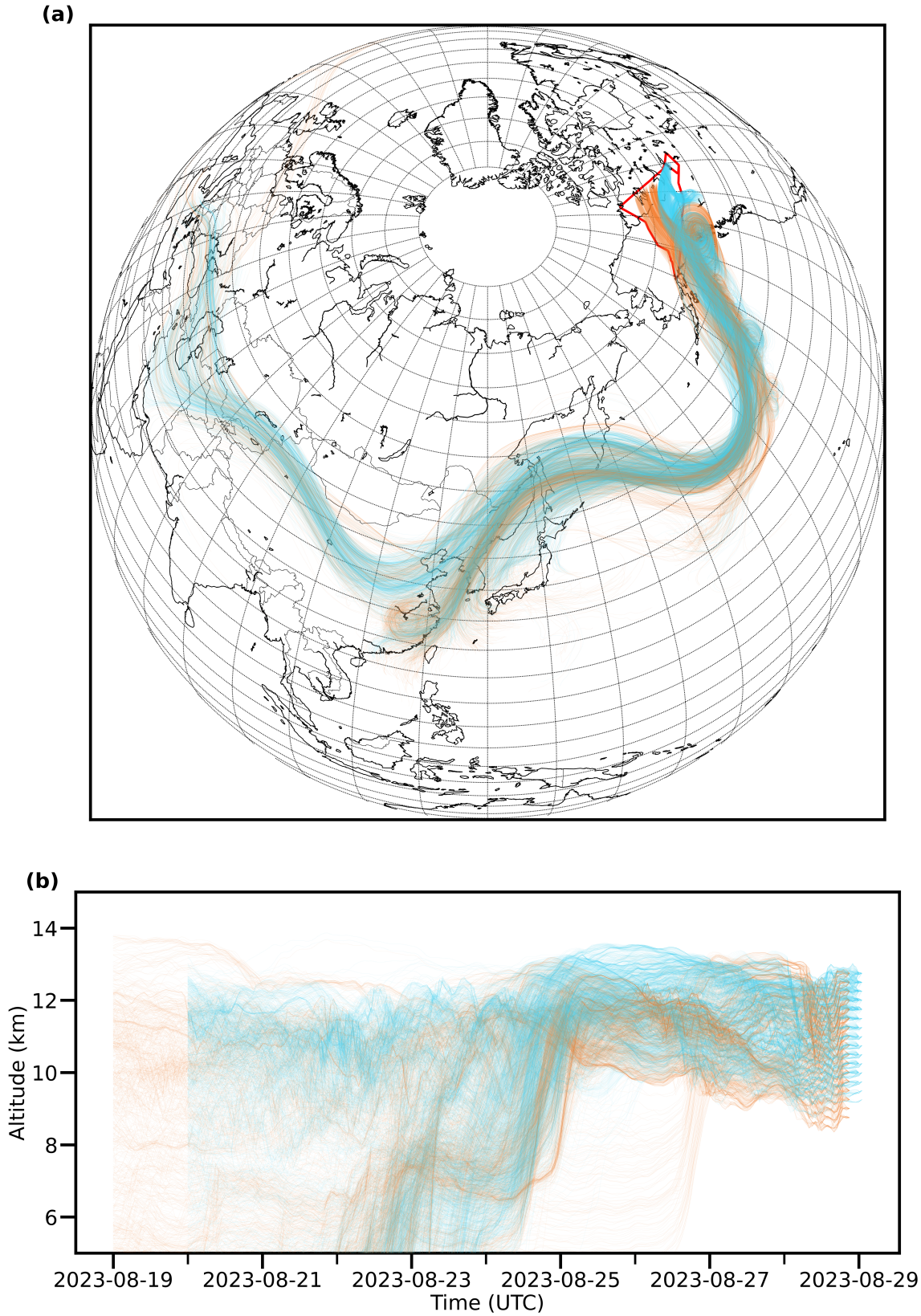

Figure 4.22: Ensembles of backward trajectories from HYSPLIT belonging to the defined ROI with respect to the CH_2Cl_2 maxima from Flight 9 on 28–29 August 2023 with the same layout as Figure 4.21. The ROI can also be seen in Figure 4.18.

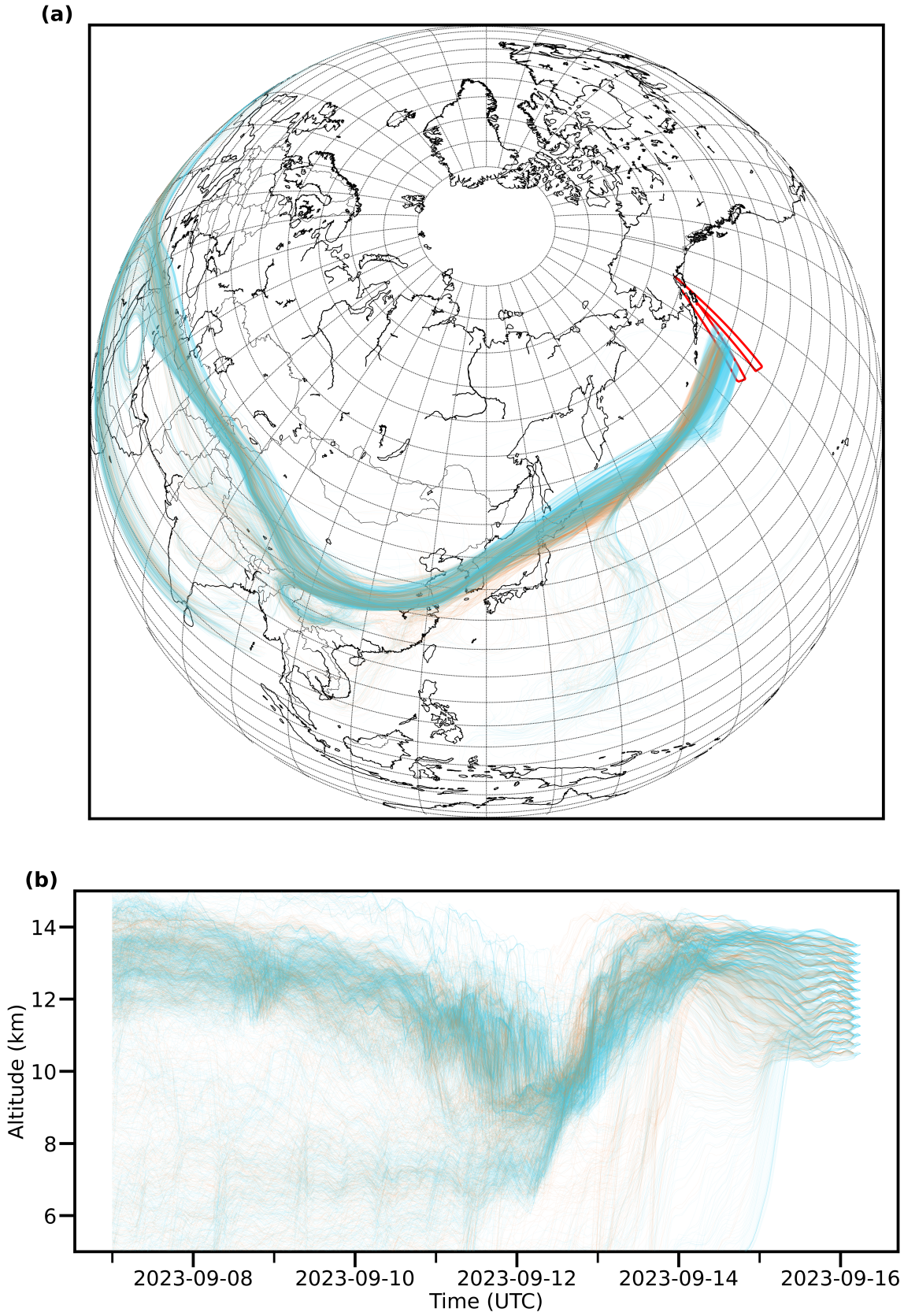

Figure 4.23: Ensembles of backward trajectories from HYSPLIT belonging to the defined ROI with respect to the CH_2Cl_2 maxima from Flight 16 on 15–16 September 2023 with the same layout as Figure 4.21. The ROI can also be seen in Figure 4.21

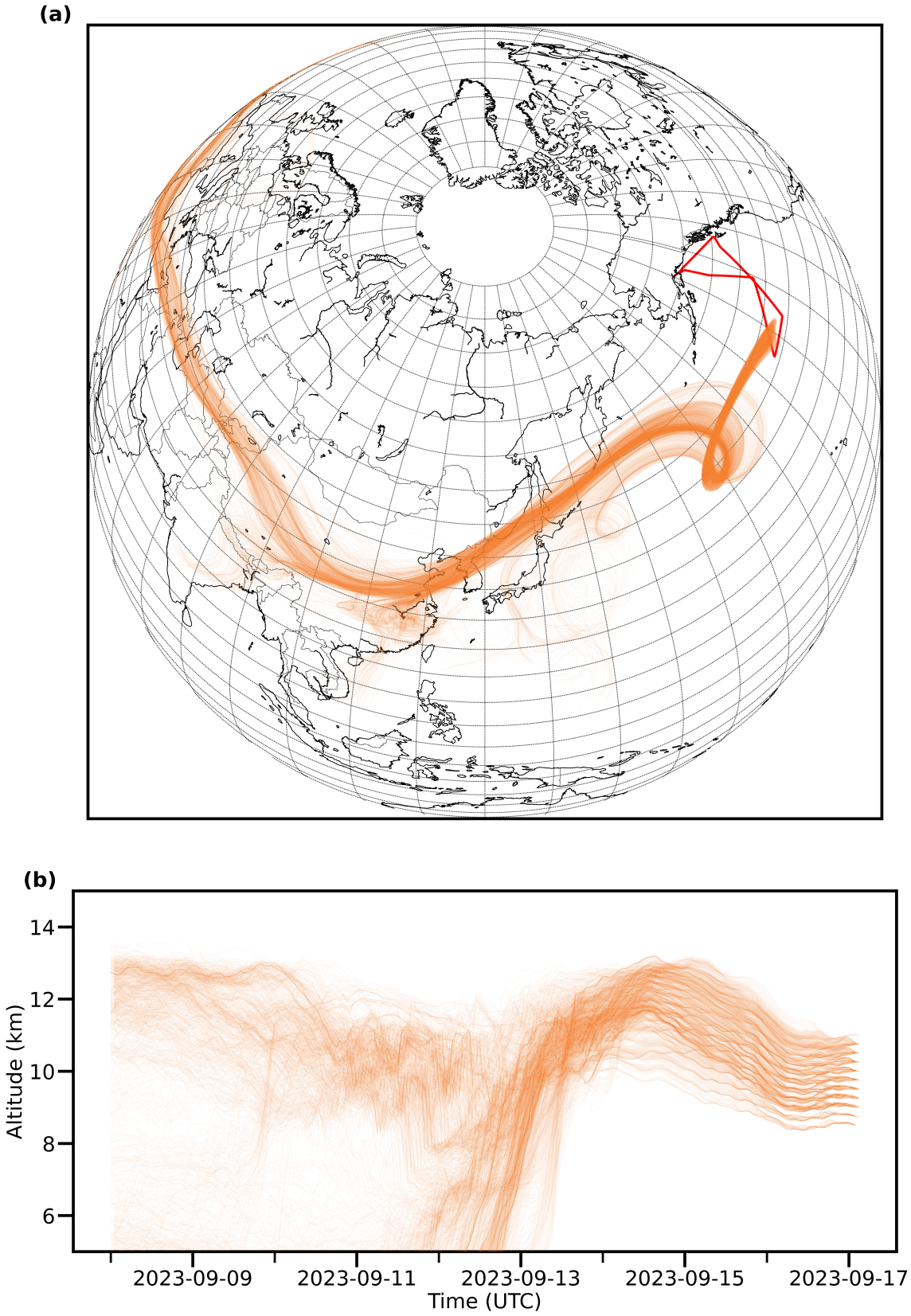

Figure 4.24: Ensembles of backward trajectories from HYSPLIT belonging to the defined ROI with respect to the CH_2Cl_2 maxima from Flight 17 on 16–17 September 2023 with the same layout as Figure 4.21. The ROI can also be seen in Figure 4.21

4.4 Discussion of the Uplift and Transport Processes

4.4.1 Vertical Ascent in the Northwest Pacific along the Transport Pathway

As discussed in Section 4.3, all four analyzed flights, exhibiting significant enhancements of CH_2Cl_2 and PAN volume mixing ratios (VMR), show indications of rapid vertical uplift. This ascent of up to 7 km within two days occurs approximately four to five days prior to the in-situ measurements. To better understand the timescale and mechanisms behind this uplift, Flight 8 on 26–27 August 2023 is used here as a representative case study.

To isolate uplift processes specifically over the ASM region, the ensemble of backward trajectories was filtered to include only those trajectories with origins east of 70° longitude. With this filtering only the trajectories associated with the tropospheric maximum are included, all trajectories calculated back from the stratospheric maxima have their staring point further to the west (see Section 4.3.2). Figure 4.25 presents these filtered trajectories, which predominantly originate over eastern China. In Figure 4.25a, the trajectories are colored by altitude, while Figure 4.25b shows the time progression. Between August 21 and 23, trajectories span a broad altitude range from below 2 km up to 10 km over the Japan Sea and Kamchatka. From there, they ascend further over the North Pacific to reach approximately 13 km at the observation point. While overlapping trajectories limit detailed interpretation, the general uplift pattern is clearly visible.

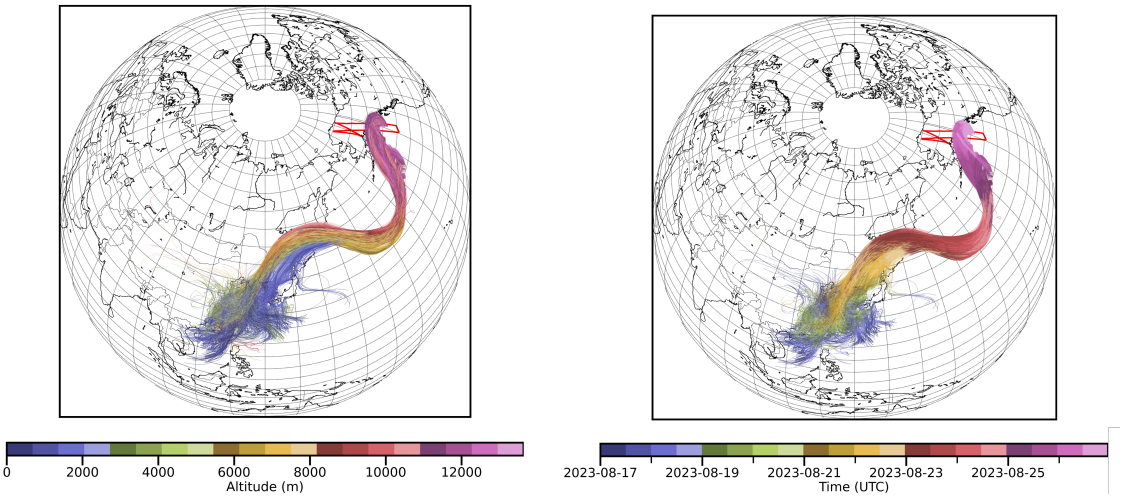

(a) Trajectories mapped to altitude in m

(b) Trajectories mapped to time steps in UTC

Figure 4.25: Source region filtered backward trajectories with color mapped altitude and timestep values. Only trajectories with a source location of more than 70° E are considered.

To further investigate rapid vertical transport, Figure 4.26 highlights trajectories exhibiting ascent rates exceeding 600 hPa in 48 hours from the lower troposphere (see discussion below and Madonna et al., 2014, Joos et al., 2023 and Heitmann et al., 2024). The ascent rate is calculated as follows:

$$\frac{\Delta p}{\Delta t} = \frac{p(t_0) - p(t_0 - \Delta t)}{\Delta t} \quad < \quad \frac{-600\,\mathrm{hPa}}{48\,\mathrm{h}}$$

A substantial fraction of trajectories meets this criterion between August 23 and 26, indicating rapid ascent outside the ASM core, predominantly over the northwestern Pacific. This observation suggests that the strongest uplift occurs over the western Pacific, rather than directly over East China or the Tibetan Plateau. As similar dislocation was also observed by Vogel et al., 2014, who described a rapid uplift inside typhoons and a following injection into the anticyclone over the monsoon region with westward eddy shedding.

Such rapid vertical transport is also characteristic of Warm Conveyor Belts (WCBs), which are typically defined by pressure decrease exceeding 600 hPa over 48 hours (Madonna et al., 2014, Heitmann et al., 2024) with the exception of uplifts in a tropical cyclone, but are tied to the flank of an extratropical cyclone (Joos et al., 2023). Aerosol and pollution transport via a WCB into the UTLS and crossing of the tropopause over Europe has recently described by Joppe et al., 2025. The climatological WCB frequency for June to August peaks over eastern Asia and the northwestern Pacific, with a distinct maximum over the Japan Sea (Joos et al., 2023). This aligns well with the location and timing of the strong ascent identified in Flight 8. According to Joos et al., 2023, WCB activity near the Himalayas is closely associated with the ASM, while WCBs over the North Pacific are primarily linked to the mei-yu/baiu front. These WCBs can penetrate the upper troposphere and potentially the lower stratosphere. Heitmann et al., 2024 similarly identifies WCB inflow, ascent, and outflow profiles that correspond spatially and vertically with the height profiles observed in the backward trajectories of Flight 8 on 26–27 August 2023 .

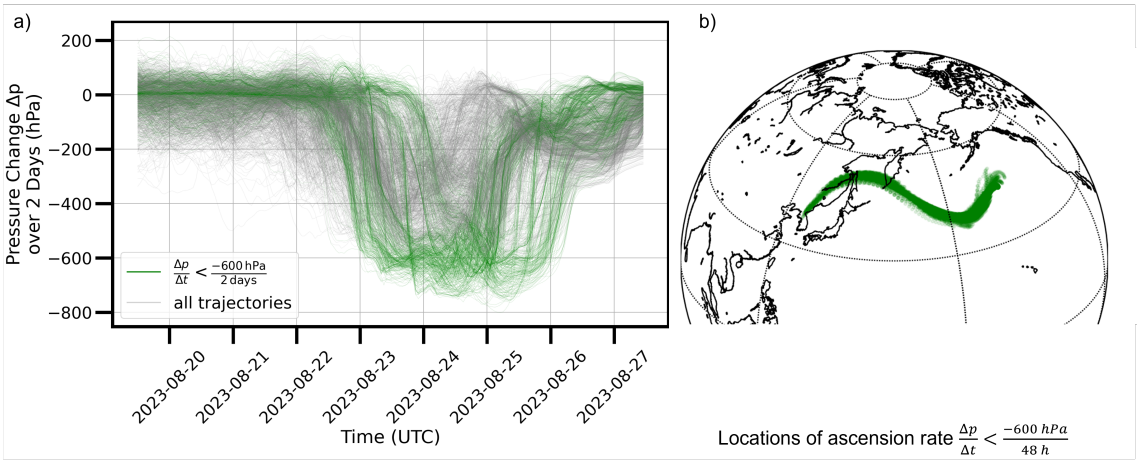

Figure 4.26: Ascent rates for Flight 8 on 26–27 August 2023 . In a) the temporal progression of the ascent rate is shown. All trajectories which reach at least once an ascent rate $\frac{\Delta p}{\Delta t}$ less than $\frac{-600\,\mathrm{hPa}}{48\,\mathrm{h}}$ are plotted in green and the location of these ascent rates can be seen in b).

Additionally, WCBs are accompanied by enhanced precipitation, as the uplifted warm and moist air from monsoonal and maritime regions condenses at higher altitudes (e.g. Madonna et al., 2014, Joos et al., 2023). Figure 4.27 shows total precipitation from ERA5 reanalysis data accumulated over 24 h over East Asia and Northwest Pacific in the six days before the measurement on August 27. Maximum daily precipitation exceeding 0.018 m is observed over the Yellow Sea and the west coast of the Japan Sea on August 22, increasing to more than 0.026 m on August 23 localized over Primorje in Southeast Russia (135° E, 47° N). This precipitation may be associated with the backward flank of an extratropical cyclone, supporting the WCB hypothesis (Madonna et al., 2014).

The here used criterion of an ascend of more than 600 hPa in 48 h, is more simplified than the selection and WCB identification process of Madonna et al., 2014 and Joos et al., 2023. It is a necessary condition, but not a sufficient one, as these studies apply more refined filtering of trajectories regarding the detailed ascension and the positioning with respect to (extra-)tropical cyclones. Even though precipitation in the vicinity of the ascend can be observed and the climatological frequencies of WCBs in the summer have a (local) maximum over the discussed regions of the Northwest Pacific, there not enough evidence in the analysis in this thesis to clearly attribute the tropospheric air mass ascent of Flight 8 to a WCB event. Additional analysis of the extratropical cyclones and the PV could provide more clarity about the ascent as depicted by the trajectories.

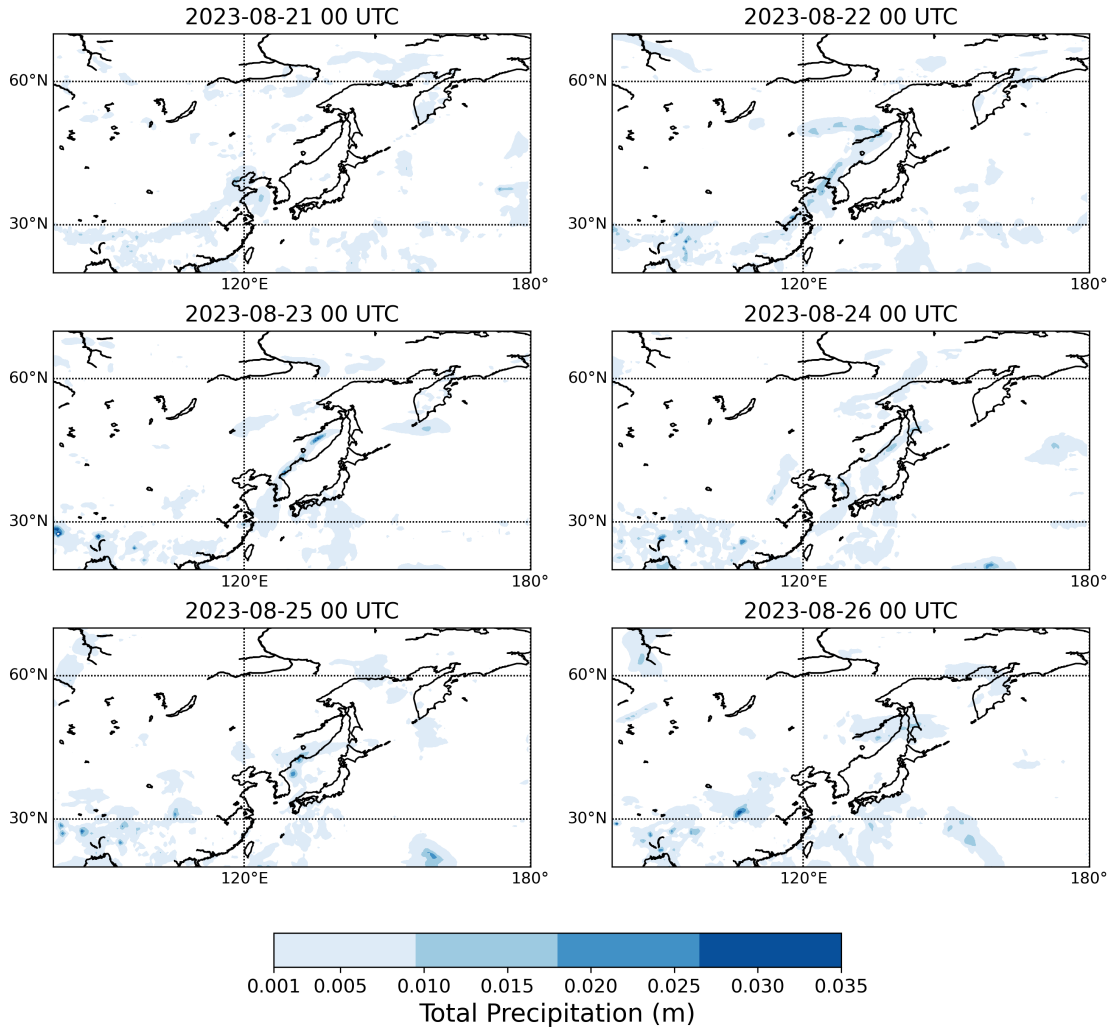

Figure 4.27: Total Precipitation accumulated over 24 h from ERA5 reanalysis data. The panels show the time evolution of the precipitation over the West Pacific for six days before Flight 8 on 26–27 August 2023

The observed transport pathway also suggests interactions with the West Pacific Anticyclone (WPA), a secondary anticyclonic mode of the ASM. X. Wang et al., 2022 define WPA events as anticyclonic centers between 135°E and 140°E during July and August. Supporting, Honomichl and Pan, 2020 link the formation of the WPA to eastward eddy shedding from the main ASM anticyclone. Eddy

shedding plays a significant role in horizontal trace gas transport. Deep convection or a typhoon within the ASM can lift boundary layer air into the upper troposphere, where it spirals upward and is ejected via eastward eddy shedding (Vogel et al., 2014, von Hobe et al., 2021, Pan et al., 2024). This process can lead to the injection of trace gases like CH_2Cl_2 into the UTLS, as suggested by Lauther et al., 2022. According to Vogel et al., 2019, this spiral ascent within the anticyclone and the eastward outflow provide an efficient isentropic pathway into the lower stratosphere.

Figure 4.28 illustrates the development of two distinct anticyclonic maxima in geopotential height between August 23 and 26, one prominent centered from Iran to the eastern Himalayas, and another transient maximum over the Japan Sea. This bimodal structure is a strong indication of WPA development, which supports the interpretation of eastward eddy shedding as a resulting mechanism (Honomichl and Pan, 2020).

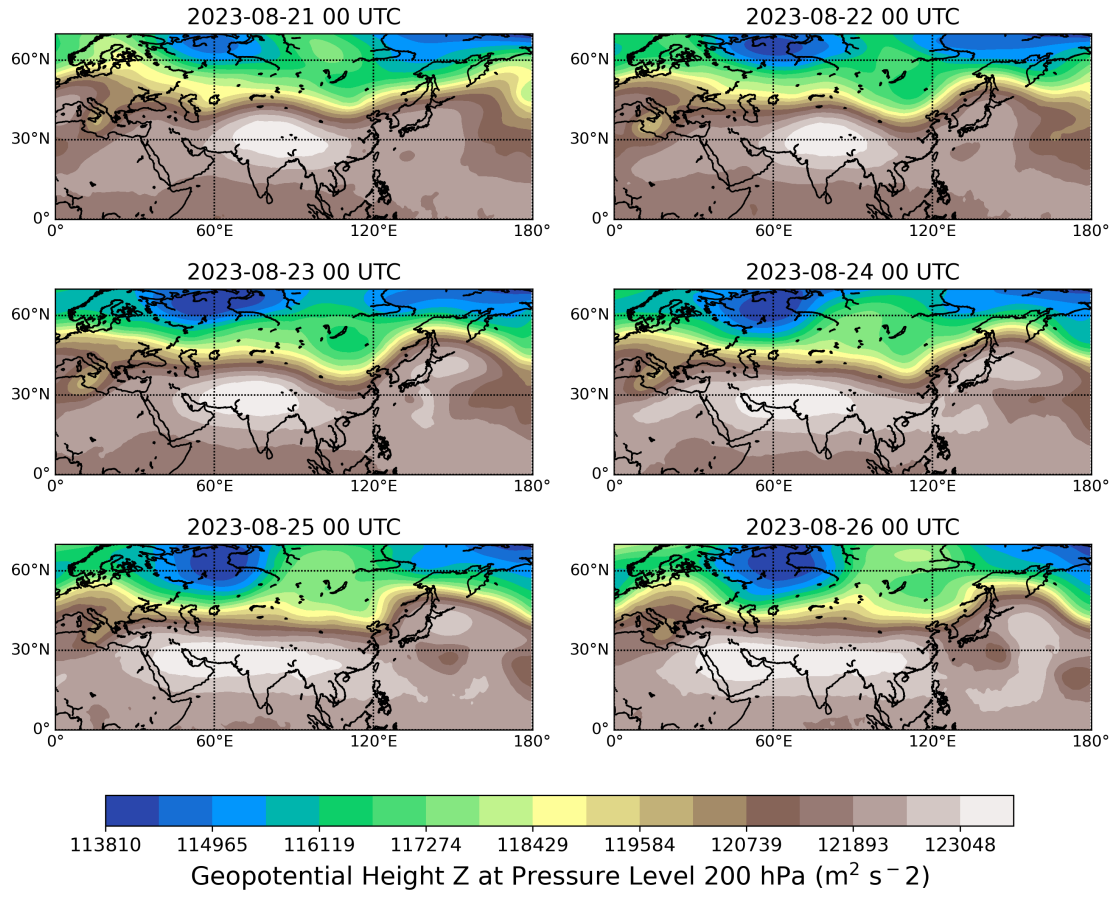

Figure 4.28: Geopotential Height at 200 hPa from ERA5 reanalysis data. The panels show the time evolution of the anticyclonic modes over the ASM region and West Pacific for six days before Flight 8 on 26–27 August 2023 .

Lauther et al., 2022 associate CH_2Cl_2-rich air with upward transport through convection and spiral ascent in the AMA, followed by eastward transport. However, this analysis shows that much of the uplift occurs outside the core monsoon region. Once air masses reach the upper troposphere, they

may mix and be entrained into eddy structures that are transported eastward via the subtropical jet (Pan et al., 2024, Vogel et al., 2019, Plumb, 1996).

While the observed tracer structure and trajectory analysis show similarities with the eddy shedding case study described by Vogel et al., 2014, the location of the uplift, predominantly over the western Pacific, may suggest a spatial shift in the monsoon circulation at lower altitudes. The spiral uplift is not observed around the AMA core, as e.g. trajectories from CLaMS simulations in Vogel et al., 2014 show. But Vogel et al., 2015 describe emissions originating from Southeast Asia within the core and transport along the periphery of the AMA. Deep convection or tropical typhoons are then the cause of the rapid uplift, followed by mixing into the monsoon's anticyclonic circulation. This is even described in the case of two modes of the anticyclone. The uplift east of the anticyclone is also consistent with global MIPAS observations of PAN from Fadnavis et al., 2014. They state that, while PAN emissions from India are largely injected directly into the AMA, Chinese emissions tends to reach the UTLS east of the anticyclone.

The uplift of the observed high concentrations of CH_2Cl_2 shows some characteristics of WCB uplift and eddy shedding processes with the formation of a WPA. Both processes possess the ability to transport pollution into the UTLS, which was likely observed for CH_2Cl_2 and PAN during Flight 8 on 26–27 August 2023 . Polluted air from the tropopause uplifted by WCB can also be mixed with air from an UTLS background along the transport pathway (Joppe et al., 2025). However, the evidence for WCB-driven uplift for the tropospheric maximum of CH_2Cl_2 remains incomplete for the discussed case of Flight 8. It is not sufficient to conclusively attribute the observed ascent to WCB activity. A possible explanation for the stratospheric maxima involves uplift under the influence of the monsoon system itself, followed by eddy shedding over the Pacific, potentially associated with Rossby wave breaking. This interpretation aligns with the horizontal distribution patterns seen in the ICON-ART surface tracers and is supported by preliminary findings from the PHILEAS campaign (Riese, 2025, in preparation). The uplift process itself is not resolved for the stratospheric maxima in the HYSPLIT trajectories. As the ICON-ART surface tracers indicate an origin in the monsoon region, it can be assumed, that the uplift linked to the ASM had taken place along the path of the trajectories.

Further analysis of the involved transport processes should use Potential Vorticity (PV) to analyze the anticyclones (Pan et al., 2024) and the described low PV values at the top of WCB (Joos et al., 2023, Madonna et al., 2014, and Heitmann et al., 2024). To the best of current knowledge, these two (rapid) uplift processes, WCB activity and ascend into the AMA with subsequent eddy shedding, have not yet been jointly discussed in the context of the ASM. For this thesis, an open question remains whether uplift outside the deep convective regions can be initiated by WCBs and subsequently mixed into an eddy shedding process. This process could already contains air masses that ascended further west into the anticyclone via, for example, deep convection over the Tibetan Plateau and subsequent upward spiraling.

4.4.2 Trace Gases in the Stratosphere

Airborne measurements conducted during the WISE campaign in autumn 2017 over Western Europe and the midlatitude Atlantic Ocean revealed up to 150% enhanced CH_2Cl_2 mixing ratios in the extratropical lower stratosphere (Ex-LS) compared to background levels. Lauther et al., 2022 attributed these anomalies to emissions from southern and eastern Asia, transported over a period of 6–11 weeks through the summertime Asian Monsoon Anticyclone (AMA).

Observations from the GLORIA instrument during Flight 8 on 26–27 August 2023 detected filaments of enhanced CH_2Cl_2 and PAN within the UTLS region as described in Section 4.1.1. The interpretation of these structures is complex due to the nature of the cross-sectional measurements and the geometry of the tangent points. For instance, the projection of these tangent points on the ground is spatially displaced, which affects the comparison with dynamical tropopause indicators derived from ERA5 reanalysis (PV = 2 PVU and PV = 4 PVU). This displacement is more pronounced for the feature between 01 : 15–01 : 30 UTC than for the earlier maximum between 23 : 40–00 : 10 UTC, which lies closer to the PV = 4 contour. Even so, the definition of the dynamical tropopause on the PV = 2 PVU isoline is a simplification and does not generally hold, since no single PV-isosurface provides a fully accurate representation of the tropopause (Turhal et al., 2024).

Jesswein et al., 2025 report CH_2Cl_2 mixing ratios of up to 300 pptv from in-situ measurements at flight altitude during Flight 8 on 26–27 August 2023 . These high concentrations may correspond to the GLORIA observations between 23 : 40 and 00 : 10 UTC, as the flight altitude intersects seemingly this structure in the UTLS. According to Jesswein et al., 2025 their data show no clear transition into the stratosphere.

To clarify the vertical placement relative to the tropopause, the correlation between enhanced CH_2Cl_2 VMRs and Potential Temperature Θ is examined in Figure 4.29. The maximum CH_2Cl_2 signal associated with the later time interval is highlighted in red, corresponding to a region with $\Theta > 380$ K. According to the definition by Werner et al., 2010, this places the air mass within the lowermost stratosphere (LMS). While systematic errors and negative VMR values in adjacent regions suggest some caution in interpretation, the enhanced CH_2Cl_2 signal, reaching nearly 200 pptv, supports the conclusion that at least this structure lies within the stratosphere.

The earlier maximum (01 : 15–01 : 30 UTC) is more difficult to classify due to the closeness to the PV = 4 PVU line and more ambiguous separation from the bigger tropospheric CH_2Cl_2 maximum. Nevertheless, both features align with coherent ensembles of HYSPLIT backward trajectories (see Section 4.3), suggesting a shared transport pathway. The spatial separation of these maxima could be indicative of isentropic transport of a single filament, with only one portion having crossed the dynamical tropopause into the stratosphere. Whether the second filament is undergoing or has completed a similar transition remains an open question.

Past studies also support this isentropic transport mechanism. Lauther et al., 2022 observed CH_2Cl_2-enriched air masses associated with the ASM system above the thermal tropopause in the North

Atlantic. These findings confirm that isentropic transport from the AMA can introduce trace gases into the extratropical UTLS, where they subsequently mix with midlatitude air masses (see Vogel et al., 2015).

In this thesis, both observed upper maxima are considered with caution to be located in the lower stratosphere. This is supported by the position relative to the dynamical tropopause and consistent transport history, although the classification of the earlier maximum remains less certain.

While the transport pathway is well-supported, the exact origin of the observed CH_2Cl_2 enhancements cannot be directly confirmed through trajectory analysis alone. Given the atmospheric lifetime of CH_2Cl_2, on the order of several months, contributions from other source regions beyond East and Southeast Asia cannot be excluded. Potential long-range transport via the subtropical or polar jet streams could also play a role. Uplift processes, which are not resolved in the HYSPLIT driving ERA5 meteorological data, are theoretically possible all along the trajectories. Nonetheless, East China is recognized as a major source region (An et al., 2021). Emissions from the monsoon region, as confirmed by ICON-ART surface tracers, likely contribute to the observed enhancements. Thus, it is reasonable to associate the stratospheric CH_2Cl_2 signatures in this study with emissions uplifted within the AMA. To more definitively constrain the origin and age of these air masses, future analysis should include shorter-lived tracers. Species with lifetimes on the order of days to weeks could provide greater temporal resolution for transport analysis.

In summary, the presence of enhanced CH_2Cl_2 and PAN in the extratropical lower stratosphere during Flight 8 on 26–27 August 2023 likely reflects long-range, isentropic transport from the AMA region. While the classification of the upper observed structures as stratospheric is not as clear, the data support the conclusion that monsoon-related uplift and subsequent horizontal transport are key drivers of the elevated trace gas concentrations observed in the UTLS.

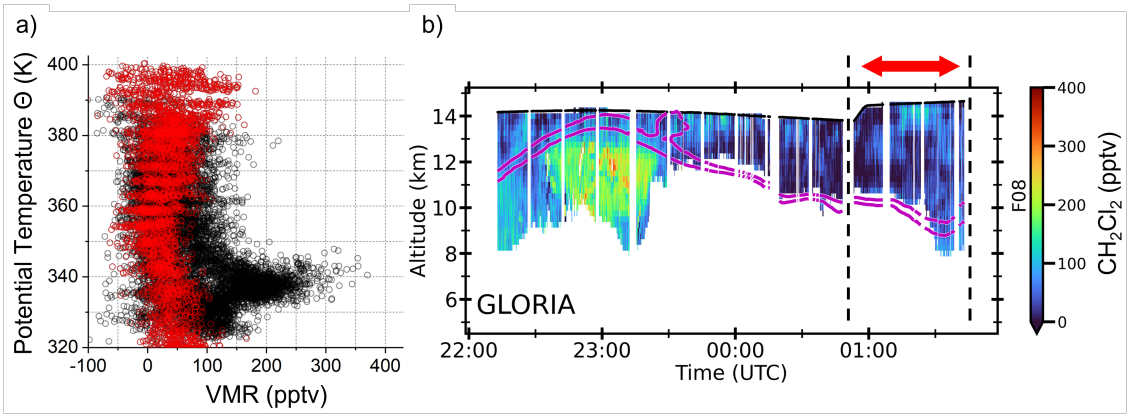

Figure 4.29: VMR of CH_2Cl_2 from Flight 8 against Potential Temperature Θ. Panel a) shows the correlation between the VMR in pptv of CH_2Cl_2 with the Potential Temperature Θ in K from ERA5 reanalysis data. Highlighted in red are the data from the marked section of the cross section in panel b). The VMR against Θ plot was created by Wolfgang Woiwode.

5 Conclusion

This thesis presents observational results from the GLORIA instrument aboard the HALO research aircraft during the PHILEAS campaign in summer 2023, focusing on the transport and distribution of the short-lived ozone-depleting compound CH_2Cl_2 and PAN, both tracer for predominantly anthropogenic pollution. The origin, as well as horizontal and vertical transport of these trace gases were analyzed to better understand long-range pollution transport into the UTLS from the ASM system. For this investigation, observation data from four flights of PHILEAS from end of August to mid September 2023 were used. The key questions of this thesis were addressed by the findings as follows:

What are the characteristics with respect to the UTLS of the observed enhancements of PAN and CH_2Cl_2 above the northeastern Pacific?

The retrieved cross sections reveal enhanced CH_2Cl_2 mixing ratios up to 400 pptv (on 17 September 2023) in the upper troposphere and 180 pptv (on 27 August 2023) in the lower stratosphere over the Gulf of Alaska, with associated relative uncertainties around 30%. For PAN maximum values of 800 pptv (on 17 September 2023) in the troposphere and 250 pptv (on 27 August 2023) in the stratosphere were observed with the same uncertainty of around 30%. The spatial structures of retrieved vertical cross sections from GLORIA reveal relatively strong CH_2Cl_2 enhancements in the upper troposphere. PAN enhancements are partly decoupled from CH_2Cl_2, suggesting the presence of different emission sources or distinct transport mechanisms. PAN filaments lacking corresponding CH_2Cl_2 enhancement and showing broader distributions in the cross sections were not investigated further. The analysis therefore focuses on Flight 8 on 26–27 August 2023 , during which the CH_2Cl_2 maxima in the lower stratosphere were observed. The classification of observed structures as stratospheric is difficult due to the limitations of tropopause height identification and the relative location in the tilted vertical cross sections from GLORIA. Nonetheless, the clear presence of enhanced CH_2Cl_2 in the potential temperature regime of the stratosphere during Flight 8 and the comparison of backward trajectory ensembles suggests transport across the tropopause in the vicinity of the AMA and WPA.

From which specific regions within the ASM does this polluted outflow originate?

The combined temporal and vertical ICON-ART surface tracer evolution indicates structured long-range transport of monsoon air mainly from East China into the UTLS above the North Pacific. Trajectory analyses and comparison with cross sections of ICON-ART surface tracers consistently identify East China and the Northwest Pacific as the main source regions of the tropospheric and stratospheric CH_2Cl_2 maxima observed during the four analyzed flights. These results confirm

previous knowledge on CH_2Cl_2 sources in East Asia and demonstrate that observed enhancements are likely linked to known emission regions.

To what extent do different uplift mechanisms, such as Warm Conveyor Belts (WCBs) and ascend in the AMA with subsequent eddy shedding, contribute to the observed transport?

For the tropospheric maximum from Flight 8 on 26–27 August 2023 , backward trajectories point to an uplift region at the outer eastern edge of the main Asian monsoon anticyclone over the Asian continent. The widely used definition of trajectories ascending more than 600 hPa from the lower to upper troposphere applies to the uplift associated with the tropospheric air masses. Other additional used criteria as an analysis of PV minima and the location of the uplift relative to extratropical cyclones could not be covered in this thesis. Although precipitation patterns and climatological frequencies of WCBs over the Northwest Pacific during summer support WCB influence, the evidence presented in this analysis is therefore still too weak to definitively link the air mass ascent into the upper troposphere observed during Flight 8 to a WCB event.

For the stratospheric maxima uplift under the influence of the ASM, followed by horizontal displacement via eddy shedding is a plausible explanation regarding the long-range transport and origin in the ASM region. Although the typical spiraling ascend in around the core of the AMA could not be seen in the trajectories. The eddy shedding is associated with Rossby wave breaking over the Pacific and WPA development over Japan, which can be seen in the horizontal distribution of ICON-ART surface tracers and the geopotential height. This explanation is further supported by preliminary findings from the PHILEAS campaign.

The location and timing of vertical ascent indicate a dominant uplift mechanism occurring outside the core monsoon convection region, specifically over the Northwest Pacific. The ascent and horizontal distribution of air masses show characteristics of both WCB activity and uplift in the AMA with subsequent eddy shedding processes and the development of a WPA.

Summary and outlook

To the best of current knowledge, this raises an open question: Can uplift processes be initiated outside of deep convective regions by WCBs and then subsequently mixed into eddy shedding structures, which may already contain air masses lifted into the AMA? Further research, particularly using PV diagnostics, is needed to better resolve the involved mechanisms. The role of mixing processes, both between air masses of different origin and across the tropopause, remains to be quantified in more detail. To better constrain the age and vertical transport pathways of these filaments, future work should employ species with shorter chemical lifetimes. These can provide improved temporal resolution and help distinguish between rapid uplift events and slower ascent.

This thesis provides evidence that the observed CH_2Cl_2 maxima over the North Pacific and Alaska are the result of complex uplift and long-range transport processes originating from East Asia and the Northwest Pacific. The analysis highlights the important role of ASM-related transport, especially outside the core monsoon convection. While uplift via deep convection into the AMA and subsequent eddy shedding is supported by evidence in this thesis and by observations in Riese,

2025, the involvement of WCBs remains to be further investigated. The findings can motivate future search for multi-process interactions in the ASM region, particularly with respect to vertical transport into the UTLS. Studies including PV diagnostics and chemical lifetime analysis could clarify the relative roles of WCBs, monsoon-driven convection and eddy shedding in shaping the distribution of pollutants in the UTLS.

Appendix

A.1 Comparison of Cross Sections from GLORIA and ICON-ART Surface Tracer

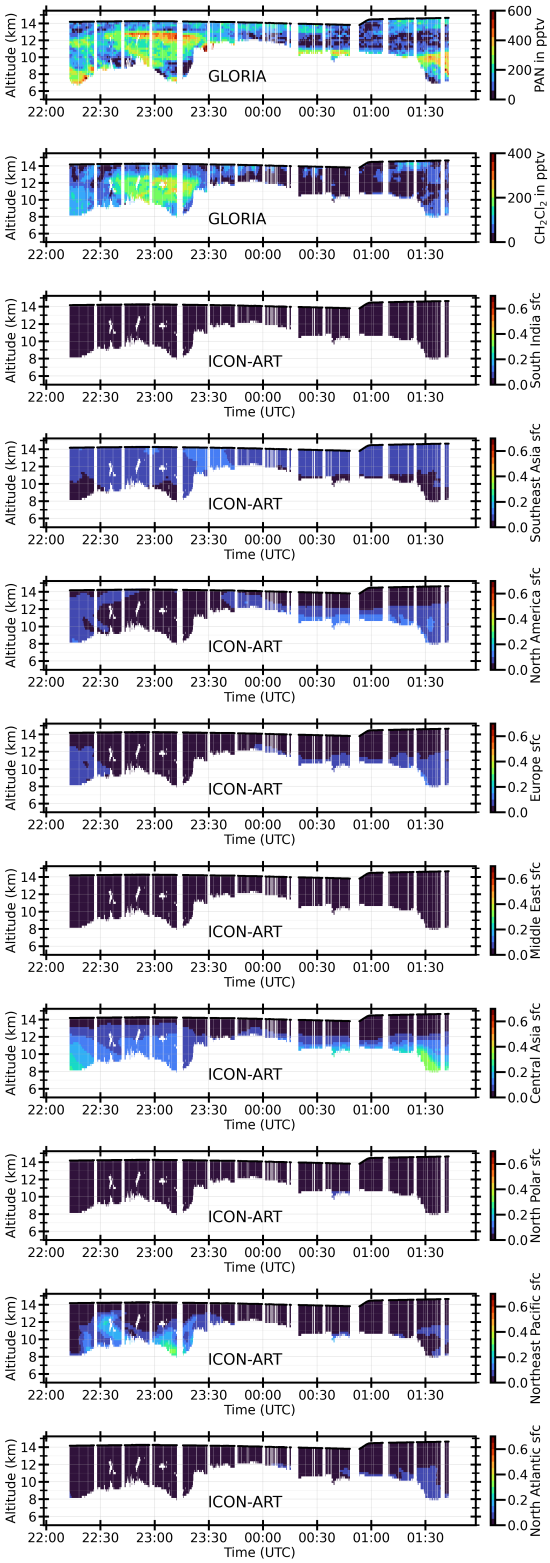

Figure A.1: Cross section from the GLORIA retrieval for PAN and CH_2Cl_2 from Flight 8 on 26–27 August 2023 in comparison to the left out ICON-ART surface tracer from Section 4.9.

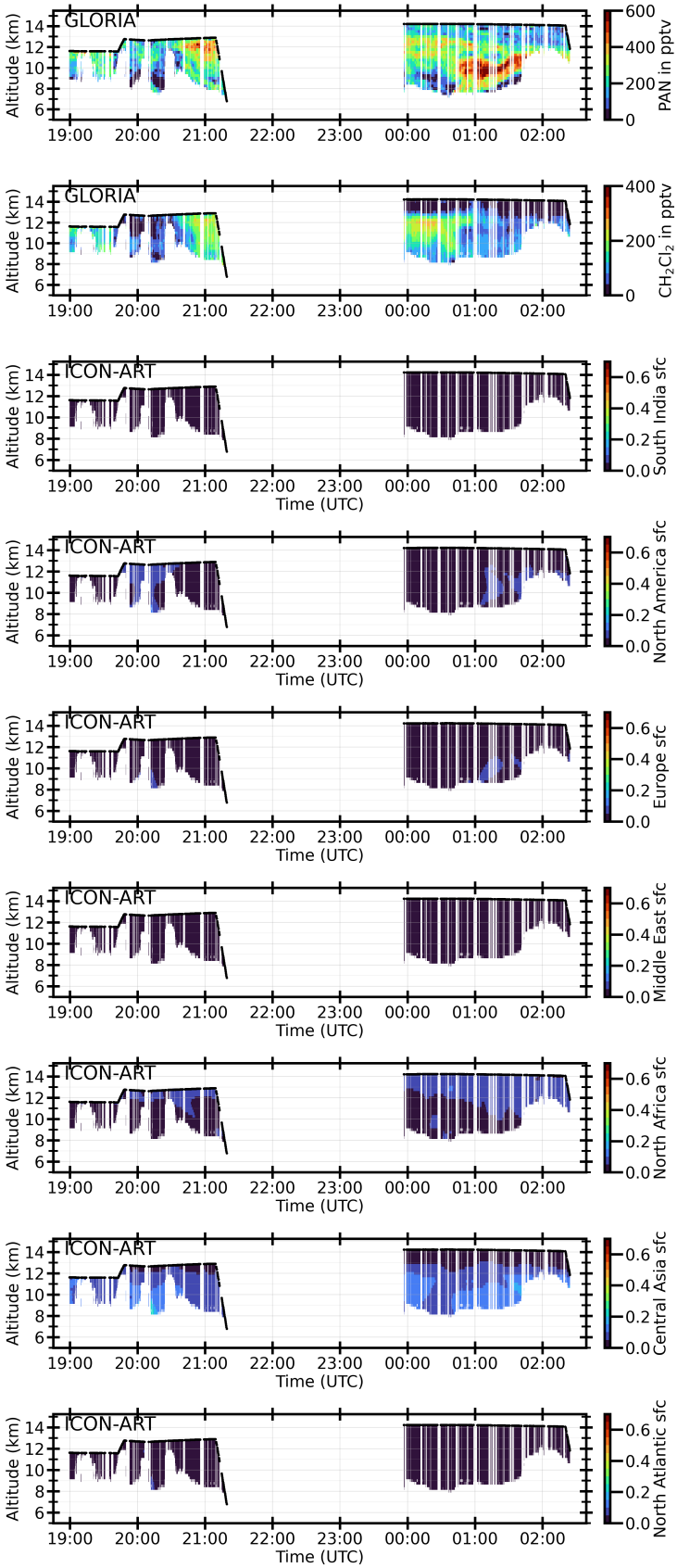

Figure A.2: Cross section from the GLORIA retrieval for PAN and CH_2Cl_2 from Flight 9 on 28–29 August 2023 in comparison to the left out ICON-ART surface tracer from Section 4.10.

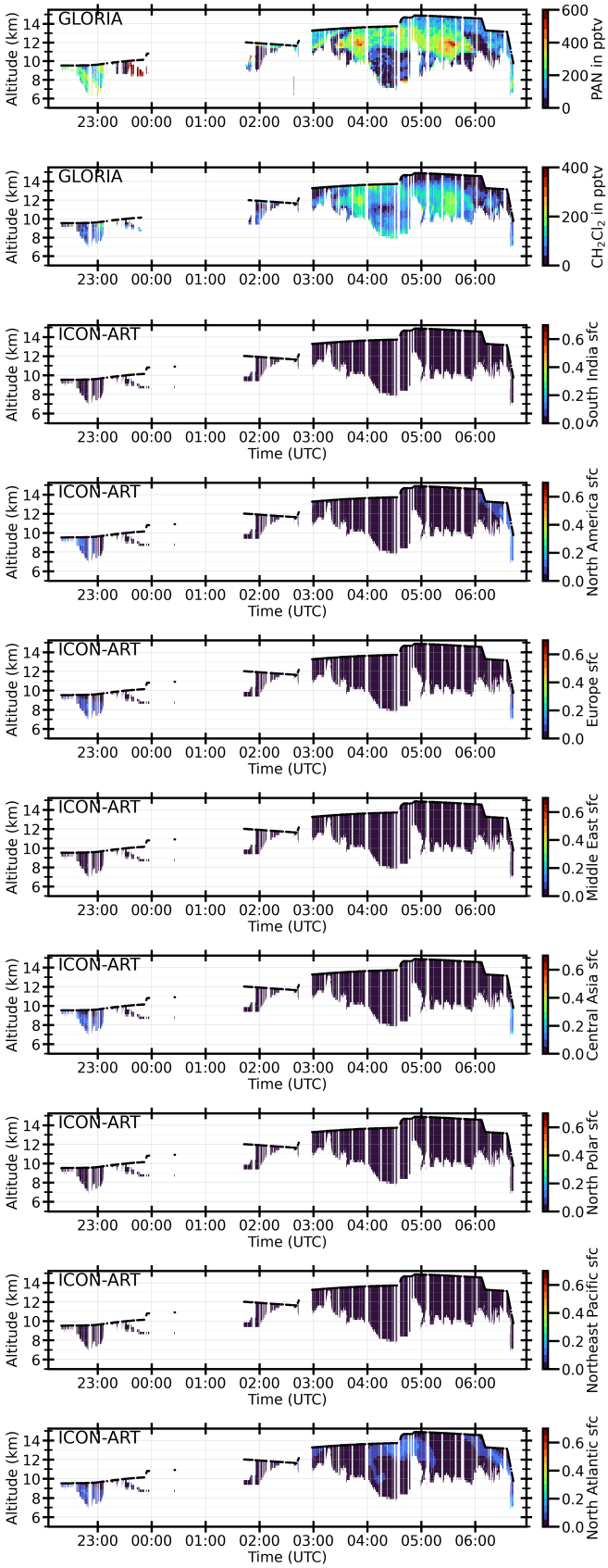

Figure A.3: Cross section from the GLORIA retrieval for PAN and CH_2Cl_2 from Flight 16 on 15–16 September 2023 in comparison to the left out ICON-ART surface tracer from Section 4.11.

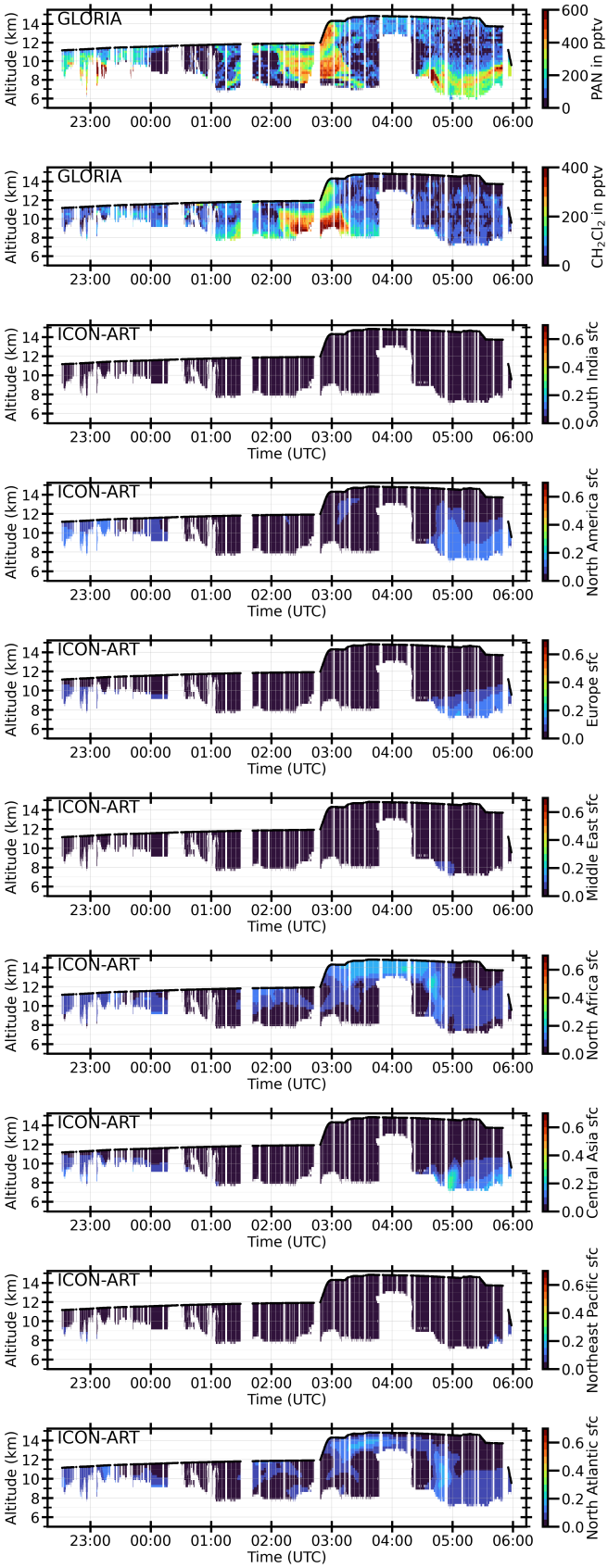

Figure A.4: Cross section from the GLORIA retrieval for PAN and CH_2Cl_2 from Flight 17 on 16–17 September 2023 in comparison to the left out ICON-ART surface tracer from Section 4.12.

A.2 Backward Trajectories for PAN Observations

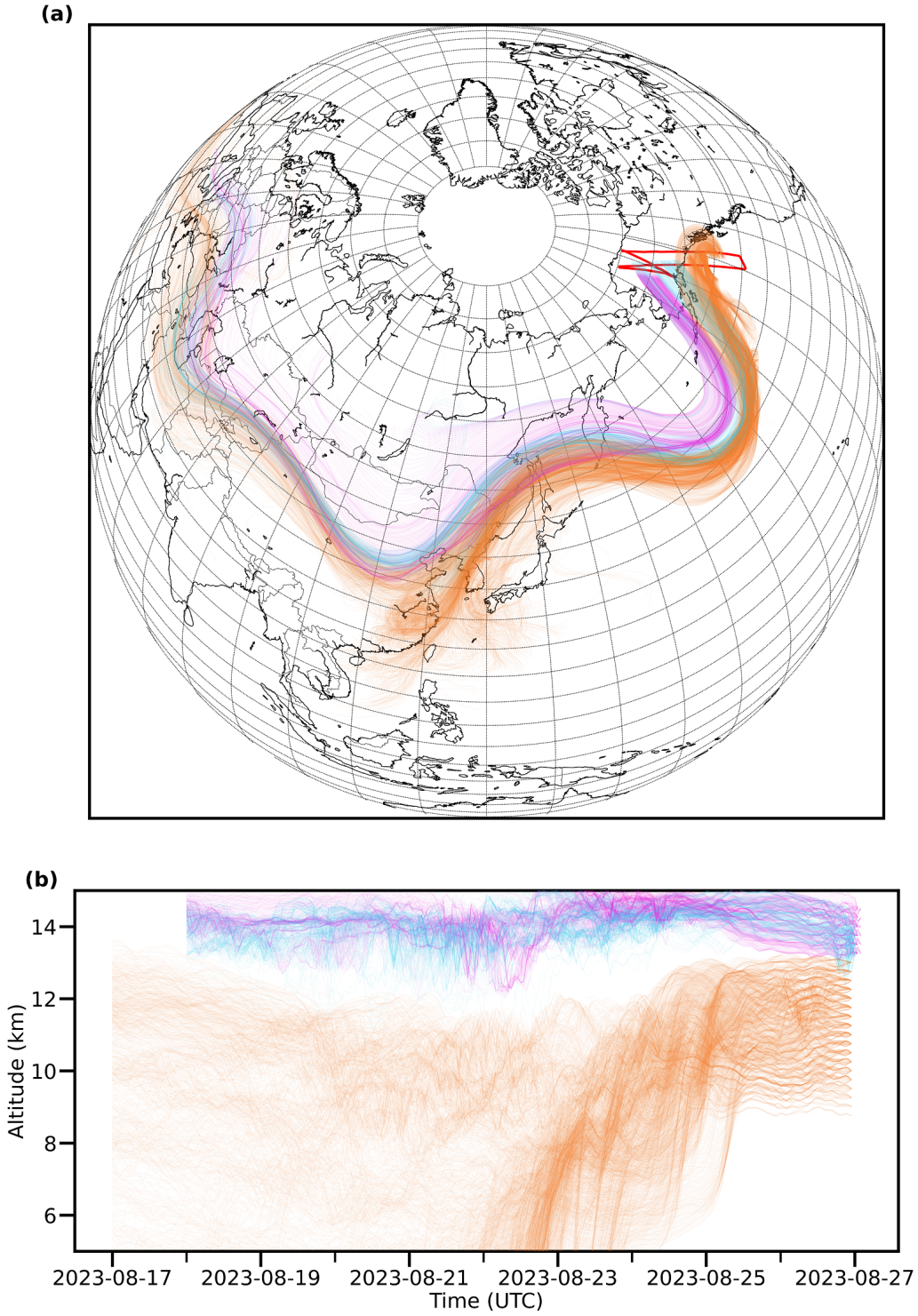

Figure A.5: Ensembles of backward trajectories from HYSPLIT belonging to the defined ROI with respect to the PAN maxima from Flight 8 on 26–27 August 2023 . The same format as in Figure 4.21 was used.

Bibliography

Adcock, K. E., Fraser, P. J., Hall, B. D., Langenfelds, R. L., Lee, G., Montzka, S. A., Oram, D. E., Röckmann, T., Stroh, F., Sturges, W. T., Vogel, B., & Laube, J. C. (2021). Aircraft-based observations of ozone-depleting substances in the upper troposphere and lower stratosphere in and above the asian summer monsoon. *Journal of Geophysical Research: Atmospheres*, *126*(1), e2020JD033137. https://doi.org/10.1029/2020JD033137

An, M., Western, L. M., Say, D., Chen, L., Claxton, T., Ganesan, A. L., Hossaini, R., Krummel, P. B., Manning, A. J., Mühle, J., O'Doherty, S., Prinn, R. G., Weiss, R. F., Young, D., Hu, J., Yao, B., & Rigby, M. (2021). Rapid increase in dichloromethane emissions from china inferred through atmospheric observations. *Nature Communications*, *12*(1), 7279. https://doi.org/10.1038/s41467-021-27592-y

Basha, G., Ratnam, M. V., & Kishore, P. (2020). Asian summer monsoon anticyclone: Trends and variability. *Atmospheric Chemistry and Physics*, *20*(11), 6789–6801. https://doi.org/10.5194/acp-20-6789-2020

Boos, W. R., & Kuang, Z. (2010). Dominant control of the south asian monsoon by orographic insulation versus plateau heating. *Nature*, *463*(7278), 218–222. https://doi.org/10.1038/nature08707

Bourguet, S., & Linz, M. (2022). The impact of improved spatial and temporal resolution of reanalysis data on lagrangian studies of the tropical tropopause layer. *Atmospheric Chemistry and Physics*, *22*(20), 13325–13339. https://doi.org/10.5194/acp-22-13325-2022

Cooper, O. R., Forster, C., Parrish, D., Trainer, M., Dunlea, E., Ryerson, T., Hübler, G., Fehsenfeld, F., Nicks, D., Holloway, J., de Gouw, J., Warneke, C., Roberts, J. M., Flocke, F., & Moody, J. (2004). A case study of transpacific warm conveyor belt transport: Influence of merging airstreams on trace gas import to north america. *Journal of Geophysical Research: Atmospheres*, *109*. https://doi.org/10.1029/2003JD003624

Copernicus Climate Change Service. (2018). ERA5 hourly data on pressure levels from 1940 to present. https://doi.org/10.24381/CDS.BD0915C6

Ding, Y. (2007). The variability of the asian summer monsoon. *Journal of the Meteorological Society of Japan. Ser. II*, *85B*(0), 21–54. https://doi.org/10.2151/jmsj.85B.21

Ding, Y., & Chan, J. C. L. (2005). The east asian summer monsoon: An overview. *Meteorology and Atmospheric Physics*, *89*(1), 117–142. https://doi.org/10.1007/s00703-005-0125-z

Eckhardt, S., Stohl, A., Wernli, H., James, P., Forster, C., & Spichtinger, N. (2004). A 15-year climatology of warm conveyor belts. *Journal of Climate*, *17*(1), 218–237. https://doi.org/10.1175/1520-0442(2004)017<0218:AYCOWC>2.0.CO;2

Fadnavis, S., Schultz, M. G., Semeniuk, K., Mahajan, A. S., Pozzoli, L., Sonbawne, S., Ghude, S. D., Kiefer, M., & Eckert, E. (2014). Trends in peroxyacetyl nitrate (PAN) in the upper

troposphere and lower stratosphere over southern asia during the summer monsoon season: Regional impacts. *Atmospheric Chemistry and Physics*, *14*(23), 12725–12743. https://doi.org/10.5194/acp-14-12725-2014

Fischer, E. V., Jacob, D. J., Yantosca, R. M., Sulprizio, M. P., Millet, D. B., Mao, J., Paulot, F., Singh, H. B., Roiger, A., Ries, L., Talbot, R., Dzepina, K., & Pandey Deolal, S. (2014). Atmospheric peroxyacetyl nitrate (PAN): A global budget and source attribution. *Atmospheric Chemistry and Physics*, *14*(5), 2679–2698. https://doi.org/10.5194/acp-14-2679-2014

Friedl-Vallon, F., Gulde, T., Hase, F., Kleinert, A., Kulessa, T., Maucher, G., Neubert, T., Olschewski, F., Piesch, C., Preusse, P., Rongen, H., Sartorius, C., Schneider, H., Schönfeld, A., Tan, V., Bayer, N., Blank, J., Dapp, R., Ebersoldt, A., … Ungermann, J. (2014). Instrument concept of the imaging fourier transform spectrometer GLORIA. *Atmospheric Measurement Techniques*, *7*(10), 3565–3577. https://doi.org/10.5194/amt-7-3565-2014

Gaffney, J. S., Marley, N. A., & Prestbo, E. W. (1989). Peroxyacyl nitrates (PANs): Their physical and chemical properties. In H. Brauer, J. S. Gaffney, R. Harkov, M. A. K. Khalil, F. W. Lipfert, N. A. Marley, E. W. Prestbo, & G. E. Shaw (Eds.), *Air pollution* (pp. 1–38). Springer. https://doi.org/10.1007/978-3-540-46113-5_1

Garny, H., & Randel, W. J. (2013). Dynamic variability of the asian monsoon anticyclone observed in potential vorticity and correlations with tracer distributions. *Journal of Geophysical Research: Atmospheres*, *118*(24), 13, 421–13, 433. https://doi.org/10.1002/2013JD020908

Gill, A. E. (1980). Some simple solutions for heat-induced tropical circulation. *Quarterly Journal of the Royal Meteorological Society*, *106*(449), 447–462. https://doi.org/10.1002/qj.49710644905

Glatthor, N., von Clarmann, T., Fischer, H., Funke, B., Grabowski, U., Höpfner, M., Kellmann, S., Kiefer, M., Linden, A., Milz, M., Steck, T., & Stiller, G. P. (2007). Global peroxyacetyl nitrate (PAN) retrieval in the upper troposphere from limb emission spectra of the michelson interferometer for passive atmospheric sounding (MIPAS). *Atmospheric Chemistry and Physics*, *7*(11), 2775–2787. https://doi.org/10.5194/acp-7-2775-2007

Gottschaldt, K.-D., Schlager, H., Baumann, R., Cai, D. S., Eyring, V., Graf, P., Grewe, V., Jöckel, P., Jurkat-Witschas, T., Voigt, C., Zahn, A., & Ziereis, H. (2018). Dynamics and composition of the asian summer monsoon anticyclone. *Atmospheric Chemistry and Physics*, *18*(8), 5655–5675. https://doi.org/10.5194/acp-18-5655-2018

Hallquist, M., Munthe, J., Hu, M., Wang, T., Chan, C. K., Gao, J., Boman, J., Guo, S., Hallquist, Å. M., Mellqvist, J., Moldanova, J., Pathak, R. K., Pettersson, J. B., Pleijel, H., Simpson, D., & Thynell, M. (2016). Photochemical smog in china: Scientific challenges and implications for air-quality policies. *National Science Review*, *3*(4), 401–403. https://doi.org/10.1093/nsr/nww080

Heitmann, K., Sprenger, M., Binder, H., Wernli, H., & Joos, H. (2024). Warm conveyor belt characteristics and impacts along the life cycle of extratropical cyclones: Case studies and climatological analysis based on ERA5. *Weather and Climate Dynamics*, *5*(2), 537–557. https://doi.org/10.5194/wcd-5-537-2024

Hersbach, H., Bell, B., Berrisford, P., Hirahara, S., Horányi, A., Muñoz-Sabater, J., Nicolas, J., Peubey, C., Radu, R., Schepers, D., Simmons, A., Soci, C., Abdalla, S., Abellan, X., Balsamo, G., Bechtold, P., Biavati, G., Bidlot, J., Bonavita, M., … Thépaut, J.-N. (2020).

The ERA5 global reanalysis. *Quarterly Journal of the Royal Meteorological Society*, *146*(730), 1999–2049. https://doi.org/10.1002/qj.3803

Hoffmann, L., Günther, G., Li, D., Stein, O., Wu, X., Griessbach, S., Heng, Y., Konopka, P., Müller, R., Vogel, B., & Wright, J. S. (2019). From ERA-interim to ERA5: The considerable impact of ECMWF's next-generation reanalysis on lagrangian transport simulations. *Atmospheric Chemistry and Physics*, *19*(5), 3097–3124. https://doi.org/10.5194/acp-19-3097-2019

Honomichl, S. B., & Pan, L. L. (2020). Transport from the asian summer monsoon anticyclone over the western pacific. *Journal of Geophysical Research: Atmospheres*, *125*(13), e2019JD032094. https://doi.org/10.1029/2019JD032094

Höpfner, M., Blom, M., Echele, C. E., Glatthor, N., Hase, F., & Stiller, G. (2001). Retrieval simulations for MIPAS-STR measurements. In W. L. Smith & U. M. Timofeev (Eds.). International radiation symposium (Ed.), *IRS 2000: Current problems in atmospheric radiation proceedings of the international radiation symposium, st petersberg, russia, 24-29 july 2000*. A. Deepak.

Höpfner, M., Ungermann, J., Borrmann, S., Wagner, R., Spang, R., Riese, M., Stiller, G., Appel, O., Batenburg, A. M., Bucci, S., Cairo, F., Dragoneas, A., Friedl-Vallon, F., Hünig, A., Johansson, S., Krasauskas, L., Legras, B., Leisner, T., Mahnke, C., … Wohltmann, I. (2019). Ammonium nitrate particles formed in upper troposphere from ground ammonia sources during asian monsoons. *Nature Geoscience*, *12*(8), 608–612. https://doi.org/10.1038/s41561-019-0385-8

Hossaini, R., Chipperfield, M. P., Saiz-Lopez, A., Harrison, J. J., von Glasow, R., Sommariva, R., Atlas, E., Navarro, M., Montzka, S. A., Feng, W., Dhomse, S., Harth, C., Mühle, J., Lunder, C., O'Doherty, S., Young, D., Reimann, S., Vollmer, M. K., Krummel, P. B., & Bernath, P. F. (2015). Growth in stratospheric chlorine from short-lived chemicals not controlled by the montreal protocol. *Geophysical Research Letters*, *42*(11), 4573–4580. https://doi.org/10.1002/2015GL063783

Hossaini, R., Atlas, E., Dhomse, S. S., Chipperfield, M. P., Bernath, P. F., Fernando, A. M., Mühle, J., Leeson, A. A., Montzka, S. A., Feng, W., Harrison, J. J., Krummel, P., Vollmer, M. K., Reimann, S., O'Doherty, S., Young, D., Maione, M., Arduini, J., & Lunder, C. R. (2019). Recent trends in stratospheric chlorine from very short-lived substances. *Journal of Geophysical Research: Atmospheres*, *124*(4), 2318–2335. https://doi.org/10.1029/2018JD029400

Hossaini, R., Chipperfield, M. P., Montzka, S. A., Leeson, A. A., Dhomse, S. S., & Pyle, J. A. (2017). The increasing threat to stratospheric ozone from dichloromethane. *Nature Communications*, *8*(1), 15962. https://doi.org/10.1038/ncomms15962

Hsu, C. J., & Plumb, R. A. (2000). Nonaxisymmetric thermally driven circulations and upper-tropospheric monsoon dynamics. *Journal of the Atmospheric Sciences*, *57*(9), 1255–1276. https://doi.org/10.1175/1520-0469(2000)057<1255:NTDCAU>2.0.CO;2

Huntrieser, H., Heland, J., Schlager, H., Forster, C., Stohl, A., Aufmhoff, H., Arnold, F., Scheel, H. E., Campana, M., Gilge, S., Eixmann, R., & Cooper, O. (2005). Intercontinental air pollution transport from north america to europe: Experimental evidence from airborne measurements and surface observations. *Journal of Geophysical Research: Atmospheres*, *110*. https://doi.org/10.1029/2004JD005045

Jesswein, M., Lauther, V., Emig, N., Hoor, P., Keber, T., Lachnitt, H.-C., Ort, L., Schuck, T., Strobel, J., Van Luijt, R., Volk, C. M., Weyland, F., & Engel, A. (2025). Tracing elevated abundance of CH_2cl_2 in the subarctic upper troposphere to the asian summer monsoon. *EGUsphere*, 1–31. https://doi.org/10.5194/egusphere-2024-3946

Johansson, S., Höpfner, M., Friedl-Vallon, F., Glatthor, N., Gulde, T., Huijnen, V., Kleinert, A., Kretschmer, E., Maucher, G., Neubert, T., Nordmeyer, H., Piesch, C., Preusse, P., Riese, M., Sinnhuber, B.-M., Ungermann, J., Wetzel, G., & Woiwode, W. (2024). Ammonia in the upper troposphere–lower stratosphere (UTLS): GLORIA airborne measurements for CAMS model evaluation in the asian monsoon and in biomass burning plumes above the south atlantic. *Atmospheric Chemistry and Physics*, *24*(14), 8125–8138. https://doi.org/10.5194/acp-24-8125-2024

Johansson, S., Höpfner, M., Kirner, O., Wohltmann, I., Bucci, S., Legras, B., Friedl-Vallon, F., Glatthor, N., Kretschmer, E., Ungermann, J., & Wetzel, G. (2020). Pollution trace gas distributions and their transport in the asian monsoon upper troposphere and lowermost stratosphere during the StratoClim campaign 2017. *Atmospheric Chemistry and Physics*, *20*(23), 14695–14715. https://doi.org/10.5194/acp-20-14695-2020

Johansson, S., Wetzel, G., Friedl-Vallon, F., Glatthor, N., Höpfner, M., Kleinert, A., Neubert, T., Sinnhuber, B.-M., & Ungermann, J. (2022). Biomass burning pollution in the south atlantic upper troposphere: GLORIA trace gas observations and evaluation of the CAMS model. *Atmospheric Chemistry and Physics*, *22*(5), 3675–3691. https://doi.org/10.5194/acp-22-3675-2022

Johansson, S., Woiwode, W., Höpfner, M., Friedl-Vallon, F., Kleinert, A., Kretschmer, E., Latzko, T., Orphal, J., Preusse, P., Ungermann, J., Santee, M. L., Jurkat-Witschas, T., Marsing, A., Voigt, C., Giez, A., Krämer, M., Rolf, C., Zahn, A., Engel, A., … Oelhaf, H. (2018). Airborne limb-imaging measurements of temperature, HNO_3, O_3, $ClONO_2$, H_2O and CFC-12 during the arctic winter 2015/2016: Characterization, in situ validation and comparison to aura/MLS. *Atmospheric Measurement Techniques*, *11*(8), 4737–4756. https://doi.org/10.5194/amt-11-4737-2018

Joos, H., Sprenger, M., Binder, H., Beyerle, U., & Wernli, H. (2023). Warm conveyor belts in present-day and future climate simulations – part 1: Climatology and impacts. *Weather and Climate Dynamics*, *4*(1), 133–155. https://doi.org/10.5194/wcd-4-133-2023

Joppe, P., Schneider, J., Wilsch, J., Bozem, H., Breuninger, A., Curtius, J., Ebert, M., Emig, N., Hoor, P., Ismayil, S., Kandler, K., Kunkel, D., Kurth, I., Lachnitt, H.-C., Li, Y., Miltenberger, A., Richter, S., Rolf, C., Schneider, L., … Borrmann, S. (2025). Transport of biomass burning aerosol into the extratropical tropopause region over europe via warm conveyor belt uplift. *EGUsphere*, 1–39. https://doi.org/10.5194/egusphere-2025-1346

Kleinert, A., Friedl-Vallon, F., Guggenmoser, T., Höpfner, M., Neubert, T., Ribalda, R., Sha, M. K., Ungermann, J., Blank, J., Ebersoldt, A., Kretschmer, E., Latzko, T., Oelhaf, H., Olschewski, F., & Preusse, P. (2014). Level 0 to 1 processing of the imaging fourier transform spectrometer GLORIA: Generation of radiometrically and spectrally calibrated spectra. *Atmospheric Measurement Techniques*, *7*(12), 4167–4184. https://doi.org/10.5194/amt-7-4167-2014

Lauther, V., Vogel, B., Wintel, J., Rau, A., Hoor, P., Bense, V., Müller, R., & Volk, C. M. (2022). In situ observations of CH_2Cl_2 and $CHCl_3$ show efficient transport pathways for very short-lived species into the lower stratosphere via the asian and the north american summer monsoon. *Atmospheric Chemistry and Physics*, *22*(3), 2049–2077. https://doi.org/10.5194/acp-22-2049-2022

Li, T., Wang, Y., Wang, B., Ting, M., Ding, Y., Sun, Y., He, C., & Yang, G. (2022). Distinctive south and east asian monsoon circulation responses to global warming. *Science Bulletin*, *67*(7), 762–770. https://doi.org/10.1016/j.scib.2021.12.001

Madonna, E., Wernli, H., Joos, H., & Martius, O. (2014). Warm conveyor belts in the ERA-interim dataset (1979–2010). part I: Climatology and potential vorticity evolution. *Journal of Climate*, *27*(1), 3–26. https://doi.org/10.1175/JCLI-D-12-00720.1

Mahieu, E., Fischer, E. V., Franco, B., Palm, M., Wizenberg, T., Smale, D., Clarisse, L., Clerbaux, C., Coheur, P.-F., Hannigan, J. W., Lutsch, E., Notholt, J., Cantos, I. P., Prignon, M., Servais, C., & Strong, K. (2021). First retrievals of peroxyacetyl nitrate (PAN) from ground-based FTIR solar spectra recorded at remote sites, comparison with model and satellite data. *Elementa: Science of the Anthropocene*, *9*(1), 00027. https://doi.org/10.1525/elementa.2021.00027

Miyazaki, Y., Kondo, Y., Koike, M., Fuelberg, H. E., Kiley, C. M., Kita, K., Takegawa, N., Sachse, G. W., Flocke, F., Weinheimer, A. J., Singh, H. B., Eisele, F. L., Zondlo, M., Talbot, R. W., Sandholm, S. T., Avery, M. A., & Blake, D. R. (2003). Synoptic-scale transport of reactive nitrogen over the western pacific in spring. *Journal of Geophysical Research: Atmospheres*, *108*. https://doi.org/10.1029/2002JD003248

Norton, R. H., & Beer, R. (1977). Errata: New apodizing functions for fourier spectrometry. *Journal of the Optical Society of America*, *67*(3), 419. https://doi.org/10.1364/JOSA.67.000419

Norton, R. H., & Beer, R. (1976). New apodizing functions for fourier spectrometry. *JOSA*, *66*(3), 259–264. https://doi.org/10.1364/JOSA.66.000259

Pan, L. L., Atlas, E. L., Honomichl, S. B., Smith, W. P., Kinnison, D. E., Solomon, S., Santee, M. L., Saiz-Lopez, A., Laube, J. C., Wang, B., Ueyama, R., Bresch, J. F., Hornbrook, R. S., Apel, E. C., Hills, A. J., Treadaway, V., Smith, K., Schauffler, S., Donnelly, S., … Newman, P. A. (2024). East asian summer monsoon delivers large abundances of very short-lived organic chlorine substances to the lower stratosphere. *Proceedings of the National Academy of Sciences*, *121*(12), e2318716121. https://doi.org/10.1073/pnas.2318716121

Pan, L. L., Honomichl, S. B., Kinnison, D. E., Abalos, M., Randel, W. J., Bergman, J. W., & Bian, J. (2016). Transport of chemical tracers from the boundary layer to stratosphere associated with the dynamics of the asian summer monsoon. *Journal of Geophysical Research: Atmospheres*, *121*(23), 14, 159–14, 174. https://doi.org/10.1002/2016JD025616

Park, S., Atlas, E. L., Jiménez, R., Daube, B. C., Gottlieb, E. W., Nan, J., Jones, D. B. A., Pfister, L., Conway, T. J., Bui, T. P., Gao, R.-S., & Wofsy, S. C. (2010). Vertical transport rates and concentrations of OH and Cl radicals in the tropical tropopause layer from observations of CO_2 and halocarbons: Implications for distributions of long- and short-lived chemical species. *Atmospheric Chemistry and Physics*, *10*(14), 6669–6684. https://doi.org/10.5194/acp-10-6669-2010

Piesch, C., Sartorius, C., Friedl-Vallon, F., Gulde, T., Heger, S., Kretschmer, E., Maucher, G., Nordmeyer, H., Barthel, J., Ebersoldt, A., Graf, F., Hase, F., Kleinert, A., Neubert, T., &

Schillings, H. J. (2015). The mechanical and thermal setup of the GLORIA spectrometer. *Atmospheric Measurement Techniques*, *8*(4), 1773–1787. https://doi.org/10.5194/amt-8-1773-2015

Ploeger, F., Diallo, M., Charlesworth, E., Konopka, P., Legras, B., Laube, J. C., Grooß, J.-U., Günther, G., Engel, A., & Riese, M. (2021). The stratospheric brewer–dobson circulation inferred from age of air in the ERA5 reanalysis. *Atmospheric Chemistry and Physics*, *21*(11), 8393–8412. https://doi.org/10.5194/acp-21-8393-2021

Ploeger, F., Konopka, P., Walker, K., & Riese, M. (2017). Quantifying pollution transport from the asian monsoon anticyclone into the lower stratosphere. *Atmospheric Chemistry and Physics*, *17*(11), 7055–7066. https://doi.org/10.5194/acp-17-7055-2017

Plumb, R. A. (1996). A "tropical pipe" model of stratospheric transport. *Journal of Geophysical Research: Atmospheres*, *101*, 3957–3972. https://doi.org/10.1029/95JD03002

Popovic, J. M., & Plumb, R. A. (2001). Eddy shedding from the upper-tropospheric asian monsoon anticyclone. *Journal of the Atmospheric Sciences*, *58*(1), 93–104. https://doi.org/10.1175/1520-0469(2001)058<0093:ESFTUT>2.0.CO;2

Potisomporn, P., Adcock, T. A. A., & Vogel, C. R. (2023). Evaluating ERA5 reanalysis predictions of low wind speed events around the UK. *Energy Reports*, *10*, 4781–4790. https://doi.org/10.1016/j.egyr.2023.11.035

Randel, W. J., & Park, M. (2006). Deep convective influence on the asian summer monsoon anticyclone and associated tracer variability observed with atmospheric infrared sounder (AIRS). *Journal of Geophysical Research: Atmospheres*, *111*. https://doi.org/10.1029/2005JD006490

Rieger, D., Bangert, M., Bischoff-Gauss, I., Förstner, J., Lundgren, K., Reinert, D., Schröter, J., Vogel, H., Zängl, G., Ruhnke, R., & Vogel, B. (2015). ICON–ART 1.0 – a new online-coupled model system from the global to regional scale. *Geoscientific Model Development*, *8*(6), 1659–1676. https://doi.org/10.5194/gmd-8-1659-2015

Riese, M., Oelhaf, H., Preusse, P., Blank, J., Ern, M., Friedl-Vallon, F., Fischer, H., Guggenmoser, T., Höpfner, M., Hoor, P., Kaufmann, M., Orphal, J., Plöger, F., Spang, R., Suminska-Ebersoldt, O., Ungermann, J., Vogel, B., & Woiwode, W. (2014). Gimballed limb observer for radiance imaging of the atmosphere (GLORIA) scientific objectives. *Atmospheric Measurement Techniques*, *7*(7), 1915–1928. https://doi.org/10.5194/amt-7-1915-2014

Riese, M. (2025). Long-range transport of polluted asian summer monsoon air to high latitudes during the PHILEAS campaign in the boreal summer 2023.

Schröter, J., Rieger, D., Stassen, C., Vogel, H., Weimer, M., Werchner, S., Förstner, J., Prill, F., Reinert, D., Zängl, G., Giorgetta, M., Ruhnke, R., Vogel, B., & Braesicke, P. (2018). ICON-ART 2.1: A flexible tracer framework and its application for composition studies in numerical weather forecasting and climate simulations. *Geoscientific Model Development*, *11*(10), 4043–4068. https://doi.org/10.5194/gmd-11-4043-2018

Sharpe, S. W., Johnson, T. J., Sams, R. L., Chu, P. M., Rhoderick, G. C., & Johnson, P. A. (2004). Gas-phase databases for quantitative infrared spectroscopy. *Applied Spectroscopy*, *58*(12), 1452–1461. https://doi.org/10.1366/0003702042641281

Singh, H. B. (1987). Reactive nitrogen in the troposphere. *Environmental Science & Technology*, *21*(4), 320–327. https://doi.org/10.1021/es00158a001

Siu, L. W., & Bowman, K. P. (2019). Forcing of the upper-tropospheric monsoon anticyclones. *Journal of the Atmospheric Sciences*, *76*(7), 1937–1954. https://doi.org/10.1175/JAS-D-18-0340.1

Siu, L. W., & Bowman, K. P. (2020). Unsteady vortex behavior in the asian monsoon anticyclone. *Journal of the Atmospheric Sciences*, *77*(12), 4067–4088. https://doi.org/10.1175/JAS-D-19-0349.1

Smith, K., Atlas, E., Apel, E. C., Blake, D. R., Dutton, G., Hornbrook, R. S., Montzka, S., Mühle, J., Schauffler, S., & Treadaway, V. (2024). Chloromethanes in the north american troposphere and lower stratosphere over the past two decades. *Geophysical Research Letters*, *51*(15), e2024GL108710. https://doi.org/10.1029/2024GL108710

Stein, A. F., Draxler, R. R., Rolph, G. D., Stunder, B. J. B., Cohen, M. D., & Ngan, F. (2015). NOAA's HYSPLIT atmospheric transport and dispersion modeling system. *Bulletin of the American Meteorological Society*, *96*(12), 2059–2077. https://doi.org/10.1175/BAMS-D-14-00110.1

Stiller, G. P. (2000). *The Karlsruhe optimized and precise radiative transfer algorithm*. https://doi.org/10.5445/IR/270048971

Stiller, G. P., von Clarmann, T., Funke, B., Glatthor, N., Hase, F., Höpfner, M., & Linden, A. (2002). Sensitivity of trace gas abundances retrievals from infrared limb emission spectra to simplifying approximations in radiative transfer modelling. *Journal of Quantitative Spectroscopy and Radiative Transfer*, *72*(3), 249–280. https://doi.org/10.1016/S0022-4073(01)00123-6

Turhal, K., Plöger, F., Clemens, J., Birner, T., Weyland, F., Konopka, P., & Hoor, P. (2024). Variability and trends in the potential vorticity (PV)-gradient dynamical tropopause. *Atmospheric Chemistry and Physics*, *24*(23), 13653–13679. https://doi.org/10.5194/acp-24-13653-2024

Ungermann, J., Ern, M., Kaufmann, M., Müller, R., Spang, R., Ploeger, F., Vogel, B., & Riese, M. (2016). Observations of PAN and its confinement in the asian summer monsoon anticyclone in high spatial resolution. *Atmospheric Chemistry and Physics*, *16*(13), 8389–8403. https://doi.org/10.5194/acp-16-8389-2016

Ungermann, J., Kleinert, A., Maucher, G., Bartolomé, I., Friedl-Vallon, F., Johansson, S., Krasauskas, L., & Neubert, T. (2022). Quantification and mitigation of the instrument effects and uncertainties of the airborne limb imaging FTIR GLORIA. *Atmospheric Measurement Techniques*, *15*(8), 2503–2530. https://doi.org/10.5194/amt-15-2503-2022

Vernier, J.-P., Thomason, L. W., & Kar, J. (2011). CALIPSO detection of an asian tropopause aerosol layer. *Geophysical Research Letters*, *38*(7). https://doi.org/10.1029/2010GL046614

Villamayor, J., Iglesias-Suarez, F., Cuevas, C. A., Fernandez, R. P., Li, Q., Abalos, M., Hossaini, R., Chipperfield, M. P., Kinnison, D. E., Tilmes, S., Lamarque, J.-F., & Saiz-Lopez, A. (2023). Very short-lived halogens amplify ozone depletion trends in the tropical lower stratosphere. *Nature Climate Change*, *13*(6), 554–560. https://doi.org/10.1038/s41558-023-01671-y

Vogel, B., Günther, G., Müller, R., Grooß, J.-U., Hoor, P., Krämer, M., Müller, S., Zahn, A., & Riese, M. (2014). Fast transport from southeast asia boundary layer sources to northern europe: Rapid uplift in typhoons and eastward eddy shedding of the asian monsoon anticyclone. *Atmospheric Chemistry and Physics*, *14*(23), 12745–12762. https://doi.org/10.5194/acp-14-12745-2014

Vogel, B., Günther, G., Müller, R., Grooß, J.-U., & Riese, M. (2015). Impact of different asian source regions on the composition of the asian monsoon anticyclone and of the extratropical lowermost stratosphere. *Atmospheric Chemistry and Physics*, *15*(23), 13699–13716. https://doi.org/10.5194/acp-15-13699-2015

Vogel, B., Günther, G., Müller, R., Grooß, J.-U., Afchine, A., Bozem, H., Hoor, P., Krämer, M., Müller, S., Riese, M., Rolf, C., Spelten, N., Stiller, G. P., Ungermann, J., & Zahn, A. (2016). Long-range transport pathways of tropospheric source gases originating in asia into the northern lower stratosphere during the asian monsoon season 2012. *Atmospheric Chemistry and Physics*, *16*(23), 15301–15325. https://doi.org/10.5194/acp-16-15301-2016

Vogel, B., Müller, R., Günther, G., Spang, R., Hanumanthu, S., Li, D., Riese, M., & Stiller, G. P. (2019). Lagrangian simulations of the transport of young air masses to the top of the asian monsoon anticyclone and into the tropical pipe. *Atmospheric Chemistry and Physics*, *19*(9), 6007–6034. https://doi.org/10.5194/acp-19-6007-2019

Vogel, B., Volk, C. M., Wintel, J., Lauther, V., Clemens, J., Grooß, J.-U., Günther, G., Hoffmann, L., Laube, J. C., Müller, R., Ploeger, F., & Stroh, F. (2024). Evaluation of vertical transport in ERA5 and ERA-interim reanalysis using high-altitude aircraft measurements in the asian summer monsoon 2017. *Atmospheric Chemistry and Physics*, *24*(1), 317–343. https://doi.org/10.5194/acp-24-317-2024

von Hobe, M., Ploeger, F., Konopka, P., Kloss, C., Ulanowski, A., Yushkov, V., Ravegnani, F., Volk, C. M., Pan, L. L., Honomichl, S. B., Tilmes, S., Kinnison, D. E., Garcia, R. R., & Wright, J. S. (2021). Upward transport into and within the asian monsoon anticyclone as inferred from StratoClim trace gas observations. *Atmospheric Chemistry and Physics*, *21*(2), 1267–1285. https://doi.org/10.5194/acp-21-1267-2021

Wang, B., & LinHo. (2002). Rainy season of the asian–pacific summer monsoon. *Journal of Climate*, *15*(4), 386–398. https://doi.org/10.1175/1520-0442(2002)015<0386:RSOTAP>2.0.CO;2

Wang, X., Randel, W., Pan, L., Wu, Y., & Zhang, P. (2022). Transient behavior of the asian summer monsoon anticyclone associated with eastward eddy shedding. *Journal of Geophysical Research: Atmospheres*, *127*(6), e2021JD036090. https://doi.org/10.1029/2021JD036090

Werner, A., Volk, C. M., Ivanova, E. V., Wetter, T., Schiller, C., Schlager, H., & Konopka, P. (2010). Quantifying transport into the arctic lowermost stratosphere. *Atmospheric Chemistry and Physics*, *10*(23), 11623–11639. https://doi.org/10.5194/acp-10-11623-2010

Wetzel, G., Friedl-Vallon, F., Glatthor, N., Grooß, J.-U., Gulde, T., Höpfner, M., Johansson, S., Khosrawi, F., Kirner, O., Kleinert, A., Kretschmer, E., Maucher, G., Nordmeyer, H., Oelhaf, H., Orphal, J., Piesch, C., Sinnhuber, B.-M., Ungermann, J., & Vogel, B. (2021). Pollution trace gases C_2H_6, C_2H_2, HCOOH, and PAN in the north atlantic UTLS: Observations and simulations. *Atmospheric Chemistry and Physics*, *21*(10), 8213–8232. https://doi.org/10.5194/acp-21-8213-2021

Woiwode, W., Sumińska-Ebersoldt, O., Oelhaf, H., Höpfner, M., Belyaev, G. V., Ebersoldt, A., Friedl-Vallon, F., Grooß, J.-U., Gulde, T., Kaufmann, M., Kleinert, A., Krämer, M., Kretschmer, E., Kulessa, T., Maucher, G., Neubert, T., Piesch, C., Preusse, P., Riese, M., … Orphal, J. (2015). Validation of first chemistry mode retrieval results from the new limb-imaging FTS GLORIA with correlative MIPAS-STR observations. *Atmospheric Measurement Techniques*, *8*(6), 2509–2520. https://doi.org/10.5194/amt-8-2509-2015

Woiwode, W., Grooß, J.-U., Lauther, V., Johansson, S., Ungermann, J., Neubert, T., Engel, A., Hoor, P., & Riese, M. (2025). *Two-dimensional observations of dichloromethane-rich air masses transported from the asian summer monsoon region across the north pacific* (EGU25-12886). Copernicus Meetings. https://doi.org/10.5194/egusphere-egu25-12886

Zhai, S., Jacob, D. J., Franco, B., Clarisse, L., Coheur, P., Shah, V., Bates, K. H., Lin, H., Dang, R., Sulprizio, M. P., Huey, L. G., Moore, F. L., Jaffe, D. A., & Liao, H. (2024). Transpacific transport of asian peroxyacetyl nitrate (PAN) observed from satellite: Implications for ozone. *Environmental Science & Technology*, *58*(22), 9760–9769. https://doi.org/10.1021/acs.est.4c01980

Acknowledgments

First and foremost, I want to sincerely thank Michael Höpfner for supervising this thesis and serving as a reviewer. Your thoughtful feedback, aid, and trust in my work have made a huge difference throughout the entire process.

I would like to thank Björn-Martin Sinnhuber for kindly agreeing to serve as a second reviewer and taking the time to make this thesis possible.

I'm deeply thankful to Sören Johansson for supervising this work, for your encouragement, your guidance and for always being there with advice, be it for the analyses or programming problems, when I needed it. A big thank you for accompanying me throughout the entire thesis.

I'm especially grateful to Wolfgang Woiwode for providing the first CH_2Cl_2 retrievals and for our many insightful discussions about trace gases in the lower stratosphere. Your detailed feedback on the thesis really helped shape the discussion with a broader perspective.

Thank you to Gerald Wetzel for your valuable feedback on the thesis and for pointing me toward looking into WCB-related uplift, which turned out to be a key piece of the thesis.

To Anne Kleinert for her valuable feedback on the technical details of GLORIA and the whole FFB group thank you for the technical support, the discussions and input during our meetings, and for helping me find my way around the world of airborne remote sensing.

A special thanks to Annika Oertel for her support and helpful conversation about warm conveyor belts, and for providing access to extra ERA5 data that turned out to be very useful.

Finally, a big thanks to the entire GLORIA team from KIT and FZJ — not only for the data from the PHILEAS campaign, but also for the amazing time we had together during the ASCCI campaign in March 2025. I am truly thankful for the warm and heartfelt way in which you welcomed me as a member of your team.

Disclosure of additional tools

The following additional tools were used for this thesis:

- All self-generated plots were created using Python code, version 3.10.
- This thesis was written in LaTeX using the Overleaf editor.
- The chatbot ChatGPT with the GPT-4o engine, the large language model developed by OpenAI, was used as a tool for programming in Python and writing LaTeX code.
- For assistance with English phrasing ChatGPT with the GPT-4o engine by OpenAI was used.
- For the literature review, the AI research assistants SciSpace, Consensus, and Elicit were used.
- The software Zotero was used for literature management and for generating the bibliography

Erklärung

Ich versichere wahrheitsgemäß, die Arbeit selbstständig verfasst, alle benutzten Hilfsmittel vollständig und genau angegeben und alles kenntlich gemacht zu haben, was aus Arbeiten anderer unverändert oder mit Abänderungen entnommen wurde sowie die Satzung des KIT zur Sicherung guter wissenschaftlicher Praxis in der jeweils gültigen Fassung beachtet zu haben.

I herewith declare that the present thesis is original work written by me alone and that I have indicated completely and precisely all aids used as well as all citations, whether changed or unchanged, of other theses and publications, and that I have observed the Rules of KIT for Safeguarding Good Scientific Practice, as amended.

Karlsruhe, 08.05.2025

Franziska Trinkl

Accepted as an examination copy.

Michael Höpfner